Institut für Biophysik
Fachrichtung für Physik
Fakultät für Mathematik und Naturwissenschaften
Technische Universität Dresden

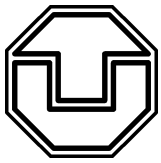

Fluorescence imaging microscopy studies on single molecule diffusion and photophysical dynamics

Dissertation
zur Erlangung des Akademischen Grades
Doktor rerum naturalium
(Dr. rer. nat.)

vorgelegt von

Stephan Schäfer

geboren in Limburg/Lahn am 9. August 1973

September 2006

1. Gutachter: Prof. Dr. Petra Schwille

2. Gutachter: Prof. Dr. Lukas Eng

3. Gutachter: Prof. Dr. Ulrich Kubitscheck

Das Rigorosum und die Disputation fanden am 9. März 2007 statt.

Meinen Eltern und meiner Großmutter.

Abstract

Within the last years, e.g. by investigating the fluorescence of single molecules in biological cells, remarkable progress has been made in cell biology extending conventional ensemble techniques concerning temporal / spatial resolution and the detection of particle subpopulations [82]. In addition to employing single fluorophores as "molecular beacons" to determine the position of biomolecules, single molecule fluorescence studies allow to access the photophysical dynamics of genetically encoded fluorescent proteins itself.

However, in order to gain statistically consistent results, e.g. on the mobility behavior or the photophysical properties, the fluorescence image sequences have to be analyzed in a preferentially automated and calibrated (non-biased) way.

In this thesis, a single molecule fluorescence optical setup was developed and calibrated and experimental biological *in-vitro* systems were adapted to the needs of single molecule imaging.

Based on the fluorescence image sequences obtained, an automated analysis algorithm was developed, characterized and its limits for reliable quantitative data analysis were determined.

For lipid marker molecules diffusing in an artificial lipid membrane, the optimum way of the single molecule trajectory analysis of the image sequences was explored. Furthermore, effects of all relevant artifacts (specifically low signal-to-noise ratio, finite acquisition time and high spot density, in combination with photobleaching) on the recovered diffusion coefficients were carefully studied.

The performance of the method was demonstrated in two series of experiments. In one series, the diffusion of a fluorescent lipid probe in artificial lipid bilayer membranes of giant unilamellar vesicles was investigated. In another series of experiments, the photoconversion and photobleaching behavior of the fluorescent protein *Kaede*-GFP was characterized and protein subpopulations were identified.

List of publications

The results presented in this thesis are partly already published in the following articles or in preparation:

1. S. Berezhna, S. P. Schäfer, G. Böse, M. Jahnz, A. Deniz, and P. Schwille. New effects in polynucleotide release from cationic lipid carriers revealed by confocal imaging, fluorescence cross-correlation spectroscopy and single particle tracking. *Biochim. Biophys. Acta.*, 1669:193-207, 2005.

2. P. S. Dittrich, S. P. Schäfer, and P. Schwille. Characterization of the photoconversion reaction of the fluorescent protein Kaede on single molecule level. *Biophys. J*, 89:3446-3455, 2005.

3. S. P. Schäfer, P. S. Dittrich, E. P. Petrov, and P. Schwille. Single molecule fluorescence imaging of the photoinduced conversion and bleaching behavior of the fluorescent protein Kaede. *Mic. Res. Technique*, 69:210-219, 2006.

4. S. P. Schäfer, E. P. Petrov, and P. Schwille. Comparison of diffusion coefficients in lipid bilayer membranes by single molecule tracking. *in preparation.*

Contents

1. Introduction

1.1. From single particle to single molecule tracking on lipid membranes

Within the last years, the single particle/molecule tracking[1] (SPT/SMT) technique has made tremendous progress in cell biology by its potential to extend conventional ensemble techniques concerning temporal / spatial resolution and the detection of particle subpopulations [82].

Beginning with pioneering works of Barak and Webb [6] on the tracking of single fluorescently labelled lipoprotein particles and of Debrabander et al. [18] on intracellular motility, who introduced SPT to the field of biological physics, the technique was initially used to investigate lipid and protein diffusion on plasma membranes [2, 104].

On the other hand, single molecule[2] characterization and detection has prospered continuously since the early investigations of Moerner and Kador [63], Orrit and Bernard [71] and Schmidt et al. [85, 86].

Especially in recent time, both techniques could be combined to investigate the tracking of individual molecules in model membranes [85, 86, 89, 88] and single protein molecules in solution and in cells [51, 55, 56, 32].

Towards automation of the tracking procedure, Ghosh and Webb [31] presented one of the first automatic tracking algorithms followed by many other home-built, freely available and commercial ones.

The remarkable progress of SPT for cell biological applications is based on three technological pillars: the development of new optical devices (especially ultrasensitive CCD technology), the success in engineering highly-efficient recombinant fluorescent proteins, and the increase in computational power with the availability to process large amounts of data efficiently. In order to actually utilize the advances in computer technology towards an automated processing of image data,

[1] Although single dye molecules and other nm-size fluorescent particles like beads, quantum dots etc. potentially differ concerning their diffusive properties, from the view point of fluorescence microscopy, all particles with diameters well below the light wavelength are imaged as (resolution-limited) spots. Therefore, in the following, the single molecule tracking technique was included into single particle tracking (SPT).

[2] In this work, "single molecule fluorescence microscopy" means the detection of the fluorescence emission of single fluorophores.

efficient and reliable algorithms have to be used.

Processing of image data generally consists of reducing and compressing the wealth of information contained in an image sequence into a few numbers. Such a sequence comprises typically ten to several thousands of single images ("frames") of each ten to hundreds of pixels, for example. The procedure is highly non-linear, which currently still means that in the field of particle tracking most of the actual image processing is performed manually [78]. However, manual image analysis is prone to personal bias and time consuming which speaks for a maximum degree of automation of the analysis procedure.

In order to reach the goal of (semi-)automated quantitative image analysis, two important requirements have to be met: First (and trivially), the algorithm must be designed to process the data (it has to "see" the images and extract the features of interest) in order to process them correctly. Second, the algorithm must be characterized concerning accuracy and precision with which a specific parameter is extracted out of the data set.

Basically, there are three different sources of image analysis software: commercial, freely available and home-built.

- Concerning the commercial image analysis software, depending on the character and quality of the data to be handled, the specific features of interest might not be detected (or detected with obvious artifacts), especially if the images are noisy. Besides the limitation in flexibility, commercial software is usually hampered in their automated feature detection. Furthermore, besides a lack in transparency concerning the methods by which, for example, the spot trajectories are determined, the feature accuracy and precision has to be determined empirically[3] (via analysis of simulated data).

- Freely available semi-automated image analysis software includes, e.g., the solutions proposed in [78] (Java-applet for ImageJ software) and [41] (Java-applet). Providing the software with a small set of input parameters allows for a relatively versatile feature extraction on the basis of single spots. (In order to characterize several spots at the same time, the client-server model proposed in [83] can be utilized.) Sage et al. [78] and Sbalzarini et al. [83] characterize the ability of the specific algorithm to extract information about the trajectories of the particles present in the images analyzed.

- Development of home-built image processing software is generally the safest way to guarantee for optimal design and to understand its strength and weaknesses. In all pioneering works (reference see above) this way was cho-

[3] This is, of course, taken for granted in the case of freeware or home-built software.

sen, however, for the common SPT-user, the considerable programming effort should not be underestimated.

1.1.1. Motivation

In short, still today there is a lack of (semi-)automated, fast and reliable feature tracking algorithms capable of dealing with high-noise data and which are available for the general user who is not an expert in image analysis, statistics and programming.

Furthermore, most of the work in literature about the reliability of single particle tracking is focused on the influence of a limited SNR on the localization accuracy and / or precision of the spot determination [8, 89, 95, 68]. However, especially in case of step widths which are relatively large compared to the localization precision, the number of steps included into the analysis plays a crucial role for the final precision to which the diffusion constant can be determined [74, 81], in addition to the specific feature extraction method used [14].

1.2. Photoswitching fluorescent proteins

Since the first successful cloning of genetically encoded fluorescent proteins based on the Green Fluorescent Protein (GFP) of the jellyfish *Aequorea victoria*, a plethora of fluorescent proteins (FPs) were developed as mutants of GFP or similar coelenterate proteins during the last decade [105]. Due to their minimum interference with intracellular processes they are widely used for labeling proteins *in vivo* by forming protein fusion constructs. Applications like monitoring signaling pathways or intracellular trafficking have made the fluorescent proteins an invaluable tool for fluorescence based investigations in molecular biology.

Due to the undesirable autofluorescent background that is usually found in biological cells in the green-yellow spectral range development of fluorescent markers with a red-shifted emission wavelength is of high importance. In addition to the red fluorescent protein cloned from the *Discosoma* coral (*DsRed* or *drFP583*) [60], other proteins emitting in the red spectral range have been found including, e.g., *mRFP1* [12] and *eqFP611* [100]. Contrary to the tetrameric *DsRed* [93], the latter are monomers and therefore are much better suitable for the use as markers in fusion constructs.

Recently, another group of fluorescent proteins with altered spectroscopic properties has acquired considerable attention. In contrast to the previously mentioned proteins exhibiting a sprectral red-shift upon maturation, proteins like *Kaede* [3], *mcavRFP* [92], *rfloRFP* [92], *FDendFP* [72], *EosFP* [99, 67] and *Dronpa* [35], show a light-triggered red shift which can be reversible, as in case of *Dronpa*.

PS-CFP [15] switches from cyan to green emission triggered also by violet light (with which it is also excited, therefore, undesired conversion can occur). Recently, a new photoswitching fluorescent protein was engineered, *Dendra* [34], that is monomeric and can be photoswitched by illumination with blue (488 nm) light.

Compared to carbocyanine dyes, where photoswitching can only take place in the presence of triplet quenchers and absence of oxygen, recombinant proteins can also be used in the intracellular environment. Furthermore, photoswitchable proteins may provide striking experimental benefits in a cellular context where fluorescence-based single molecule tracking is difficult: By switching the fluorescence activity on at one specific time point, movement of single molecules in a tightly confined region of cellular compartments can be traced much easier [3].

All fluorescent proteins known today contain one or more 11-stranded β-barrels with a central helix in which the fluorophore, 4-(p-hydroxybenzylidene)-5-imidazolinone, is shielded from the environment [70]. Whereas in GFP the fluorophore is autocatalytically formed by a single oxidative cyclization of the triplet Ser-Tyr-Gly, the formation of the fluorophore in *DsRed* and *eqFP611* requires further maturation in another oxidation step [33, 100]. The fluorophore formation in the photoswitchable proteins proceeds also in two steps, however, the red-emitting fluorophore is formed upon absorption of violet light of around 400 nm [3]. According to a mechanism suggested in [62], the green fluorophore is cleaved between the amide nitrogen and the α-carbon in His62 upon excitation via a β-elimination reaction which requires the catalytic activity of the whole intact protein. A subsequently formed double bond results in an extension of the p-conjugated electron system thus producing a new red emitting fluorophore.

As is well known, fluorescence can deliver valuable information on structural dynamics and – naturally – the photophysical behavior of fluorophores. A striking feature of many FPs found so far is the dual band absorption at ca. 390–400 nm causing weak fluorescence around 460 nm and 475–510 nm which gives the strong fluorescence peak at 508 nm [13]. Investigations based on fluorescence spectroscopy have shown that this can be attributed to two distinct chemical forms, a protonated (neutral) and a deprotonated (anionic) form, with a pH dependent relative intensity of the respective absorption and emission peaks [58]. Understanding the intricate photophysics of GFP and its mutants – in particular, the influence of the structure and the conformational dynamics on the fluorescence characteristics of the proteins – offers the possibility to design FPs with desired properties. However, in an ensemble, fluorescent proteins often display heterogeneity related to the chemical structure and the electronic state of the molecules.

1.2.1. Motivation

Therefore, fluorescence studies on the single molecule level [101, 97] can provide more detailed information than conventional fluorescence techniques based on measuring parameters of ensembles of molecules. In particular, the reversible conversion reactions in FPs between the protonated and the deprotonated states taking place on short time scales (so-called flickering) were proven for first time by single molecule fluorescence methods including single molecule microscopy [86, 22, 56] and fluorescence correlation spectroscopy [38, 91, 59].

In a previous work [25], fluorescence correlation spectroscopy was utilized to investigate the fast flickering dynamics of *Kaede* protein which proved to be pH-dependent for the green (*grKaede*) but not for the red (*rKaede*) form. Based on a microchannel continuous flow technique the conversion reaction was studied and a conversion time of 40 ms was determined. Studies of very slow processes, however, were not accessible by these techniques.

Thus, employing the two-color single molecule fluorescence imaging technique, the photobleaching – and especially photoswitching – behavior of single fluorophores, e.g. fluorescent proteins, can be studied [84].

1.3. Goals of this thesis

Aim of this thesis was the successful

1. technical development
2. physical characterization and
3. application to biological systems

of the single molecule fluorescence imaging and -tracking technique based on an optical wide field microscope setup.

Technical development: To this end, on the one hand, the optical excitation and detection system had to be developed[4]. On the other hand, a versatile and robust image analysis algorithm had to be designed and implemented, tested and debugged.

Physical characterization: The physical properties of the optical setup as well as the features of the image analysis software had to be characterized on basis of parameters relevant for the experimental system.

[4] partly in co-operation with the workshop for precision mechanics at the MPI for Biophysical Chemistry, Göttingen

Application to biological systems: Two different biological systems could successfully be investigated by the single molecule imaging technique established in this thesis:

- Within a liquid lipid bilayer membrane of a giant unilamellar vesicle (GUV) consisting of a 50 : 50 mixture of cholesterol and DLPC, the diffusion constant could be determined to high precision and accuracy for two different temperatures.

- For single immobilized molecules of the fluorescent protein *Kaede*-GFP, the photobleaching and photobleaching behavior could be determined.

1.4. Outline

The thesis is subdivided into three major parts: The introduction and discussion of theoretical concepts (I), the description of the experimental methods (II) and the presentation of the results (III).

After the general introduction (chapter #1), part I starts with the concepts of fluorescence (chapter #2), continues with an overview of different optical microscopy techniques (including relevant aspects of CCD-technology) in chapter #3 to the detailed discussion of single molecule fluorescence microscopy (chapter #4).

Part II begins in chapter #5 with a description of the various components and the design of the wide field microscopy setup, followed by a presentation of the design of the image analysis algorithm and a consideration of the experimental procedure and potential artifacts (chapter #6). Additionally, in chapter #7 details of the preparation of the biological systems are discussed.

In part III the results of the thesis are presented. First, in chapter #8, the automated and simultaneous characterization of multiple spot-like features from single molecule fluorescence image sequences will be discussed. Besides issues of feature extraction, the determination of spot trajectories and the extraction of diffusion constants[5] are treated.

Chapter #9 briefly gives the results on the determination of the diffusion constant of the GUV membrane system.

The results of the investigations on the photobleaching and photoconversion behavior of *Kaede*-GFP protein are presented in chapter #10.

While the results are discussed already in each of the chapters #8 – 10, chapter #11 contains the summary and the conclusions with an outlook are given in chapter #12 .

[5]In the present context, a spot is the fluorescence image of a particle on the CCD chip.

Part I.

Theoretical background

2. Concepts of Fluorescence

Since this thesis deals with investigations based on fluorescence microscopy, basic principles of fluorescence shall be elucidated in the following. Dye molecules are characterized by the fact that the can absorb light of certain wavelengths λ_1. On the single molecule level, the photophysical model for this process is a transition from the ground state $^1S_0$ to the first electronic excited singlet state $^1S_1$ occurring on a very fast time scale (10^{-15} s). The photophysical transitions are conveniently displayed in a Jablonski diagram [57]:

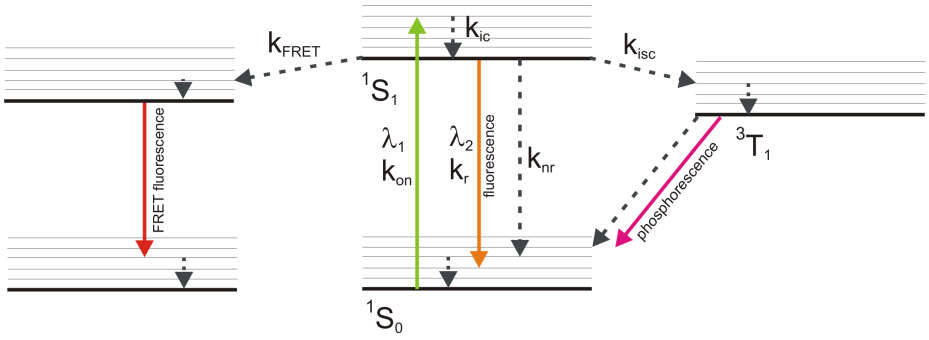

Figure 2.1.: Jablonski diagram displaying photophysical transitions. $^1S_0$: electronic ground state, $^1S_1$ ($^3T_1$): first electronic excited singlet (triplet) state; rate constants: k_{on} absorption, k_{ic} internal conversion, k_{isc} inter-system crossing, k_r radiative, k_{nr} non-radiative de-excitation, k_{FRET} fluorescence energy transfer; λ_1,λ_2: absorption and emission wavelength. Energy levels involved in the photophysical processes (here displayed: fluorescence, phosphorescence and fluorescence resonance energy transfer (FRET)) following the excitation of the molecule in one-photon-absorption (green arrow).

In the case considered here, the molecule is excited into a higher vibronic level of the $^1S_1$ state upon absorption of one photon. (Multi-photon excitation is not regarded here as it was not used during the experiments of this work.) Although quasi-forbidden, a fast (time constant $\tau_{ic} = k_{ic}^{-1} \sim 10^{-14} - 10^{-11}$ s) internal conversion process to the vibronic ground state of $^1S_1$ is mediated by collisions with solvent molecules. From the $^1S_1$ state with a life time τ_S the molecule can return to the ground state in various ways. Emitting a photon with a longer wavelength λ_2 will leave the molecule in a vibronic excited state before returning to the ground

state $^1S_0$, a phenomenon called fluorescence (k_r). The collisions of the dye with solvent molecules are also the reason for the broadening of the absorption- and the fluorescence emission spectra.

However, an excited molecule also can release the excess energy in nonradiative ways ($k_{nr}^{-1} \sim 10^{-9}\,\mathrm{s}$). In particular, collisions with specific molecules (solvent, oxygen, etc.) can quench the fluorescence. With small probability, the molecule can undergo a quasi-forbidden intersystem crossing via spin-flipping into the first electronic excited triplet state $^3T_1$. From this long-lived state ($\tau_T > 10^{-4}\,\mathrm{s}$) a return to the ground state $^1S_0$ is possible either by photon emission (phosphorescence) or nonradiatively.

As can be seen from Fig. 2.1, due to relaxation of state $^1S_1$ in excited vibronic levels of $^1S_0$, the emission wavelength is longer than the excitation by a value called the Stokes shift. The Stokes shift is a characteristic property of the fluorophore-solvent system and enables the spectral separation of the emission from excitation light by optical filters.

2.0.1. Quantum efficiency

The fraction of fluorescently de-excited $^1S_1$-molecules is defined as quantum efficiency:

$$\Phi_F = \frac{k_r}{k_r + k_{ic} + k_{isc} + k_{nr}} \tag{2.1}$$

The molecules of good fluorophores emit on average $10^5 - 10^6$ photons in total, whereas particular molecules can exceed the mean by multiples.

2.0.2. Saturation

Assuming a 3-step model as in Fig.2.1 (without FRET-transition), the fluorescence emission intensity I_{em} saturates with increasing excitation intensity I_{exc} according to [19, 66, 85]:

$$I_{em} = \frac{k_\infty \Delta t_{exc}}{1 + I_{sat}/I_{exc}} \tag{2.2}$$

with

$$I_{sat} = \frac{hc}{3\lambda_{exc}\sigma_0} \frac{\tau_S^{-1} + k_{isc}}{1 + k_{isc}\,\tau_T} \tag{2.3}$$

$$k_\infty = \frac{\eta_{det}\Phi_F}{\tau_S\,(1 + k_{isc}\,\tau_T)} \tag{2.4}$$

with I_{sat} as (excitation) saturation intensity, k_∞ as (emission) saturation rate, σ_0 as mean absorption cross section, λ_{exc} as excitation wavelength and η_{det} as detection efficiency.

2.0.3. Photobleaching

Besides being released in the ways described in Fig. 2.1, the absorbed energy can cause chemical reactions which change the photophysical properties of the fluorophore, so that fluorescence emission is quenched. Irreversible loss of fluorescence activity due to photochemical reactions from excited electronic states is called *photobleaching*.

In the case of, e.g., the dye Rhodamine 6G, two metastable dark states, the triplet ${}^3T_1$ and a radical anionic state, play a crucial role as educts for photobleaching reactions: either directly or after additional n-step ($n = 1, 2, 3, ...$) excitation (see [26] for references).

Reactions of the metastable states with oxygen can lead to a return to the ground state (reduced photobleaching) or to photophysically inactive products (enhanced photobleaching) [26].

3. Optical microscopy: basic concepts

3.1. Introduction to optical microscopy

In a typical far-field light microscope the intensity of light emanating from an object is measured after having passed through an optical system. Compared to the wavelength λ of light, object and detector are spatially clearly separated and the light waves are detected in their (electromagnetic) far-field. Opposite to this approach in near-field microscopes the light field is probed very close ($\sim \lambda$) to the origin of the light waves. In this thesis, only far-field microscopic systems were utilized and, hence, are considered further.

Among the far-field microscopes, there exist several strategies differing in the techniques used for sample illumination and light detection. Furthermore, for some of them the detected light has to superpose coherently on the detector as the phase information is crucial for contrast.

3.1.1. Fluorescence wide field microscopy

The wide field microscope

The most basic approach is implemented in the wide field microscope, where in the ideal case the object is illuminated in a homogeneous way.

For conventional wide-field microscopy coherence between light waves originating from different spots of the object is not desired as it can give rise to diffraction artifacts ("speckles"). Contrast, i.e. the difference in the signal intensity detected on different locations on the image plane, is achieved by incoherent superposition of the light and directly reflects the objects transmissivity.

However, for more advanced wide-field techniques like phase contrast or differential interference contrast (DIC) microscopy, coherence is of crucial importance for image formation [9]. Since they were not used in this thesis, they are not treated here any further.

The fluorescence microscope

To differentiate further, far-field light microscopy can be further divided into transmission and fluorescence microscopy. In transmission microscopy, the beam path and the wavelength of the light detected are identical to the one used for illumination. The fluorescence emission of fluorophore molecules is incoherent due

to its quantum nature and depends on the relative orientation between the exciting (illuminating) light field and the absorption and the emission dipole of the fluorophore. Because in many cases the dipole orientation is random, to a first approximation fluorescence emitted from an object may be regarded as isotropic. In the "epi-fluorescent" called implementation, the fluorescence light can be collected by the same objective used for excitation.

In this case, emission and illumination light are propagating in opposite directions and can comfortably be separated by optical filters.

3.1.2. Fluorescence confocal microscopy

An advanced fluorescence microscopy technique widely applied today is confocal laser scanning microscopy (LSM) In opposition to wide field microscopy, illumination in confocal laser scanning microscopy is realized by a focused laser beam scanning the object. In the detection pathway a pinhole is inserted so that only the fluorescence emission of the focal spot is detected [21].

3.1.3. Point spread function (PSF)

Before discussing the characteristics and differences of fluorescence wide field and confocal microscopy further, the concept of the point spread function determining the image acqusition shall be presented.

Both fluorescence wide field and confocal microscopy have one important feature in common: When an object (in object space Σ) is illuminated, the image of the whole object is the sum of the images of all the object's fluorescence emitters (in image space, Σ'). This incoherent linear superposition of the individual emission intensities is due to the statistical nature of fluorescence emission.

Because of this linearity the image generation can be described as convolution of the point spread function (PSF) and the real fluorescent intensity distribution [21].

The PSF is defined as the light intensity distribution (i.e., the "image") of a point source when imaged by the optical system (see Fig. 3.1).

Subsequently, an approximate PSF for a well-corrected lens shall be computed based on the following assumptions: (1) The optical system is linear, it does not scatter or absorb light and (2) the optical system is invariant, i.e. the PSF is independent of the object's position in the field of view (see [21], p.103f.).

For a light source with vacuum wavelength λ_{vac} which is imaged by a lens with the focal length f, the light amplitude $h(u, v)$ at position (u, v) is given by

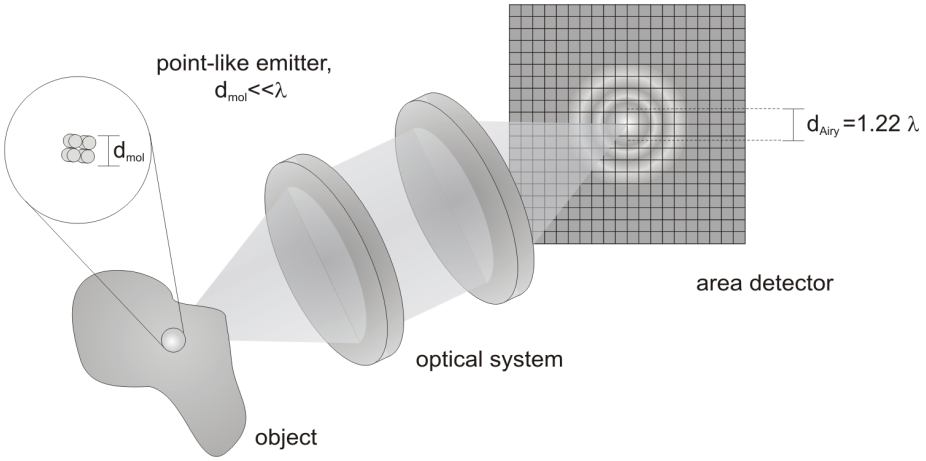

Figure 3.1.: Schematic representation of the microscope as imaging system. A subresolution object with diameter $d_{mol} \ll \lambda$ is imaged onto an area detector displaying a typical intensity distribution reflecting Fraunhofer diffraction (Airy pattern).

$$h(u,v) = -i\,\frac{2\pi\, n \sin^2\alpha}{\lambda_{vac}}\, A_f\, e^{iu/\sin^2\alpha} \int_0^1 J_0(v\rho) e^{-\frac{i}{2}u\rho^2}\, \rho d\rho \tag{3.1}$$

where A_f is the light amplitude at the distance of f and n the refractive index of the medium surrounding the light source. $\sin\alpha$ determines half the aperture angle, therefore, $n\sin\alpha$ gives the numerical aperture NA of the lens. J_0 is the Bessel function of the zeroth order of the first kind. u and v are the normalized axial and radial coordinates:

$$u = \frac{2\pi n sin^2\alpha}{\lambda_{vac}}\, z, \qquad v = \frac{2\pi n sin^2\alpha}{\lambda_{vac}}\, r \tag{3.2}$$

The point spread function PSF_l is then given by the light intensity $I(u,v)$:

$$\begin{aligned} I(u,v) &= h(u,v)\cdot h^*(u,v) \\ &= \frac{4\pi^2\, n^2 \sin^4\alpha\, A_f^2}{\lambda_{vac}^2} \left[\int_0^1 J_0(v\rho) e^{-\frac{i}{2}u\rho^2}\, \rho d\rho\right]^2 \end{aligned} \tag{3.3}$$

Following [9], separation of real and imaginary part yields

$$C(u,v) - iS(u,v) = 2\int_0^1 J_0(v\rho) e^{-\frac{i}{2}u\rho^2}\, \rho d\rho \tag{3.4}$$

and

$$C(u,v) = 2\int_0^1 J_0(v\rho)\cos(i\,u\rho^2/2)\,\rho d\rho \tag{3.5}$$

$$S(u,v) = 2\int_0^1 J_0(v\rho)\sin(i\,u\rho^2/2)\,\rho d\rho \tag{3.6}$$

Here, these functions may conveniently be approximated numerically by dividing $[0,1]$ into N intervals (with $N \gg 1$):

$$C(u,v) \approx 2\sum_{j=1}^{N} J_0\left(\frac{j\,v}{N}\right)\cos\left(\frac{j^2\,u}{2N^2}\right)\,\frac{j}{N^2} \tag{3.7}$$

$$S(u,v) \approx 2\sum_{j=1}^{N} J_0\left(\frac{j\,v}{N}\right)\sin\left(\frac{j^2\,u}{2N^2}\right)\,\frac{j}{N^2} \tag{3.8}$$

$I(u,v)$ follows as

$$I(u,v) = \frac{\pi^2\,n^2\sin^4\alpha\,A_f^2}{\lambda_{vac}^2}\left[C^2(u,v)+S^2(u,v)\right] \tag{3.9}$$

For the optical system, the point spread function PSF_{sys} is the product of the PSFs for the illumination and the detection efficiency, PSF_{ill} and PSF_{det}:

$$PSF_{sys} = PSF_{ill}\cdot PSF_{det} \tag{3.10}$$

In an (ideal) wide field microscope, $PSF_{ill}(\mathbf{r}')$ is constant for each point $\mathbf{r}'$ in object space reflecting an homogeneous illumination. PSF_{det}, however, can be approximated by I given above.

For a high-numerical objective with NA = 1.2 immersed in water ($n = 1.33$) and $\lambda_{vac}^{em} = 600\,\text{nm}$ as the emission wavelength and $A_f = 1$ as light amplitude, the calculated PSF_{wf}[1] is shown in Fig. 3.2 *a,c*. With the $\lambda_{vac}^{ill} = 540\,\text{nm}$ and $\lambda_{vac}^{em} = 600\,\text{nm}$ as the wavelength of the excitation and emission light, respectively, PSF_{conf} is displayed in Fig. 3.2 *b,d*.

[1] However, the real PSF of an arrangement which includes a high-numerical objective, the immersion medium, the cover slip and the sample (in medium) is not symmetric with respect to the focal plane due to the mismatch of refractive indices between the respective parts.

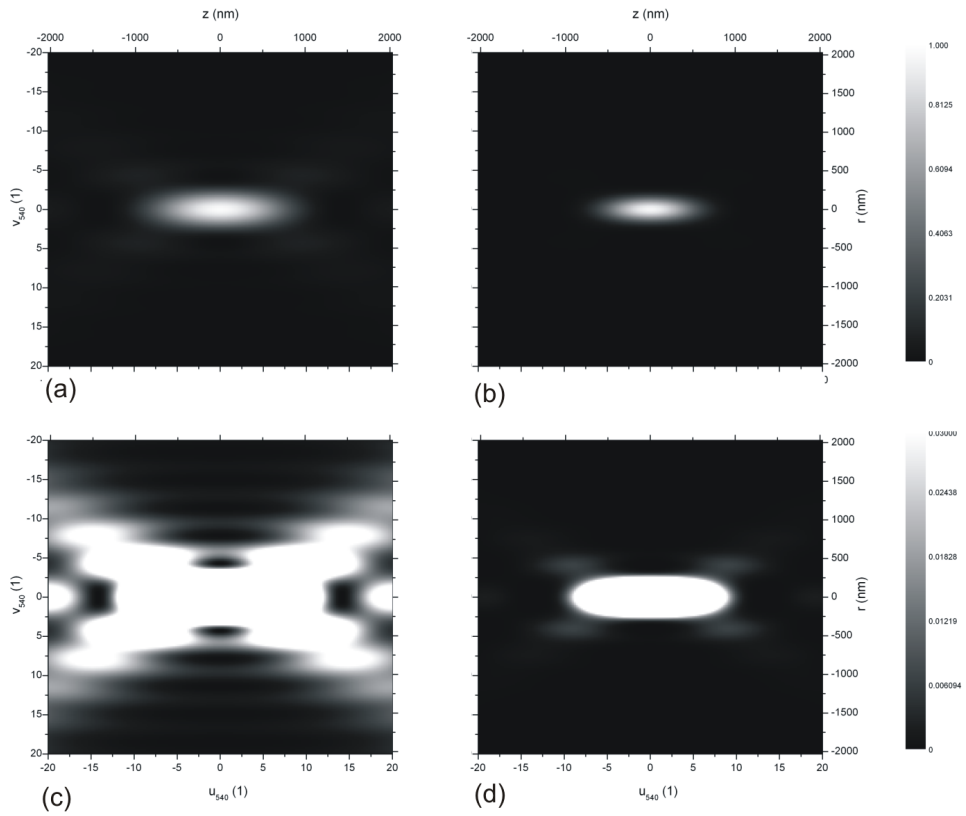

Figure 3.2.: Point spread function for wide field (a,b) and confocal illumination (c,d) as used in, e.g., laser scanning microscopes (a and c (b and d) display the same data with different scaling. n_{540} and v_{540} are the normalized axial and radial coordinates for $\lambda = 540\,\mathrm{nm}$.

3.2. Introduction to CCD-cameras

In the previous chapter, the image of a point-like object was discussed as it is obtained under (fluorescent) wide field and confocal microscopy.

In the present thesis devoted to single molecule imaging, wide CCD detectors were employed to detect the fluorescence of single mobile and immobilized molecules. Therefore, in this chapter an introduction to CCD detectors shall be given[2].

CCD ("charge coupled device") detectors are arrays of capacitors (*elements*[3]) embedded in a semiconductor matrix. By absorption of light, an electric charge can be generated and accumulated within each capacitor. Upon application of

[2]For further reference see [46, 47, 48]

[3]In this chapter, *elements* shall refer to the basic units of CCD detectors.

an (lateral) electric field, this charge can be shifted laterally to neighboring elements. The image of an element in object space is called "pixels" (from "picture elements").

Since CCDs are area detectors, all elements can detect at the same time. Therefore, the signals for all elements (i.e., for each detection volume in real space) are synchronized. This is contrary to a scanning approach (like in a laser scanning microscope), where each detection volume is sampled sequentially at a different time point.

History and basic concepts

Invented in 1969 originally as a memory device at AT&T Bell Labs, the basic concept of CCDs has been continuously under development until today. In the following, the most wide spread technical concepts of CCD design will be discussed.

- **Full frame CCD**

  Starting with the *full frame* CCD, the charge collected in an rectangular area of $N \times M$ elements (the "full frame") is shifted vertically to a shift register of size $1 \times M$. Subsequently, the respective charge in each element in the shift register is transferred horizontally to the read out element from where it is amplified and converted to units called counts. In order to avoid the collection of charge during the vertical line shift ("smearing"), light has to be blocked by a mechanical shutter during the shift process. Elements in all CCD chips have a built-in maximal electron storage capacity, the *well depth*. If exceeded, additional charge can not be collected any further, light signal is lost.

- **Frame transfer CCD**

  In the *frame transfer* CCD, only the upper $N/2 \times M$ elements are exposed to light; after the illumination time for one frame is over, the charge is quickly transferred to the lower part of the chip which is shielded against light exposure. From there, the charge acquired can be read out in a comparatively slow process like in the full frame CCD.
  Opposite to the full frame approach, no shutter is needed, however, at illumination times Δt_{exp} comparable to the vertical shift time Δt_h, smearing can occur nonetheless.

- **Interline CCD**

  To diminish smearing even at small Δt_{exp}, the *interline* CCD was developed. As in *frame transfer* CCDs, each charge is stored intermittently in light-shielded elements. Contrary to the approach treated before, vertical columns

of shielded elements are arranged in a pattern alternating with sensitive ones. Fast horizontal line shift allows for a strong reduction of smearing because the charge is shielded during the relatively slow vertical shifting.

- **Front/back-illuminated CCDs**

  To enhance sensitivity, so called *back-illuminated* CCDs (as compared to the traditional *front-illuminated* ones) were developed. In these devices, the rear surface of the device covered with a thinner semiconductor layer is exposed to light yielding a quantum efficiency Q_{CCD} of 90% and higher, which is an improvement of the front-illuminated systems having Q_{CCD} of ca. 60%.

- **Intensified CCDs**

  Whereas in the devices discussed above only the charge *after* the read out step prior to digitization is amplified, in the class of *intensified* CCDs (ICCDs) a multichannel plate (MCP) is mounted in front of the sensor to amplify the impinging light.

  Converted into photoelectrons which are amplified (up to several hundredfold) and re-converted into light, the light intensity finally reaching the CCD sensor is strongly increased. However, by employing a MCP an additional source of light noise is introduced[4]. Therefore, the overall improvement of the signal-to-noise of the camera counts in comparison to conventional low-noise CCDs has to be evaluated critically and depends upon the specific experimental conditions (light intensity, exposure time, etc.).

  The MCP of an ICCD can be gated on very short time scales ($\approx 100\,\mathrm{ns}$) which allows for a very high time resolution. In spectroscopic applications, for example, this can be a considerable advantage over all other camera concepts mentioned here.

- **Electron multiplication CCDs**

  Recently, a new type of CCD was invented amplifying the charge *before* the read out step. To that end, the charge is shifted through an additional *amplification register* on the chip with a tunable amplification gain. Compared to the *intensified* CCDs, this on-chip amplification introduces only a minute fraction of noise [77, 20].

3.2.1. Determination of signal-to-noise ratio (SNR)

Images are constructed out of single pixels based upon the detection of fluorescence photons in each element. Fluorescent molecules only emit a certain total

[4]For the treatment of camera noise, see next chapter.

number of photons until chemical conversion into a fluorescently inactive state (*photobleaching*). Additionally, the emission intensity per molecule and unit time, I_{em}, cannot be raised above a certain limit regardless of the experimental conditions (e.g., excitation intensity I_{exc}), due to *saturation*[5] (see also section 2.0.2 and [19, 66]).

Because of this limitation, it would be highly desirable to deduce the exact number of photons $I^{ph}(t)\Delta t$ hitting an element in the time interval $[t; t + \Delta t]$ from the respective number of counts $I^{c}_{det}(t)\Delta t$ detected by the CCD. However, this is not feasible due to the statistical nature of the conversion processes *and* additional deviations created during the detection/conversion processes (*noise*). Therefore, a characteristic figure of merit for the image quality is the signal-to-noise ratio (SNR) of each pixel.

Definition of SNR

The following arguments are based on the assumption of an stationary system with time dependent values $M(t)$, time average $\overline{M} = \langle M(t)\rangle_T = const$ and standard deviation $\overline{\sigma_M} = \langle \sigma_M(t)\rangle_T = const$. If not stated differently, $M \equiv \overline{M}$ and $\sigma_M \equiv \overline{\sigma_M}$. Values M^{ph} [M^e; M^c] are given in units of photons (ph) [photoelectrons (e); counts (count)].

With the above definitions, the SNR for a signal intensity $N(t)$ is given by

$$\mathrm{SNR} = \frac{N}{\sigma_N} \qquad \text{with } [\mathrm{SNR}] = 1. \tag{3.11}$$

For computation of the SNR, the units in which N and σ_N are expressed have to be considered. Because the noise σ_N is converted differently than the signal N, the specific expressions have to be adapted according to the units used as explained in the following (see Eqns. 3.25 and Appendix 13.1).

The SNR itself is dimensionless; of course, since the finally obtained intensity values measured by the CCD camera are expressed in counts, one could compute the SNR solely from the mean and noise values given in counts, N^c and σ^c_N. However, firstly, for the reason of systematic clarity and, secondly, due to the fact that the read out noise is usually given in photoelectrons, the unit dependent expressions (for ph, e and count) of the SNR shall be computed in the following part.

[5] To a first approximation, N_{max} is given by the inverse (finite) lifetime τ_r of the excited state $^1S_1$.

Conversion processes

Let us assume that a specific type of fluorophores emits on average N_0^{ph} photons per molecule and unit time Δt. Only a small fraction ζ of the N_0^{ph} photons pass the optical system and hit the CCD detector.

These N^{ph} photons are converted into N^e photoelectrons with the *quantum efficiency*

$$\eta = N^e/N^{ph} \qquad \text{with } [\eta] = \frac{\text{e}}{\text{ph}}. \tag{3.12}$$

Each photon yields either zero or one photoelectron (neglecting Auger effect or multi-photon effects etc.). The N^e photoelectrons are further digitized into N^c count with a *gain* g:

$$g = N^c/N^e \qquad \text{with } [g] = \frac{\text{e}}{\text{count}}. \tag{3.13}$$

So the mean value N results in:

$$\begin{array}{ccccc} \text{photons} & \overset{\eta}{\Rightarrow} & \text{photoelectrons} & \overset{g^{-1}}{\Rightarrow} & \text{counts} \\ g^{-1}\,\eta N^{ph} & = & g^{-1}N^e & = & N^c \end{array} \tag{3.14}$$

Further follows for the standard deviation σ_N (see Appendix 13.1):

$$g^{-1}\sqrt{\eta}\,\sqrt{\tfrac{\text{e}}{\text{ph}}}\,\sigma_N^{ph} \;=\; g^{-1}\sigma_N^e \;=\; \sigma_N^c \tag{3.15}$$

Sources of noise

The previous discussion so far only dealt with the conversion of the units of signal and noise but not of the noise sources. This shall be accomplished in this paragraph.

Two different, uncorrelated types of noise can be distinguished: Sample related ($\sigma_{N_{fl}}$) and detection related (σ_{det}) noise. Because they are statistically not correlated, the variances can be added to gain the total noise, σ_{to}:

$$(\sigma_{to})^2 = \left(\sigma_{N_{fl}}\right)^2 + (\sigma_{det})^2 \tag{3.16}$$

- Sample related noise: The origin of $\sigma_{N_{fl}}$ is the quantum nature of the fluorescence emission process. Therefore, only the mean number N_{fl} of detected photons can be known, the inherent random deviations obey a Poisson distribution (shot noise; see Appendix 13.1):

$$\frac{N_{fl}^{ph}}{\mathrm{ph}} = \left(\frac{\sigma_{N_{fl}}^{ph}}{\mathrm{ph}}\right)^2 . \tag{3.17}$$

Sample fluorescence $N_{fl,s}$ as well as all sorts of background fluorescence or stray light[6] $N_{fl,b}$ belong to this type[7]:

$$\left(\sigma_{N_{fl}}\right)^2 = \left(\sigma_{N_{fl,s}}\right)^2 + \left(\sigma_{N_{fl,b}}\right)^2 \tag{3.18}$$

- Detection related noise: The second type of noise shall be identified with fluctuations generated by conversion and read out processes. To this type *read out noise* σ_{ro} and *dark noise* σ_d can be assigned. However, $\sigma_d \ll \sigma_{ro}$ for short exposure times $\Delta t_{exp} \leq 1\,\mathrm{s}$:

$$\left(\sigma_D\right)^2 = \left(\sigma_{ro}\right)^2 + \left(\sigma_d\right)^2 \approx \left(\sigma_{ro}\right)^2 \tag{3.19}$$

Hence, the square of the total noise can be given (in units of photons, photoelectrons and counts):

$$\begin{aligned}
\left(\sigma_{to}^{ph}\right)^2 &= \left(\sigma_{N_{fl,s}}^{ph}\right)^2 + \left(\sigma_{N_{fl,b}}^{ph}\right)^2 + \left(\sigma_{ro}^{ph}\right)^2 + \left(\sigma_{d}^{ph}\right)^2 \\
&\approx \left(N_{fl,s}^{ph} + N_{fl,b}^{ph}\right) \cdot \mathrm{ph} + \left(\sigma_{ro}^{ph}\right)^2 \qquad (3.20) \\
\left(\sigma_{to}^{e}\right)^2 &= \left(\sigma_{N_{fl,s}}^{e}\right)^2 + \left(\sigma_{N_{fl,b}}^{e}\right)^2 + \left(\sigma_{ro}^{e}\right)^2 + \left(\sigma_{d}^{e}\right)^2 \\
&\approx \left(N_{fl,s}^{e} + N_{fl,b}^{e}\right) \cdot e + \left(\sigma_{ro}^{e}\right)^2 \qquad (3.21) \\
\left(\sigma_{to}^{c}\right)^2 &= \left(\sigma_{N_{fl,s}}^{c}\right)^2 + \left(\sigma_{N_{fl,b}}^{c}\right)^2 + \left(\sigma_{ro}^{c}\right)^2 + \left(\sigma_{d}^{c}\right)^2 \\
&\approx \left(N_{fl,s}^{c} + N_{fl,b}^{c}\right) \cdot g^{-1} \cdot e + \left(\sigma_{ro}^{c}\right)^2 \qquad (3.22)
\end{aligned}$$

With N and σ_N computed in the respective units, the SNR follows according to Eqn. 3.11:

[6] assumed here to be Poisson distributed

[7] Eqn. 3.18 holds for all units, ph, e and count.

$$\text{SNR} \approx \frac{N^{ph}_{fl,s}}{\sqrt{\left(N^{ph}_{fl,s} + N^{ph}_{fl,b}\right) \cdot \text{ph} + \left(\sigma^{ph}_{ro}\right)^2}} \tag{3.23}$$

$$= \frac{N^{e}_{fl,s}}{\sqrt{\left(N^{e}_{fl,s} + N^{e}_{fl,b}\right) \cdot e + \left(\sigma^{e}_{ro}\right)^2}} \tag{3.24}$$

$$= \frac{N^{c}_{fl,s}}{\sqrt{\left(N^{c}_{fl,s} + N^{c}_{fl,b}\right) \cdot g^{-1} \cdot e + \left(\sigma^{c}_{ro}\right)^2}} \tag{3.25}$$

Eqn. 3.22 offers a way to determine the gain g: When $\left(\sigma^{c}_{to}\right)^2$ is plotted as function of $N^{c}_{fl,s}$, g is the inverse slope of the curve (see section 5.3.1).

4. Single molecule fluorescence microscopy

In conventional fluorescence microscopy images recorded contain the fluorescence signal of an ensemble of fluorophores. However, ensemble averages can blur the real heterogeneity present in the system under investigation. Additionally, increasing the concentration of fluorescently labelled molecules can interfere with the properties of the system. A remedy to both issues are techniques based on single molecule measurements.

4.1. Single molecule imaging

The principal goal of *single molecule imaging* is to determine certain properties (position, emission intensity) by (optically[1]) imaging each single molecule separately. As mentioned above, this approach avoids potentially problematic averaging over ensembles containing *systematic* heterogeneity.

Contrary to the conventional approach where from an ensemble mean the properties of single units are deduced, here the opposite direction is chosen: from measurements on single molecules properties of the ensemble – or sub-ensembles – can be obtained. If changes in the system affect the fluorescence signal over time, *single molecule tracking* can be employed to determine the position and emission intensity as a function of time.

In the following paragraph several methods to fit fluorescent spots are presented. Subsequently, the term resolution is introduced and the precision to fit the lateral spot position as well as the spot height is discussed.

4.1.1. Spot fitting methods

Center-of-intensity (COI) method

To determine the position of a fluorescent object, one of the most straightforward ways is to compute its center-of-intensity (COI). This is especially obvious for sub-resolution particles like molecules whose image is given by the point spread function. However, especially low signal-to-noise values disfavor the COI method compared to a model based approach (like fitting the spot to a 2D-Gaussian).

[1] Besides fluorescence microscopy also electron microscopy techniques and atomic force microscopy, AFM, is used.

Approximation of the PSF by a 2D-Gaussian

The most common approach to gain the lateral position of a spot is to fit it to a 2D-Gaussian model mimicking the real (noisy) spot. Besides the (x, y)-position, also the spot height $I(x, y)$, the width $\sigma(x, y)$ and an additional background z_0 can be determined with a (non-linear) fitting routine.

In this thesis, only the fitting to a 2D-Gaussian model was used due to the typically very low SNR in the images.

4.1.2. Accuracy, precision and resolution

Before discussing the *localization precision* of the imaging system used, a short definition of the respective terms shall be given:

Accuracy: A measure of *reliability*; the difference between the true value N of a measured quantity and the most probable value $\overline{N} = \frac{1}{n}\sum N_i$. It gives the *systematic* error.

Precision: A measure of *repeatability*, usually given by the standard deviation of an ensemble of measurements N_i: It signifies the *statistical* error.

Unfortunately, in most of the literature the term localization *accuracy* has been established as a measure of the statistical error [8, 89, 68]. With Thompson et al. we define the localization precision as the statistical error in position determination [95]. Therefore, this definition shall be used further.

4.1.3. Lateral resolution

There is no unique concept of resolution, hence, there are different definitions of the term.

Abbe resolution Resolution defined by the Abbe limit is given by the FWHM (full width at half maximum) of the Airy disk [1]

$$\Delta x_A \simeq \frac{\lambda}{2\mathrm{NA}} \tag{4.1}$$

Rayleigh resolution The Rayleigh limit is given as the distance between the central maximum and the first minimum of the intensity of the Airy pattern generated by the optical system [76].

$$\Delta x_R \simeq 0.61\,\frac{\lambda}{\mathrm{NA}} \tag{4.2}$$

Sparrow resolution In fluorescence microscopy, the Sparrow limit is defined as the minimum distance of two equally fluorescing point objects so that no intensity minimum exists between both images (under the condition of arbitrary high emission intensity) [40]) :

$$\Delta x_S \simeq 0.48 \frac{\lambda}{\mathrm{NA}} \tag{4.3}$$

For images generated by real detection systems various sources of noise are present, so that the maximal resolution can only be approximated by the limits given above and, therefore, have to be validated under the specific experimental conditions given.

4.1.4. Localization precision

For the determination of the lateral spot position the localization *precision* is of special interest as it gives the degree of reliability of the position determination.

Therefore, considerable attention has been paid to this issue in the literature [8, 89, 95, 68]. Although the optical resolution is diffraction limited and in the order of $\lambda/2$, the mean position of a spot can be determined with a ten or more times higher precision which is eventually only limited by the number of photons collected [8].

Localization in center-of-intensity approach

If only photon shot noise is present and assuming that the PSF behaves like a 3D-Gaussian with the lateral standard deviation σ_{xy}, a photon can be localized in the $x-y$-plane with a precision of also σ_{xy} [42]. Hence, for n photons detected the localization precision shrinks to

$$\overline{\sigma}_{xy} = \frac{\sigma_{xy}}{\sqrt{n}} \tag{4.4}$$

However, if also read out noise is present or if the profile is non-Gaussian, the situation turns out to be more complicated [68].

Since the COI-approach was not followed in this work, no further emphasis is given on the specific localization precision.

Localization precision approximated by Fisher information matrix

Several approaches to determine the localization precision go back to [8] where the problem is approached by the least-square criterion. Ober et al. criticize this method as problematic if the underlying intensity probability distributions are not

η	60%
A	$100,000\,\mathrm{ph/s}$
Δt_{exp}	$10\,\mathrm{ms}$
NA	1.2
λ_{em}	$520\,\mathrm{nm}$
Δr_{loc}^0	$2.8\,\mathrm{nm}$

Table 4.1.: Typical experimental values [68]

Gaussian. This would be the case in single molecule images with a low number of photons which are essentially Poissonian distributed[2]. Furthermore, Bobroff approximated the (single molecule) image profile with a 2D-Gaussian which might be problematic if the single molecule is a certain distance out of the focal plane.

Ober et al. suggest a different approach based on the statistical theory of the Fisher information matrix $\mathcal{I}(P)$ [50] with $P(x, y)$ the real position of a molecule. Then the inverse of $\mathcal{I}(P)$ can provide a lower bound for the variance of an unbiased estimator[3] $\tilde{P}$:

$$var(\tilde{P}) \geq \mathcal{I}^{-1}(P) \tag{4.5}$$

According to Ober et al., any "reasonable" estimator $\tilde{P}'$ has an asymptotic variance equaling the inverse of $\mathcal{I}^{-1}(P)$ [75, 103, 50]

Using the maximum likelihood estimator, they give the fundamental limit of the localization accuracy by

$$\Delta r_{loc}^0 = \frac{\lambda_{em}}{2\pi\,\mathrm{NA}\,\sqrt{\eta A\,\Delta t_{exp}}} \tag{4.6}$$

with λ_{em} as emission wavelength, NA as numerical aperture, η the detection efficiency of the optical system, A the emission rate of the molecule and Δt_{exp} the exposure (aquisition) time. (For typical experimental values see Tab. 4.1.)

Thus, the fundamental limit for the localization precision according to Eqn. 4.6 turns out to be 2.8 nm. However, for the consideration of a pixelated detector and the presence of photon shot and read out noise, the fundamental limit has to be corrected by a lengthy factor given in [68]. Under the experimental conditions used typically for this thesis, the real limit of the localization precision Δr_{loc} is

[2] In the Gaussian case, the least-square estimate is a maximum-likelihood estimate whereas in the Poissonian case it is not [98, 37].

[3] An unbiased estimator $\tilde{P}$ gives the correct mean of P.

M	60
Δx_{pix}	$0.1075\,\mu$m
Δr_{loc}	$\approx 8\,$nm

Table 4.2.: Experimental values for this thesis (estimated from [68])

probably in the range of 8 nm[4] (see Tab. 4.2 with M as magnification and Δx_{pix} as the pixel size in object plane).

Although no simple relationship between the localization accuracy and the signal-to-noise ratio can be given, simulations on basis of the experimental parameters used provide a good estimate of the effective SNR (see section 8.2).

Localization in fitting approach by 2D-Gaussian

Approximating the PSF by a 2D-Gaussian and under the (disputable) assumption that the noise is Gaussian-distributed so that the least-squares estimate can be used [8], Thompson et al. give Δr_{loc} as:

$$\Delta r_{loc} = \left[\frac{\sigma_{xy}^2 + a^2/12}{n} + \frac{4\sqrt{\pi}\,\sigma_{xy}^3}{a\,n^2}\,\sigma_{ro}^2 \right]^{1/2} \tag{4.7}$$

with σ_{xy} as standard deviation of the PSF (Gaussian or other), n total number of photons collected, a pixel length and σ_{ro} as read out noise. (To avoid confusion, σ_{xy} and σ_{ro} is given as in units of length and photons, respectively.)

This result is qualitatively comparable to [51] but has a more compact form (see experimental part, section 8.2).

4.2. Single molecule tracking

4.2.1. Introduction to motility

It is a trivial fact that organic life requires the turnover of energy and matter in the course of metabolism. On a cellular level this is achieved by actively driven transport or by diffusion. Especially the intracellular active transport of "cargo molecules" has gained tremendous attention in recent years [45]. Single enzyme molecules ("molecular motors") transport vesicles, e.g. under consumption of energy like ATP in between different loci within the cell. However, many biological phenomena rely – at least partly – upon "simple" diffusive processes, e.g. the transport of water through aquaporin complexes within the cell membrane [17], the

[4] This value is extracted from the Figs. 4b and 6b in [68]

small-scale distribution of lipid molecules in cellular membranes[5] or the exchange of neurotransmitters in the synaptic cleft. Even the (overall) directed motion of motor proteins themselves sometimes involves diffusive motion, as in the case of KIF1A, a monomeric form of kinesin [69, 65].

While in this thesis only Brownian diffusive motion was investigated, the nature of diffusion will be discussed in the following section.

4.2.2. Diffusion

The random thermal motion of microscopic particles was first discovered in 1828 by the British botanist R. Brown[6] [11]. The importance of the *Brownian motion* (BM; also called *normal* diffusion) has unfolded in two ways: First, since it is caused by random thermal velocity fluctuations of molecules, its consequences determine the behavior of many living and non-living systems [7, 65]. Second, historically it was very influential in the acceptance of the "atomistic hypothesis" and molecular theory (see for example A. Einstein's work on Brownian motion[7] [28]).

Principles of diffusive motion

Although BM was first observed on microscopic particles several orders of magnitude bigger than e.g. lipid molecules, the theory also extends to the scales of (bio-)molecules. In the following, both objects – μm size microscopic particles and molecules – will be referred to as "particles".

The BM of a particle is characterized by different parameters, e.g. the particle size, the viscosity and the temperature of the solvent: The larger the particle and the higher the viscosity, the smaller the movement. Additionally, BM is stable over time; the motion persists as long as the particle is immersed in the fluid. External fields (gravity, electro-magnetic) seem to have no effect [61].

If a particle is suspended in a liquid, it collides randomly at a rate of $k_{coll} \approx 10^{12} s^{-1}$ with neighboring (solvent) molecules due to thermal motion [65]. The resulting transfer of kinetic energy and momentum leads to a random walk which has structure on all length scales: Even with different observation rates k_{obs} the displacements $\vec{r}(n\Delta t), n = 1, 2, 3, \ldots$ show self-similarity (as long as $k_{obs} = 1/\Delta t \ll k_c$). Brownian diffusion is a Markovian process: If it is assumed as a discrete-time

[5] Regardless of the existence and role of liquid-ordered microdomains ("lipid rafts"), the Brownian motion moves the lipid molecules within the membrane as well as the membrane as a whole, as many molecular dynamics simulations show.

[6] A very nice treatment of Brownian motion can be found in [61].

[7] According to [65], Einstein's Ph.D. thesis, on the viscosity of suspensions, remains his most heavily cited scientific paper till today.

process, the probability to find the particle at position $\vec{r}(n\Delta t)$ after step n only depends on its position $\vec{r}((n-1)\Delta t)$ after step $n-1$ (with Δt as lag time).

To give a short analysis of 3D-Brownian motion, every displacement (step) shall be decomposed into independent 1D-steps. Further, since collisions occur very frequently and $k_{obs} \ll k_c$, a fixed collision rate $k_{c,f}$ and a fixed step width Δx with

$$\Delta x \ll \langle r(\Delta t)\rangle, \qquad r = |\vec{r}(n\Delta t) - \vec{r}((n-1)\Delta t)|$$

shall be assumed. In the general case, when p gives the probability for a particle to step to the right (in $+x$-direction), the total probability that a particle takes exactly k steps (of n times in total) to the right is given by the binomial distribution [7]

$$P_B(k;n,p) = \frac{n!}{k!(n-k)!}\, p^k\, (1-p)^{n-k}. \tag{4.8}$$

For the total displacement $x(k,n)$ holds

$$x(k,n) = [k-(n-k)]\Delta x = [2k-n]\Delta x \tag{4.9}$$

with the mean displacement

$$\begin{aligned} \langle x(n)\rangle &= [2\langle k\rangle - n]\Delta x \\ &= [2np - n]\Delta x \\ &= [n(2p-1)]\Delta x \end{aligned} \tag{4.10}$$

and the mean square displacement

$$\begin{aligned} \langle x^2(n)\rangle &= \langle \left([2k-n]\Delta x^2\right)^2\rangle \\ &= [4\langle k^2\rangle - 4\langle k\rangle n + n^2]\Delta x^2 \\ &= [4\left(n^2p^2 + np(1-p)\right) - 4np\cdot n + n^2]\Delta x^2 \end{aligned} \tag{4.11}$$

With $p = 0.5$ (no bias) one gets

$$\langle x(n)\rangle = 0 \tag{4.12}$$

and

$$\langle x^2(n)\rangle = n\Delta x^2. \tag{4.13}$$

If n and np both become very large, the binomial distribution approximates a Gaussian distribution [7]:

$$P_G(k)\,dk \;=\; \frac{1}{\sqrt{2\pi\sigma^2}}\,e^{-\frac{(k-\mu)^2}{2\sigma^2}}\,dk, \tag{4.14}$$

with $P_G(k)\,dk$ as the probability to find a value in the interval $[k; k+dk]$; The mean value is given by $\mu = \langle k\rangle = np$ and the variance by $\sigma^2 = np(1-p)$.

Defining the deviation from the mean value $y = k - np$ and transforming into real space,

$$\tilde{\sigma}^2 \;=\; n\Delta x^2 \tag{4.15}$$
$$\tilde{y} \;=\; y\Delta x \tag{4.16}$$
$$t \;=\; n\,\Delta t, \tag{4.17}$$

one gets

$$\begin{aligned}\tilde{P}_G(\tilde{y},t)\,d\tilde{y}\,dt \;&=\; \frac{1}{\sqrt{2\pi\tilde{\sigma}^2}}\,e^{-\frac{\tilde{y_k}^2}{2\tilde{\sigma}^2}}\,d\tilde{y}\,dt\\ &=\; \frac{1}{\sqrt{2\pi n\Delta x^2}}\,e^{-\frac{\tilde{y}^2}{2n\Delta x^2}}\,d\tilde{y}\,dt\\ &=\; \left(2\pi t\Delta x^2/\Delta t\right)^{-1/2}\,e^{-\frac{\tilde{y}^2}{2\Delta x^2}\cdot\frac{\Delta t}{t}}\,d\tilde{y}\,dt\end{aligned} \tag{4.18}$$

as probability for a particle to displace itself from $\tilde{y}(0) = 0$ to $[\tilde{y}; \tilde{y}+d\tilde{y}]$ within $[t; t+dt]$[8].

Diffusion on grounds of BM can be described macroscopically by the dependence of concentration $C(\vec{r},t)$ on time t and place $\vec{r}$ with the diffusion equation (2. Fick's Law):

$$\frac{\partial}{\partial t}\,\delta C(\vec{r},t) = D\,\nabla^2_{\vec{r},n}\,[\delta C(\vec{r},t)] \tag{4.19}$$

with D as the diffusion coefficient. The solution for Eqn. 4.19 has also the form of a Gaussian distribution[10]:

$$C(\vec{r},t) = \;\frac{C_0}{(4\pi Dt)^{n/2}}\,e^{-\frac{(\vec{r}-\vec{r}_0)^2}{4Dt}} \tag{4.20}$$

with $\nabla_{\vec{r},n}$ as the n-dimensional gradient operator[9].

[8] Only the 1D-case considered here. ("˜" will be omitted below.)
[9] provided that $C(\vec{r}_0,0) = C_0\,\delta(\vec{r}-\vec{r}_0)$

Comparing Eqn. 4.18 and 4.19, enables to connect microscopic (Δx, Δt) with macroscopic values (D)("Einstein-Smoluchowski-Equation"):

$$D = \frac{\Delta x^2}{2\Delta t}. \tag{4.21}$$

4.2.3. Methods of trajectory analysis

As mentioned above, in order to to characterize the mode of motion of particles, the displacements within the trajectories are analyzed[10]. In the following, two different approaches shall be discussed: the mean square displacement (MSD) and the displacement histogram (DH).

In MSD diagrams the average of the squared displacement $\langle r^2(t)\rangle$ is plotted versus the lag time t. The MSD(t) is then fitted to a model function (see below). Sometimes error bars for MSD(t) are given to illustrate the degree of precision, however, subpopulations of particles concerning e.g., the motion behavior, can not be detected due to averaging.

A complementary approach is given by computing the probability distribution of the step distances via the step distance histogram (DH). For a fixed lag time t the DH is computed and the parameters of an appropriate model function are fitted (see below). Compared to the MSD approach, subpopulations can be detected from one given t, whereas the characterization of the mode of motion requires a set of DH plots.

Mean square displacement

If a trajectory is recorded in discrete steps, the mean square displacement $\langle \Delta r(t)\rangle$ at time $t = k\,\Delta t$ can be determined[11]:

$$\begin{aligned} \mathrm{MSD}(k\,\Delta t) &= \langle (r(k\,\Delta t)^2\rangle \\ &= \frac{1}{n-k}\sum_{j=1}^{n-k} \left(\,\vec{r}\,[(j+k)\Delta t] - \vec{r}\,[j\Delta t]\,\right)^2, \quad k = 0,\ldots,n-1. \end{aligned} \tag{4.22}$$

This process is illustrated in Fig. 4.1 for a trajectory of a fluorophore diffusing within an artificial lipid bilayer membrane.

To extract information about the nature of the diffusion process and to parameterize it (e.g. the diffusion coefficient), in general the MSD computed from a

[10] A thorough introduction into single particle tracking analysis is given by [74].
[11] Here, averaging is performed over all data points following [81].

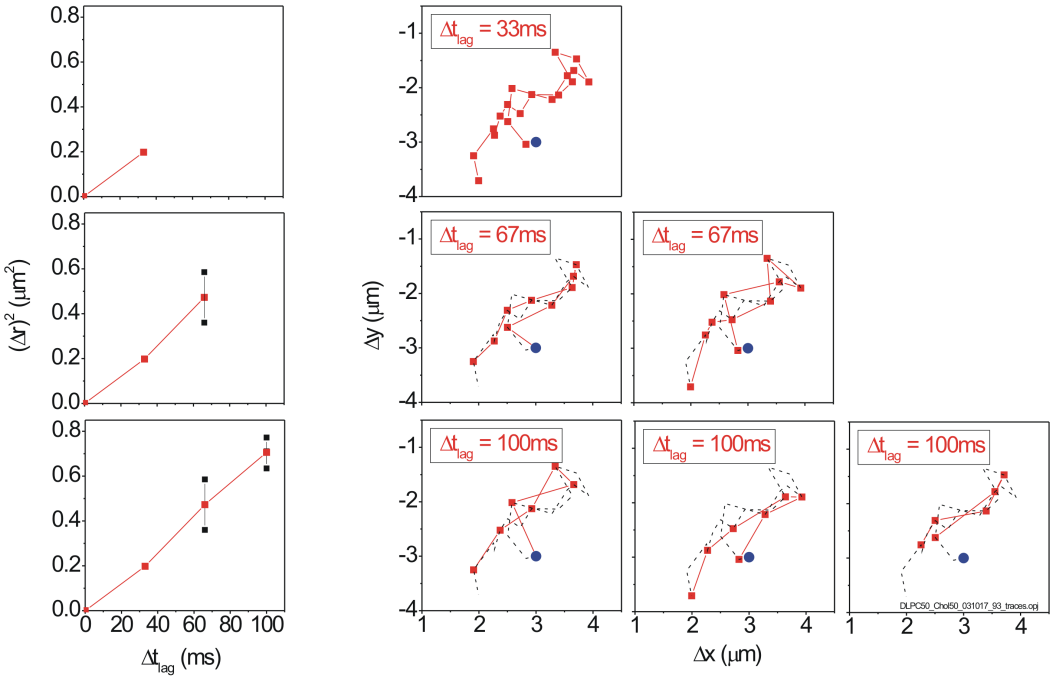

Figure 4.1.: Mean square displacement (MSD) of a trajectory of a single fluorescent DiI-C_{18}-molecule in a DLPC:cholesterol (50:50) artificial lipid bilayer membrane (blue dot: trace origin). The mean square displacement is computed for the first tree steps: *upper row*, t_{lag} : 33 ms (1 step); *middle row*, t_{lag} : 67 ms (2 steps); *lower row*, t_{lag} : 100 ms (3 steps). The MSD of the n^{th} step is computed as the average of n (dependent) sub-trajectories.

set of trajectories (or even a single sufficiently long one) has to be fitted to an appropriate model function.

Although for this thesis, the systems under investigation only display Fickian diffusive motion[12], for completeness also other, in biological systems frequently encountered modes of motion shall be briefly discussed concerning their implication for the MSD model function:

[12]For this mode of motion, the mean square displacement and the Gaussian distribution of displacements grow linearly with the lag time.

$$\langle r^2(t)\rangle = 4Dt \qquad \text{Fickian (normal) diffusion} \qquad (4.23)$$

$$\langle r^2(t)\rangle = 4Dt^{\alpha} \qquad \text{anomalous diffusion} \qquad (4.24)$$

$$\langle r^2(t)\rangle = 4Dt + (vt)^2 \qquad \text{directed motion with diffusion} \qquad (4.25)$$

$$\langle r^2(t)\rangle \simeq \langle r_C^2\rangle \left[1 - A_1 e^{-\frac{4A_2 Dt}{\langle r_C^2\rangle}}\right] \qquad \text{corralled motion} \qquad (4.26)$$

The four different modes of motion are described in more detail in [82].

- **Fickian (normal) diffusion**

  As discussed already above (Eqn. 4.13), in case of normal diffusion the MSD is linear in time with a slope of $4D$, if the trajectory is 2D or projected on a 2D-plane[13].

- **Anomalous diffusion**

  For $\alpha > 1 (< 1)$ the correct term is super(sub)-diffusion. Linear at short times, the slope of the MSD becomes flatter for longer times (trajectories). The physical idea behind this diffusion model is a random array of continuously changing traps with a broad distribution of energies so that no average residence time can be determined [29]. (The continuous-time random walk model (CTRW) comes to the same shape at long times [64].)

- **Directed motion**

  In the presence of an external flow field or if pulled, e.g., by motor proteins, directed motion of a particle, usually combined with Brownian diffusion, can be observed.

- **Corralled motion**

  If the particle is trapped so that it can only move within a confined region, its MSD will display an upper threshold. Like anomalous diffusion, the MSD is linear for small time scales when it does not feel the boundaries.

Assuming normal diffusion, Fig. 4.2 (a) gives an example where a set of trajectories were analyzed by fitting the mean square displacement.

[13] In case particles move in 3D and the traces can be also recorded in 3D, the respective slope of the MSD is $6D$.

Displacement histogram

If the displacements for a given lag time t are distributed as expected for normal diffusion, the distribution function is given according to a Rayleigh distribution (see also Eqns. 4.18, 4.21 and 9.1):

$$P_{DH}(r,t)\,dr = \frac{r}{2Dt} \times \exp\left(-\frac{r^2}{4Dt}\right)\,dr \tag{4.27}$$

with r as 2D-projection of the displacement between steps $\vec{r}_1(t')$, $\vec{r}_2(t'+t)$. For the same set of traces as used in the MSD analysis, an example of the corresponding DH plot is given in Fig. 4.2 (b).

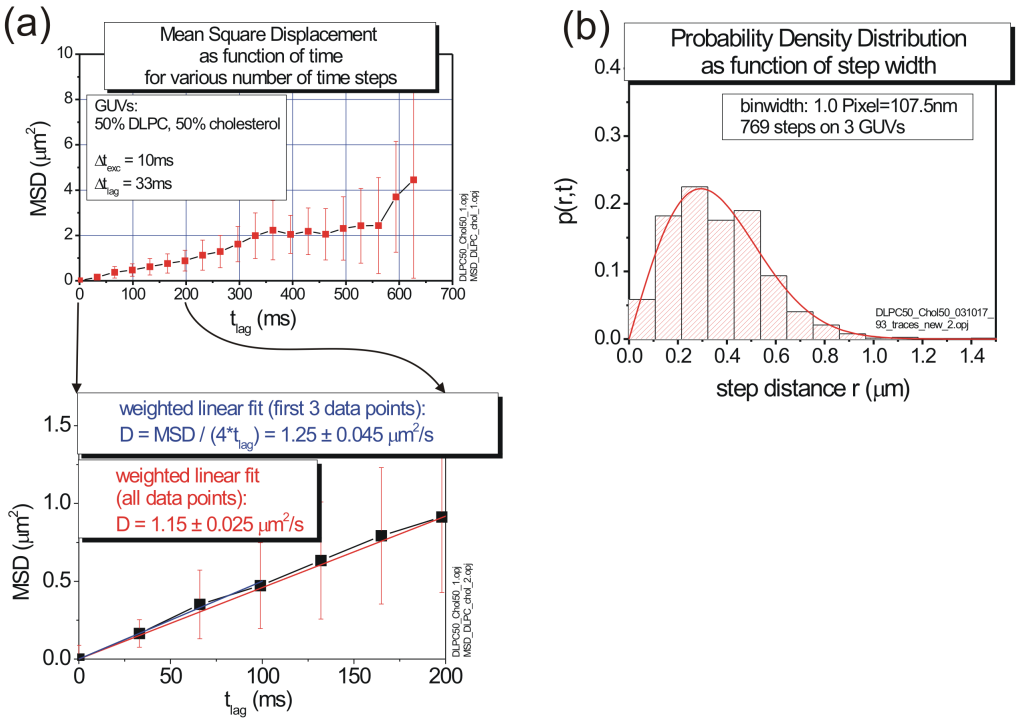

Figure 4.2.: (a): Example for MSD-analysis of a set of trajectories. Single fluorescent DiI-C_{18}-molecules diffusing in a DLPC : cholesterol (50 : 50) artificial lipid bilayer membrane were localized and the MSD of the trajectories determined. $\Delta t_{exp} = 10$ ms, $\Delta t_{lag} = 33$ ms; All steps were used for MSD computation. (b): Example for a displacement histogram of a set of trajectories. Single fluorescent DiI-C_{18}-molecules diffusing in a DLPC : cholesterol (50 : 50) artificial lipid bilayer membrane were localized and the displacement for lag time $\Delta t_{lag} = 33\,\text{ms}$ computed.

Caveats

Tracking particles in order to characterize their mode of motion suffers from several sources of errors which shall be discussed in the following.

Problems common to both MSD and DH

- **localization precision**

  Generally, the precision of particle localization is crucial for the further characterization of the mode of motion, whether MSD or DH is used. Following [79], a *static* and a *dynamic* error in the localization precision shall be distinguished. The static error is the consequence of the pixel noise (photon shot noise, read out noise, ...) and occurs even if completely immobilized particles are imaged. The dynamic error is the consequence of the finite image acquisition time t_{exp} during which the particle moves. Both errors can be corrected for by introducing additional offsets:

$$4Dt \quad \rightarrow \quad 4Dt - \underbrace{4/3 \cdot Dt_{exp}}_{dynamic} + \underbrace{\sigma_{loc}^2}_{static} \tag{4.28}$$

  Concerning the MSD analysis, this leads to a correction in Eqn. 4.23:

$$\langle r^2(t) \rangle \quad = \quad 4Dt - 4/3 \cdot Dt_{exp} + \sigma_{loc}^2 \tag{4.29}$$

  For the displacement histogram, a decrease in localization precision causes a similar change as to Eqn. 4.27:

$$P_{DH}(r,t)\,dr \quad = \quad \frac{r}{2Dt - 2/3 \cdot Dt_{exp} + \sigma_{loc}^2/2} \times \exp\left(-\frac{r^2}{4Dt - 4/3 \cdot Dt_{exp} + \sigma_{loc}^2}\right) dr. \tag{4.30}$$

  If $\sigma_{loc}^2 \ll 4/3 \cdot Dt_{exp}$, the lag time t becomes $t - t_{exp}/3$. Furthermore, if both the static and the dynamic errors are small compared to the average displacements, other sources of error (like erroneous linking or simply the statistical fluctuation in displacement size[14]) can contribute much more to the total error.

  However, under the above assumptions (see section 8.2) the correction $t \rightarrow t - t_{exp}/3$ needs to be applied for analysis of the specific data.

[14] especially if the number of steps included into the MSD or DH analysis is small, e.g. < 100;

- **Erroneous linking of spot trajectories**

  Generally, although all particles present in a set of images may have the same properties – so that individual differences in displacement among the trajectories are caused by purely statistical fluctuations – it is crucial *how* the particles are linked:

  Ideally, spots are clearly discernable and sufficiently separated in order to uniquely connect their positions through the image stack[15], i.e. to link (*track*) them and generate the respective trajectories.

  However, during the linking process errors can occur, basically in three different ways:

  1. On the one hand, although the particle is still present in frame $n+1$, the respective trace is terminated prematurely in frame n;
  2. On the other hand, although the particle is not present any more in frame $n+1$ (e.g., due to photobleaching or motion out of the image region), the respective trace is continued in frame $n+1$, but with a different particle[16].
  3. Finally, even if a particle is present in frame $n+1$, its trajectory is linked to some other particle in frame $n+1$ (which might be closer to the one in frame n, for example).

  All three errors introduce bias:

  - Error #1 leads to the interruption of real traces with the consequence that big steps are excluded from the MSD / displacement histogram; In this case the diffusion constant is shifted to smaller values. (This error can in principle be reduced by decreasing the lag time.)
  - Error #2 leads to artificially long traces (concerning the number of time steps of the trajectories and the way travelled by the particle). However, the potential bias towards larger diffusion constants – because erroneous big steps are included – can be prevented by employing a suitable tracking algorithm and a proper choice of a reasonable, system-specific maximal step distance (see chapter 8 and Appendix 13.4).
  - Error #3 can have ambiguous effect on the outcome of the analysis;
    If the linking occurs in the way that the particle in frame $n+1$ is chosen which is closest to the position of the "original" one in frame n,

[15] Assembling the single image frames along the third dimension generates an "image stack".
[16] In this case the trajectory should be terminated in frame n, and a new trace should start in frame $n+1$.

the diffusion constant is biased towards smaller values: The smallest displacements possible are selected.

Especially if the density of particles is high enough that their trajectories cross each other, an artificial shift of D to smaller values can easily happen because in this case it is very difficult to distinguish the particles from each other. (Empirical corrections for this artifact are treated in section 8.6.4 and Fig. 8.14.)

Reducing the particle density is the straight forward (experimental) remedy; If that proves difficult, it is wise to accept only trajectories containing links with an "empirically" high likelihood, i.e. relative proximity of the spots involved – and interrupting traces at dubious "joints".

This will lead to shorter traces than theoretically possible, and for longer lag times / displacements statistical precision of the MSD / DH analysis decreases.

- **Statistical fluctuations**

  Statistical fluctuations of the particle motion itself can cause changes in the shape among different trajectories which can be reflected, in MSD plots, for example. If the spread in shape within a set of trajectories is not considered, one easily assumes real heterogeneity where only statistical fluctuations exist.

  Therefore, as a general rule, it is very much required to base the conclusions gained from single particle tracking analysis on a solid statistical fundament [80].

- **Change in the mode of motion**

  Similar to the artifact introduced by erroneous linking, combining subtrajectories belonging to the same particle but to different modes of motion can lead to severe misinterpretation (for example, if a vesicle, previously bound to the cell membrane, gets suddenly dragged by a motor protein along a microtubule). One approach offered in [80] demands to not only analyze the trajectories themselves but also to consider the probability of their occurrence in order to determine whether real heterogeneity in a system is present or not.

Step distance histogram (DH) versus mean square displacement (MSD)

As Fig. 4.2 suggests, MSD and DH show empirically a different sensitivity for extracting the diffusion coefficient concerning the number of data points included for the fit.

To compute the diffusion constant from a step distance histogram, e.g. a Rayleigh distribution can be (nonlinearly) fitted to it. Only steps distant by one unit lag time Δt_{lag} have to be included. The more histogram data points included, the more stable the fitting.

On the contrary, to obtain D from the MSD, the MSD is fitted by a linear, possibly weighted, fit function. The specific value of the diffusion coefficient usually strongly depends on the data points MSD(t_{lag}) included in the fit. The longer the lag time, the rougher the MSD gets, so that statistical weighting is strongly recommended. As a number of thump, only ca. the first 25% of the MSD(t_{lag})-values should be included in the fitting [81]. Correct weighting, however, becomes more complicated if the data set consists of trajectories of different length.

Furthermore, several subpopulations can only be extracted from the DH but not from the MSD.

Therefore, in this thesis, diffusion constants were only determined by fitting a Rayleigh distribution to a step distance histogram.

Conclusions

As every experimental method, analyzing single particle trajectories requires a certain *qualitative* assessment of the results which (ideally) should be based on solid statistical arguments. Analyzing the image data[17] means reducing their complexity and compressing the information contained to gain results of low dimensionality (e.g. the scalar diffusion coefficient). This generally involves non-trivial image analysis procedures along a certain path in a multi-dimensional parameter space. This space can – usually – neither theoretically nor practically be explored extensively.

Therefore, (semi-)empirical decisions have to be taken concerning the specific analysis procedure; to reduce subjective bias to a minimum, however, the influence of the specific parameter on the final outcome should be carefully estimated and, hence, an appropriate value chosen.

The experimental work presented in this thesis was conducted and the image

[17] Image stacks can be represented as 3D intensity matrices, i.e. third order tensors which are usually quite complex data arrays.

analysis algorithm (presented below) was built guided by these principles.

4.3. Optimization of the signal-to-noise ratio (SNR)

After discussing the basic concepts of single molecule imaging and tracking (under special consideration of diffusion processes), the dependence of the signal-to-noise ratio (SNR) as the most important figure of merit on several experimental parameters shall be elucidated in the following. The SNR was defined in Eqns. 3.23–3.25, depending on the units in which the signal N and the noise σ are expressed. In the present section, SNR^e (Eqn. 3.24) shall be discussed ("photoelectron picture").

Since for image acquisition a CCD camera was used, the photons were converted into photoelectrons which were collected in a digital way, which means a two-fold integration (binning):

- On the one hand, due to the finite size of the CCD elements, all photoelectrons converted on the area of a given CCD element are counted in this element.
- On the other hand, due to the gain $g > 1$, packs of g photoelectrons are digitized as one count each.

As can be seen from Eqn. 3.24, three parameters determine SNR:

- the signal intensity $N^e_{fl,s}$; It is considered as the amplitude of the pixel with the maximum intensity within the image of a specific particle (spot).
- the background fluorescence intensity $N^e_{fl,b}$; For simplicity – and as experimentally justified – it shall be neglected in the current discussion.
- The (pixelated) read out noise σ^e_{ro};

The simplified Eqn. 3.24 yields:

$$\mathrm{SNR} \approx \frac{N^e_{fl,s}}{\sqrt{N^e_{fl,s} \cdot \mathrm{e} + \left(\sigma^e_{ro}\right)^2}}. \tag{4.31}$$

Starting with σ^e_{ro}, its value is fixed for a given set of CCD camera parameters (temperature, "CCD gain", read out speed, etc.)[18]. In particular, σ^e_{ro} is independent of the parameters that can be varied experimentally (and which affect $N^e_{fl,s}$):

- the magnification M

[18] See experimental section.

- the illumination (exposure) time Δt_{exp}
- the illumination intensity I_{exp}.

Because the localization precision depends strongly on the signal-to-noise ratio, it is advisable to optimize SNR for these parameters.

4.3.1. Magnification

In the microscope, the focal plane Σ in the object space is imaged onto the corresponding focal plane Σ' in image space[19] and vice-versa. Here, Σ' is defined by Σ, given by the plane of the CCD chip. The CCD elements with size Δx_{el} are, therefore, images of the pixels [20] with size Δx_{pix}:

$$\Delta x_{pix} = \frac{\Delta x_{el}}{M}. \tag{4.32}$$

The number of photons emitted by a molecule (and the number detected by all pixels) is independent from M, however, not so the width of the PSF in terms of Δx_{pix}. Therefore, with increasing M (and numerical aperture, NA $= n \sin\alpha$), the PSF spreads over a larger number of pixels.

Assuming a 2D-Gaussian shaped PSF, centered in the middle of a pixel, $N^e_{fl,s}$ can be determined as:

$$\begin{aligned} N^e_{fl,s} &= \int_{-\Delta x_{pix}/2}^{+\Delta x_{pix}/2} \int_{-\Delta x_{pix}/2}^{+\Delta x_{pix}/2} I(x,y)\, dx\, dy \\ &= 2\pi\, \tilde{\sigma}^2_{xy} I^e_S \left[\mathrm{erf}\left(\frac{\Delta x_{pix}}{\sqrt{8}\,\tilde{\sigma}_{xy}}\right)\right]^2 \\ &= N^e_{S,tot} \left[\mathrm{erf}\left(\frac{\Delta x_{pix}}{\sqrt{8}\,\tilde{\sigma}_{xy}}\right)\right]^2 \\ &= N^e_{S,tot} \left[\mathrm{erf}\left(\frac{\Delta x_{el}}{\sqrt{8}\,M\tilde{\sigma}_{xy}}\right)\right]^2 \end{aligned} \tag{4.33}$$

with $\tilde{\sigma}_{xy}$ as PSF standard deviation[21] ($[\tilde{\sigma}_{xy}] = m$), I^e_S as maximum emission intensity ($[I^e_S] = e/m^2$) and $N^e_{S,tot}$ as total number of photoelectrons [54].

erf(x) gives the error function:

[19] in real optical systems: Petzval surface Σ_p, due to field curvature aberration[39]

[20] *picture elements*

[21] The FWHM (*Full width at half maximum*) is generally given by FWHM $= \sqrt{8\ln 2}\tilde{\sigma}_{xy} \approx 2.35\,\tilde{\sigma}_{xy}$. It can be approximated by $\lambda/2$, therefore, for red light FWHM $\approx 0.30\,\mu$m and $\tilde{\sigma}_{xy} \approx 0.13\,\mu$m

$$\mathrm{erf}(x) \;=\; \frac{2}{\sqrt{\pi}} \int_0^x e^{-t^2}\, dt. \tag{4.34}$$

For a typical single molecule, the emission rate is $\approx 600\,\mathrm{count/s}$ so that for $\Delta t_{exp} = 10\,\mathrm{ms}$ $I_S^c = 6\,\mathrm{count/pixel}$. With gain $g = 6.4\,\mathrm{e/count}$[22] and $\tilde{\sigma}_{xy}^2 = 0.13\,\mu\mathrm{m}$,

$$\begin{aligned} N_{S,tot}^e &= 2\pi\, \left(\tilde{\sigma}_{xy}/\Delta x_{pix}\right)^2 g I_S^c \\ &= 2\pi\, \cdot \left(0.13\,\mu\mathrm{m}/\left(0.1075\,\mu\mathrm{m/pixel}\right)\right)^2 \cdot 6.4 \cdot 6\,\mathrm{e/pixel}^2 \\ &\approx 9.2 \cdot 6.4 \cdot 6\,\mathrm{e} \approx 350\,\mathrm{e}. \end{aligned} \tag{4.35}$$

Further follows:

$$\left[\mathrm{erf}\left(\frac{\Delta x_{pix}}{\sqrt{8}\,\tilde{\sigma}_{xy}}\right)\right]^2 \;\approx\; \left[\mathrm{erf}\left(0.292\right)\right]^2 \approx 0.106. \tag{4.36}$$

Therefore,

$$N_{fl,s}^e \;\approx\; 0.106 \cdot N_{S,tot}^e \approx 37\mathrm{e}. \tag{4.37}$$

That means, of the 350 photoelectrons converted in the CCD in total, in this case 37 e are registered in the central pixel. For a given read out noise[23] $\sigma_{ro}^e = 5.3\,\mathrm{e}$, one gets for the SNR in the central pixel (Eqn. 4.31):

$$\begin{aligned} \mathrm{SNR}_{center} &= \frac{N_{fl,s}^e}{\sqrt{N_{fl,s}^e \cdot \mathrm{e} + \left(\sigma_{ro}^e\right)^2}} \\ &\approx \frac{37\mathrm{e}}{\sqrt{37\mathrm{e} \cdot \mathrm{e} + \left(5.3\mathrm{e}\right)^2}} \;\approx\; 4.6. \end{aligned} \tag{4.38}$$

(To summarize, typical experimental values for single molecule fluorescence are given in Tab. 4.3.)
As is obvious from Eqn. 4.33, the magnification has a big influence on the SNR and the localization and intensity precision: To maximize SNR_{center}, it is desirable to select an objective with M as small as possible (see also [53]).

However, in the presence of CCD read out noise the localization precision is neither highest if the SNR of the *central* pixel is maximal (low M), nor if it is minimal (high M); This can be seen as follows:

[22] CoolSnap HQ, Roper Scientific; see experimental section;
[23] CoolSnap HQ, Roper Scientific; see experimental section;

$N^e_{S,tot}$	350 e
Δt_{exp}	10 ms
Δx_{el}	6.45 μm
M	60
Δx_{pix}	0.1075 μm
$\tilde{\sigma}_{xy}$	0.13 μm
σ^e_{ro}	5.3 e
g	6.4 count/e
$N^e_{S,fl}$	37 e
SNR	4.6

Table 4.3.: Typical parameters for single molecule experiments.

- high M: the PSF is spread over many pixels, the signal vanishes in the read out noise. The resulting SNR for every pixel is low.

- low M: the PSF is concentrated in one pixel, signal stretching from its "tails" into neighboring pixels vanishes in the read out noise; The determination of the spot position by fitting a 2D-Gaussian model function will be biased towards the pixel center.

Hence, a "medium" magnification has to be found in order to maximize the effective localization and intensity precision.

Additionally, to prevent an aliasing effect due to an insufficient spatial sampling rate, the Nyquist criterion has to be fulfilled: To sample an analog signal I in order to reconstruct it completely from the sampled (digitized) data I', the sampling rate $\tilde{k}$ has to be at least twice as high as the highest (spatial) frequency in the signal, $k_{sig,max}$:

$$k_{sig,max} \leq \tilde{k}/2 \tag{4.39}$$

$k_{sig,max}$ is given by the inverse resolution $r \approx \lambda/2$, therefore:

$$k_{sig,max} \approx 2/\lambda \leq \tilde{k}/2 \tag{4.40}$$

Therefore,

$$\tilde{k} \geq 4/\lambda \tag{4.41}$$

The sampling rate is given by the inverse pixel length, $\Delta x_{pix} = \Delta x_{el}/M$. For typical objectives available with a magnification of $40(60, 100)\times$, this means:

$$\begin{aligned} \tilde{k}_{40} &= 161\,\text{nm} \\ \tilde{k}_{60} &= 107.5\,\text{nm} \\ \tilde{k}_{100} &= 64.5\,\text{nm} \end{aligned} \tag{4.42}$$

Emission wavelengths are typically in the range of $\lambda = 500 \ldots 650\,\text{nm}$, $k_{sig,max} = 125 \ldots 163\,\text{nm}$. Thus, only the $60\times$- and $100\times$-objectives can be used in order to prevent aliasing.

Finally, a $60\times$ water immersion objective with a very high numerical aperture ($60\times$ /NA1.2 UPlanApo, Olympus Corporation) was preferred to a $100\times$ one, in order to avoid spreading of the PSF and loss of signal intensity.

Oil immersion objectives proved not superior to water immersion optics because the objects of interest were localized in a significant distance from the glass-water-interface. Hence, the higher NA of the oil objective (NA = 1.4) compared to the respective water immersion objectives (NA = 1.2) was ineffective. Additionally, the immersion oil showed a certain autofluorescence if excited with blue-green light.

4.3.2. Illumination time / intensity

The broadening of the spot size due to diffusion during a finite exposure time Δt_{exp} was first described in [86, 102] without further analysis. This is provided on basis of numerical simulations in e.g. [90] and [52]. However, due to the characteristic properties of the specific fitting algorithm used and the biological system under investigation, it seemed appropriate to determine the dependence of the localization precision by detailed simulations (see chapter #8).

In brief, Δt_{exp} should not be

- **too small**, since in this case the signal collected is too weak to detect the spots with a reasonable certainty and to determine the spot position and height;
- **too big**, because this leads to short time-trajectories due to early photobleaching. Furthermore, in case of moving molecules / particles, the longer the acquisition time, the more the spots deviate from a 2D-Gaussian model;

Similar as to the illumination time, there is a finite value for the illumination intensity I_{exc} at which the SNR becomes a maximum:

If I_{exc} is

- **too small**, the signal acquired is too weak to allow for a reliably certain identification of the spots and their consistent fitting;

- **too big**, the molecules bleach fast and do not show sufficiently long trajectories; additionally, the emission intensity I_{em} increases *non-linearly* with I_{exc} and saturates, so that increasing I_{exc} above the saturation intensity I_{sat} leads to an ever higher population of the triplet state and, therefore, increased photobleaching (see section 2.0.2).

As discussed in section 5.2, typically excitation times in the range of a few to tens of ms were chosen, as well as excitation intensities varying from tenth to several kW/cm^2.

Part II.

Experimental methods

5. Wide field microscopy

As already introduced in section 3.1, a wide field microscopy setup was employed for the single molecule tracking experiments performed in this thesis. Of course, other (optical and non-optical) measurements were performed, however, as the focus of this work is fluorescence imaging of single molecules, the other techniques are briefly described below and the reader is referred to more detailed publications.

5.1. Components

Principal components of the optical setup, which will be explained in more detail below, are:

- **Microscope and objectives**
- **Laser sources**
- **Acousto-Optical Modulator**
- **CCD-camera**
- **Optical filters, lenses and mirrors**

5.1.1. Microscope and objectives

A commercial inverted optical microscope (IX 50, Olympus) was utilized, equipped with either an oil or water immersion objective with a high numerical aperture (60× /1.4 UPlanApo oil immersion; 60× /1.2 UPlanApo water immersion, Olympus) similar as has been used by [56].

5.1.2. Laser sources

For illumination of the sample only lasers were employed. Compared to conventional light sources (mercury / tungsten / Xe lamp etc.), laser light is different in several – usually beneficial –ways:

- It consists of one or more, usually well separated spectral lines. Therefore, it provides well-defined excitation conditions.
- It provides a high degree of coherence which allows for good focusing (and collimation) and, thus, high excitation intensity.

- Owing to the small beam width, acousto-optical modulators (AOM) can be used to modulate the intensity with a rise time of a few hundred ns[1].

ArKr Ion gas laser

For most of the experiments, an ArKr Ion laser (Innova70, Coherent Corp.) served as the source for several wavelengths used, especially 488/514/520 nm. Especially the spread of the lines from ca. 450 to 647 nm opens up opportunities for 2-color-excitation which were only partly exploited during this thesis[2]. Besides the broad spectrum, the Innova70 offers high emission intensities of up to 10 W in total. (Whereas for some spectroscopic applications, like fluorescence correlation spectroscopy, power values in the mW or μW-regime are sufficient, for single molecule imaging experiments the output power exceeding 1 W is required, especially for "short" illumination times of 10 ms and below.)

Diode laser, 405 nm

To excite particular fluorescent proteins at short wavelengths, a blue laser diode (Laser 2000, Wessling, Germany) emitting at 405 nm ($P = 30$ mW) was utilized.

The principle and technology of the laser devices used is beyond the scope of this work but can be found treated extensively in [27].

5.1.3. Acousto-optical modulator

A commercially available acousto-optical modulator (AOM) (AA.MOD.4C, A.A Sa Co., St-Rémy-Lès-Chevreuse, France) was utilized to

- select specific laser lines (from the ArKr-laser in multi-line mode) and to

- modulate the excitation intensity.

With the driver used, up to four lines could be modulated independently and simultaneously, which allowed for multi-color excitation experiments.

Although the AOM blocked most of the light when switched off, up to 0.05% was transmitted even in maximal blocking. This made it necessary to use additional laser clean-up filters and (mechanical) shutters, in order to avoid laser light bleed-through and photobleaching of the fluorophores.

[1] Shutters usually can not open/close faster than several ms.
[2] With different sets of optical filters also UV-emission is accessible.

5.1.4. CCD-camera

For image acquisition, a commercial ultra-sensitive low-noise high speed CCD[3] camera was used (CoolSnap HQ, Roper Scientific), controlled by a commercial software (WinSpec32, Roper Scientific). It is calibrated and described in more detail in section 5.3.1.

5.1.5. Optical filters, lenses and mirrors

Optical filters

Optical filters were used for

1. "cleaning" the excitation light by removing residual light of unwanted wavelengths ("clean-up filters");
2. aligning two excitation light beams (dichroic mirrors, DM);
3. separating emission from excitation light or splitting emission light of different wavelength (dichroic mirrors, DM);
4. removing residual excitation from emission radiation *after* the dichroic mirror (band-pass (BP)/ long-pass (LP) filters);

For the two most intensively investigate dyes in this thesis, Figs. 5.1 and 5.2 display the transmission spectra of the optical filters used together with the emission spectra of DiI and *Kaede*-GFP (green/red form).

The filters had to be chosen empirically based on the following criteria:

- **Clean-up filters**:
  - if multi-line lasers (ArKr) were used, light from lines with $\lambda > \lambda_{exc}$ could pass (and interfere at) the dichroic. Although very weak in power ($< 0.1\%$), it severely disturbs the real signal and has to be removed.
- **Dichroic mirrors**:
  - DM must reflect the excitation light and allow most of the emission radiation to pass. Therefore, step "edges" are desirable.

[3]Charge-Coupled Device

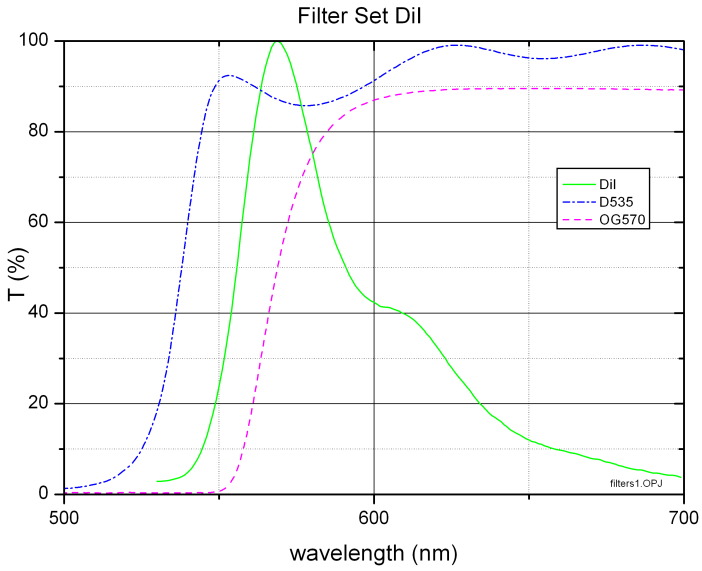

Figure 5.1.: Transmission spectra for the optical filters used for fluorescence imaging of single DiI molecules in lipid bilayer membranes: *blue dash-dotted*: dichroic mirror D535, *magenta dashed*: long-pass filter OG570. *green solid*: emission spectrum of DiI (Invitrogen Corp.)

- **Band-pass / long-pass filters**:

  - BP and LP filters should display a maximum transmission along the emission spectrum of the chosen fluorophore while blocking the excitation light with a factor of OD6 and higher ($< 10^{-4}\%$). (Due to the latter issue, the rising edge of D535/50 and OG570 are shifted up to 25 nm to the red compared to the respective dichroic mirrors.)

All filters were purchase by AHF Corp. (Tübingen, Germany).

It has to be emphasized that the optimal choice of the DC/BP or DC/LP combination is crucial for a high emission photon yield: Given that sufficiently powerful laser sources are available, bringing as many emitted photons (and as little excitation / stray light photons) as possible to the detector is of paramount interest.

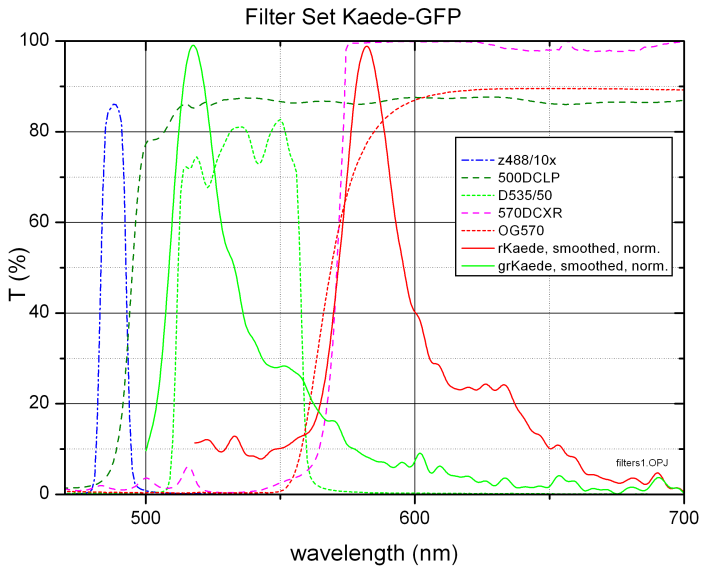

Figure 5.2.: Transmission spectra for the optical filters used for fluorescence imaging of single *Kaede*-GFP molecules immobilized in PAA-gel: *blue dash-dotted*: optical clean-up filter z488/10X, *olive dashed*: dichroic mirror 500DCLP, *green dotted*: band-pass filter D535/50, *magenta dashed*: dichroic mirror 570DCXR, *red dotted*: long-pass filter OG570. *green solid*: emission spectrum of *Kaede*-GFP (green form), *red solid*: emission spectrum of *Kaede*-GFP (red form).

Lenses and mirrors

Lenses and mirrors (Ag or Al coated) were used in particular for manipulation of the excitation light beam which has to be focused on the back focal plane of the objective used to illuminate the specimen homogeneously (see section 5.2).

A $\lambda/4$-plate was employed to convert linearly into circularly polarized laser light to safeguard for oriented static absorption dipoles.

Lenses and mirrors were purchases from Linos GmbH (Göttingen, Germany) or from Thorlabs GmbH (Karlsfeld, Germany).

5.2. Excitation system

The optical excitation pathway was determined by

- the laser light source(s)
- the acousto-optical modulator
- the intermediate optics (lenses, mirrors).

As the first items were already described above, the role of the intermediate lenses and mirrors shall be discussed here. Goal of the aligning procedure was to focus the laser beam on the back focal plane (BFP)[4] of the objective used in order to achieve a broadly and in general homogeneously illuminated field of view. Optical key parameters were

1. the axial position of the focal spot of the incident beam relatively to the BFP
2. the lateral position of the focal spot of the incident beam relatively to the BFP
3. the angle between the axis of the incident beam and the optical axis (of the objective)
4. the angle under which the laser beam is focussed on the BFP. This is determined by three factors:
   - the focal length of the last lens before the objective (*Convex lens*, Fig. 5.8
   - the beam expansion ratio f_2/f_1 (with f_1, f_2 as the focal lengths of the lenses of the beam expander)
   - the degree of collimation when the beam enters the *Convex lens*

Items (1) and (4) influence the degree of collimation of the beam entering the object (and, hence, the beam width in the focal plane), item (2) affects the position, and item (3) the direction of the beam penetrating the object.

In practise, it was not necessary to illuminate the object with a constant intensity *along the optical axis* because the relevant focal plane (in object space Σ) is determined by the position of the CCD camera chip (fixing the corresponding optical plane in image space Σ'). Therefore, slightly deviating the focus from the BFP (and, thereby, focussing into the specimen) was tolerable in order to tune the excitation intensity I_{exc} in a simple way. This was usually done by moving lens 2 (part of the beam expander) along the optical axis.

[4]Ideally, every (spherical) light wave emanating from the BFP is collimated by the objective and leaves it as a plane wave.

5.3. Detection system

5.3.1. CCD-camera

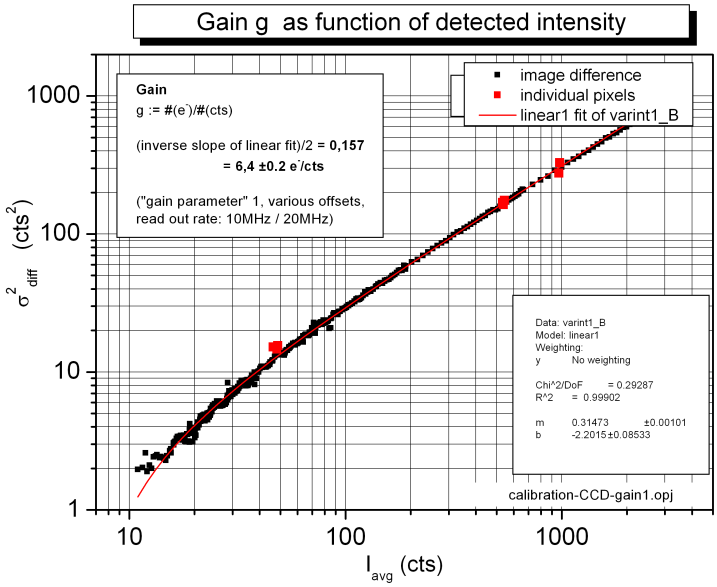

Figure 5.3.: Determination of gain $g = \#\text{e}/\text{count}$: Two images I_1, I_2, consecutively taken under the same conditions, were subtracted, yielding difference image I^c_{dif}; its intensity variance, $(\sigma^c_{N_{fl,S}})^2$, is plotted vs. I^c_{dif} following $(\sigma^c_{N_{fl,S}})^2 = 2/g \cdot I^c_{dif}$ (*black squares*). Linear fit of first 100 data points yields gain g (*red line*). ("2" results from the subtraction process due to error propagation). Variance of individual pixels computed from sequence of images coincide with results (*red squares*).

For capturing the images, a commercial ultra-sensitive low-noise high speed CCD[5] camera was used (CoolSnap HQ, Roper Scientific), controlled by a commercial software (WinSpec32, Roper Scientific).

This area detector had to be calibrated for two reasons:

- First, contrary to single-photon counting devices (e.g., APD, PMT), CCDs exhibit a considerable noise superimposed with the signal (see section 3.2).

[5]Charge-Coupled Device

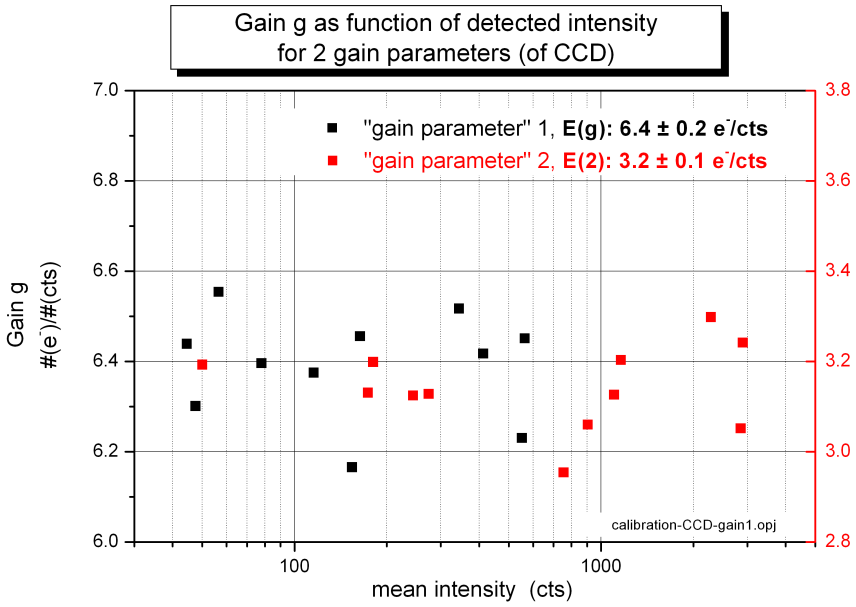

Figure 5.4.: Determination of gain g = #e/count according to Fig.5.3. g is plotted as function of I^c_{dif} for two different CCD "gain parameters" 1 and 2. Here, gain was determined by fitting data obtained under different illumination intensities separately.

The characteristic of this noise is a key to the determination of two CCD key parameters, the gain g (# electrons needed to generate one count) and the read out noise σ_{ro}.

Knowing the gain allows the determination of the number of photons captured, provided the quantum efficiency of the CCD is known.

The read out noise helps to set a lower threshold for the number of photons which have to be absorbed in order to gain meaningful information from the measurements.

- Second, based on knowing g and σ_{ro}, artificial images (matching the real ones) can be simulated and subsequently analyzed by the respective analysis algorithm in order to determine the quality of information obtained[6].

[6] e.g., the precision of the localization or the diffusion constant

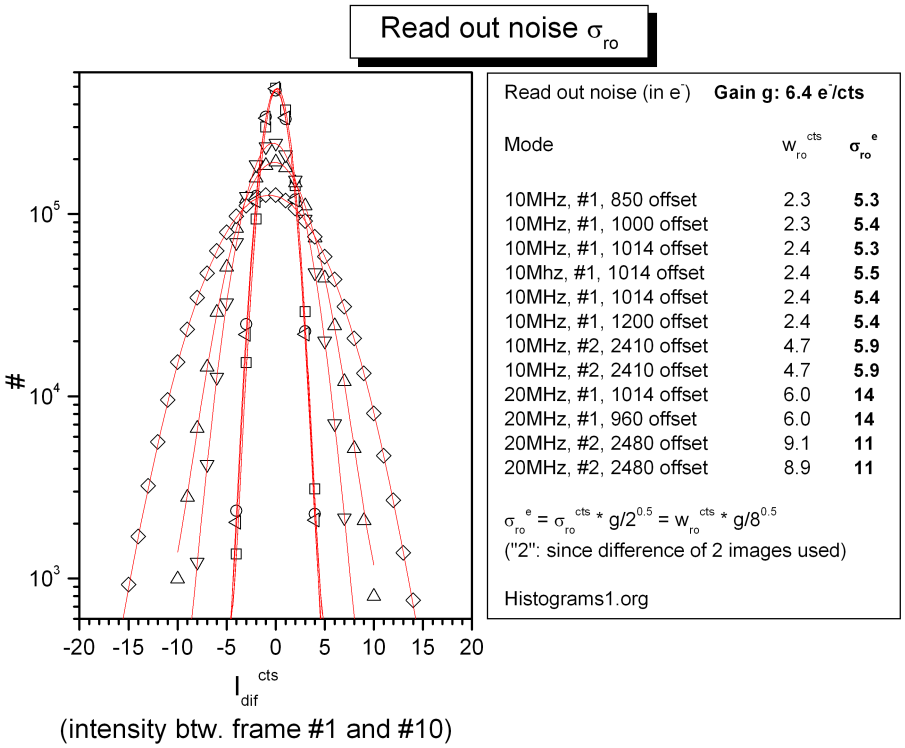

Figure 5.5.: Read out noise σ^e_{ro} determined for several CCD parameters (read out rate (10 / 20 Mhz), "gain parameter" (#1 / #2), intensity offset (various values)). Ten image frames were captured under zero illumination, then difference image I^c_{dif} between image #1 and #10 was computed; the histogram of I^c_{dif} was fitted to 1D-Gauss. 10 Mhz @ "gain parameter" #1 gives lowest σ^e_{ro}.

This "feed back" can be used to an enhance experimental parameters and the analysis algorithm, for example.

In Fig. 5.3 the gain is determined for the CCD by plotting the variance of the pixel intensity as function of the mean intensity. Two frames, consecutively taken under the same conditions, were subtracted, yielding the difference image I^c_{dif}; The image showed a broad dynamical range to achieve a wide distribution of mean intensities. Subsequently, the pixels were grouped according to their intensity into bins of the same width. For a given subgroup of pixels, the intensity variance was approximated as mean of the squared difference intensities from I^c_{dif}.

In Fig. 5.4, gain g is displayed for each intensity range separately, for two different parameter settings ("gain parameter 1 / 2"). As can be seen, "gain parameter 2" appears beneficial due to a lower gain (which means, less photoelectrons are needed to generate one count), however, this benefit is compensated by a much

higher σ_{ro}-value, as can be seen in Fig. 5.5.

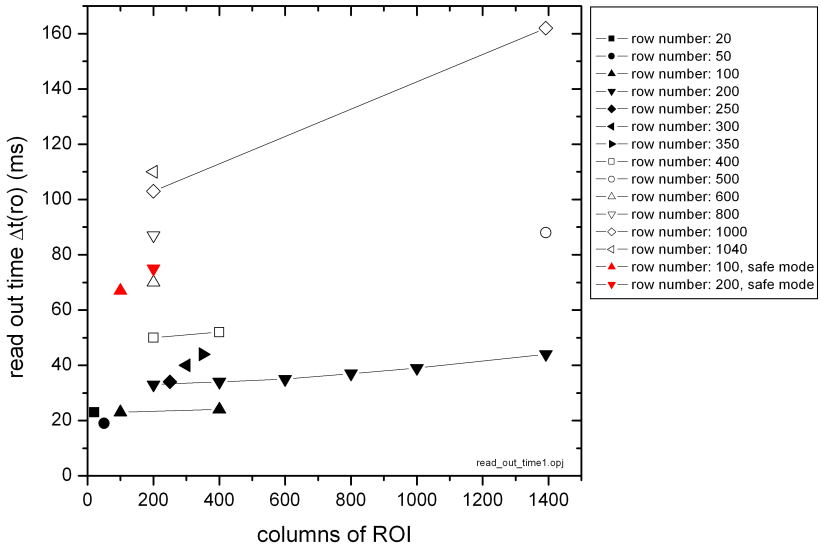

Figure 5.6.: Read out time Δt_{ro} as function of #(lines) of ROI selected, (CCD: CoolSnap HQ, Roper Scientific); ("fast mode" acquisition setting, if not declared otherwise).

Fig. 5.6 gives the dependence of the read out time Δt_{ro} as function of the number of (vertical) columns for the ROI (region of interest) chosen. As is clearly obvious, the number of the (horizontal) lines largely determines the read out speed.

Since the "fast mode" was more than a factor of 2 faster (and showed no increase of read out noise compared to, e.g., the "safe mode"), it was always chosen, if the CCD was not triggered externally.

In Tab. 5.1 the relevant CCD data for the operation mode used are listed. $I_{off,1}$ and $I_{off,2}$ are the CCD "dark" background offset levels; $I_{off,1}$ was set initially, $I_{off,2}$ was determined from darkfield images.

5.3.2. Resolution

In order to determine the resolution of the optical setup, images of immobilized single molecules were acquired (using a UPlanApo 60× 1.2W objective, Olympus)

parameter	value	remarks
g	6.4 e/count	"gain parameter 1"
σ_{ro}	5.3 e	(rms)
$I_{off,1}$	850 count	CCD-offset, set initially
$I_{off,2}$	11.2 count	CCD-offset, residual
columns	1392	
rows	1040	

Table 5.1.: CCD parameters

and analyzed by the automatic image processing algorithm. The spots were fitted by a 2D Gauss model with the spot standard deviation σ_{spot} as one of the fit parameters. The results are displayed as histogram in Fig. 5.7. Assuming the $FWHM = 2\sqrt{2\ln 2}\,\sigma_{spot}$ of a spot as the Abbe-, and $2\,\sigma_{spot}$ as the Sparrow-resolution, we get 282 ± 61 nm (Abbe) and 240 ± 52 nm (Sparrow).

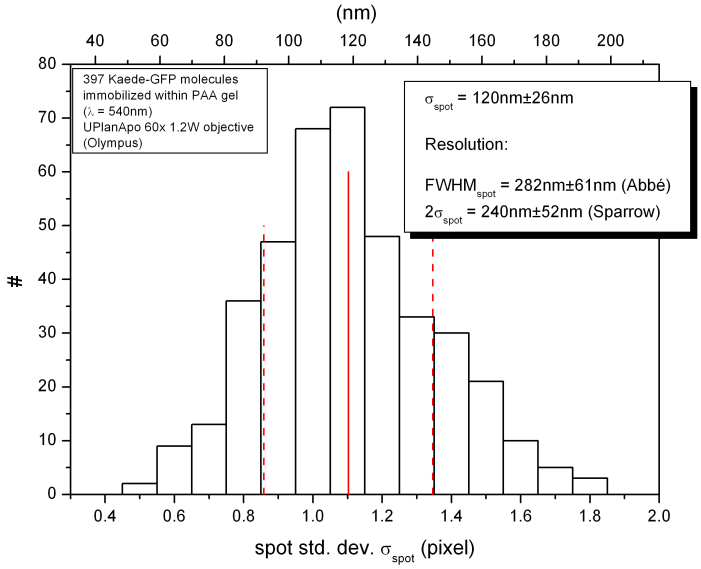

Figure 5.7.: Histogram of the spot std.dev. $\sigma_{spot} = 120 \pm 26$ nm (source: fit of 397 *Kaede*-GFP-molecules, immobilized in PAA-gel, $\lambda = 540$ nm). The Abbe-(Sparrow-) resolution is 282 ± 61 nm (240 ± 52 nm).

5.3.3. 2-color beam splitter

In order to investigate the fluorescence of *Kaede*-GFP-molecules, for example, the emission was separated into two spectral channels employing a 2-color beam splitter. This device was developed by Rainer Pick, Department of NanoBiophotonics, and the workshop for precision mechanics, Max-Planck-Institute for Biophysical Chemistry, Göttingen).

5.3.4. Detection efficiency

The detection efficiency η_{tot} of the optical setup is defined as

$$\eta_{tot} = \frac{\#\,(\text{photoelectrons generated})}{\#\,(\text{photons emitted})}. \tag{5.1}$$

η_{tot} can be computed as the product of the collection efficiency of the objective, η_{obj}, the transmissivities of the optical elements in the emission beam path (cover slip, $\tilde{T}_{CS}$, objective $\tilde{T}_{obj}$, tube lens $\tilde{T}_{tl}$, spectral filters $\tilde{T}_{filt}$, additional optical elements (microscope / cameral windows), $\tilde{T}_{add}$) and the detection efficiency of the CCD, η_{CCD}:

$$\eta_{tot} = \eta_{obj} \times \tilde{T}_{CS} \times \tilde{T}_{obj} \times \tilde{T}_{tl} \times \tilde{T}_{filt} \times \tilde{T}_{add} \times \eta_{CCD}. \tag{5.2}$$

η_{obj} can be computed from the numerical aperture NA $= n \sin\alpha$ of the objective:

$$\eta_{obj} = \frac{\Omega_{obj}}{4\pi} \quad \text{with} \quad \Omega_{\text{obj}} = \int_0^{\alpha} \sin\theta \,\mathrm{d}\theta \int_0^{2\pi} \mathrm{d}\phi = 2\pi\left[1 - \cos\alpha\right]. \tag{5.3}$$

With NA $= 1.2$ and $n = 1.33$ (water), $\alpha = 64°$ and $\eta_{obj} = 28\%$.
The numerical values[7] are given in Tab. 5.3.4.

Therefore, the overall detection efficiency η_{tot} is given by $0.09 \pm 0.02\,\mathrm{e/ph}$; if 100 photons are emitted by a fluorophore in the focal plane of the objective, on average 9 photoelectrons are created in the CCD chip.

5.4. Setup

After presenting the components of the optical setup, its specific outline shall be discussed in the following (see overview given by Fig. 5.8). The design was oriented on the main requirements for fluorescence excitation and detection.

[7] Values labelled with $\star$ are estimations; $\tilde{T}_{obj}$: Olympus; η_{CCD}: Roper Scientific.

parameter	value
η_{obj}	0.28 ± 0.02
$\tilde{T}_{CS}$	0.96 ± 0.02 $(\star)$
$\tilde{T}_{obj}$	0.90 ± 0.02
$\tilde{T}_{tl}$	0.95 ± 0.02 $(\star)$
$\tilde{T}_{filt}$	0.70 ± 0.10 $(\star)$
$\tilde{T}_{add}$	0.90 ± 0.10 $(\star)$
η_{CCD}	$0.60 \pm 0.05\,\mathrm{e/ph}$
η_{tot}	$0.09 \pm 0.02\,\mathrm{e/ph}$

Table 5.2.: Parameters contributing to the total detection efficiency η_{tot}

5.4.1. Fluorescence excitation

Optimal sample excitation exists if the illumination is spatially homogeneous, spectrally well-defined (i.e. usually monochromatic) and with specific constant intensity I_{exc} during the pulse length Δt_{exc} (and $I_{exc} = 0$ in between pulses, i.e. during CCD read out).

Illumination homogeneity To enhance the homogeneity of the illumination profile, the beam is expanded by the *Beam Expander* lenses and focused by the *Convex* lens (see Fig. 5.8) on the BFP of the objective. The wider the beam is expanded, the more homogeneous the beam profile becomes, at the expense of I_{exc}, however. To get $I_{exc} = 1$ kW/cm^2 for an sample area of, e.g., $10 \times 10\,\mu$m, at least $P_{exc} = 100$ mW have to be coupled into the objective; this P_{exc} value is usually beyond the specifications of the objective for continuous exposure, so here it was applied only for pulsed excitation[8].

Additionally, to reduce unwanted interference patterns (*speckles*) it proved necessary to thoroughly clean lens and mirror surfaces in the beam path to remove disturbing dust[9].

[8] Also excitation powers of up to 200 mW ($\lambda = 647$ nm) could be used without damaging the objective.

[9] Speckles can, in principle, be removed by focussing the excitation beam on a rotating ground-glass diffuser disk with subsequent collimation of the transmitted, scattered light. This approach was tested during the initial phase of setup building, in close collaboration with the workshop for precision mechanics, MPI for Biophysical Chemistry, Göttingen. However, two obstacles prevented a broader application of this idea. First, it proved very difficult to rotate the disk fast enough for sufficient speckle averaging during the image acquisition time of few ms. Second, it would have required expensive mechanical equipment (bearing etc.), to increase the disk speed and reduce the beam undulations induced by insufficient (non-axial) mounting. Therefore, beam expansion as displayed in Fig. 5.8 and a mostly speckle-free illumination

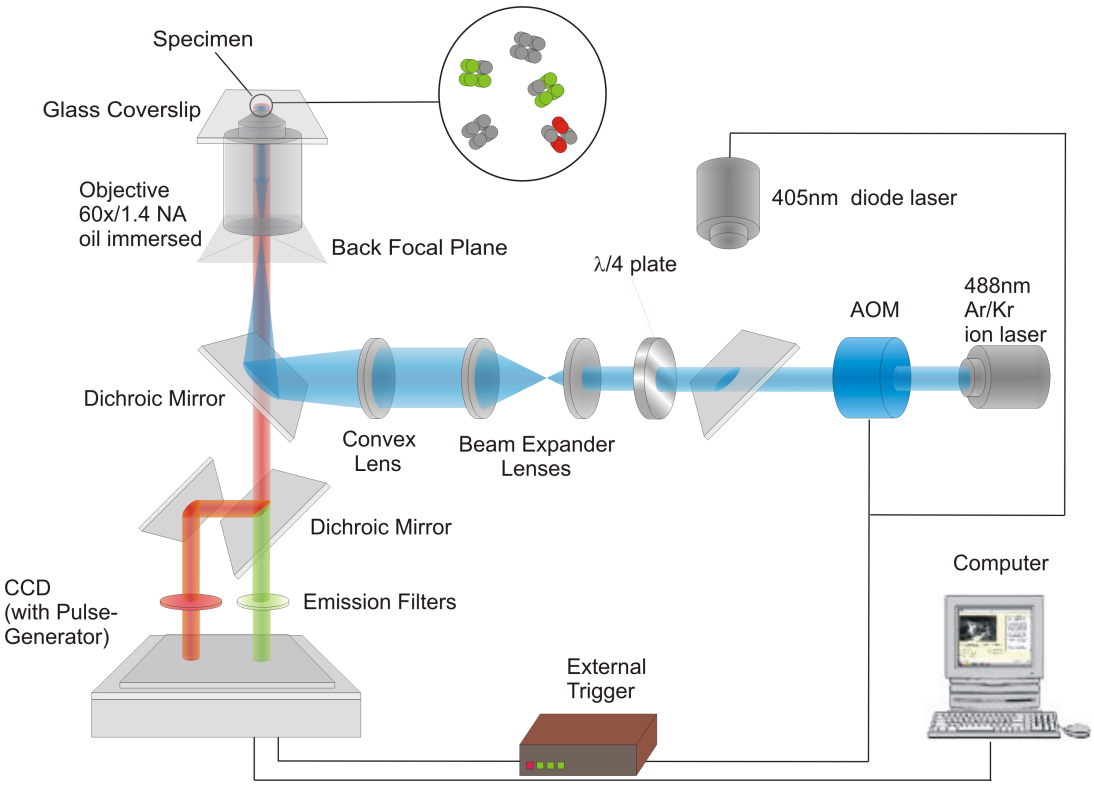

Figure 5.8.: Experimental 2-color-excitation / 2-color-detection setup as used for photophysical investigations of the *Kaede*-GFP. The sample is excited by radiation of two colors from two different laser sources, the emission signal is split by a beam splitter and focussed on a CCD camera.

Spectral properties In order to efficiently excite specific fluorophores, the sample is illuminated with light of usually one or two wavelengths $\lambda_{exc,i}$ which were selected out of the multi-line beam of the ArKr-Laser by the AOM. To remove residual laser emission[10], additional spectral clean-up filters were inserted into the beam path.

Pulse length The AOM not only selects $\lambda_{exc,i}$ but has also the function of a shutter "opening" for the excitation time Δt_{exc}. Either triggered by the CCD or an external TTL-pulse generator, Δt_{exc} can be as short as fractions of 1 ms (limited by the CCD).

field conformed to the experimental needs.

[10]The AOM exhibits for a particular laser line up to 0.05% bleed-through, compared to the total line emission.

5.4.2. Fluorescence detection

Optimal detection conditions prevail if a maximum of photons from the specific fluorophores and a minimum of photons from other sources (e.g., excitation or stray light) are detected. Thus, on the one hand, the factors in Tab. 5.3.4 should all be one for the fluorescence photons, on the other hand, $\tilde{T}_{filt}$ should be zero for other photons.

Among the factors contributing to the collection efficiency η_{tot}, the most promising and important to optimize for a wide field setup are the CCD (η_{CCD}), the spectral filters ($\tilde{T}_{filt}$) and the objective (η_{obj},$\tilde{T}_{obj}$). However, taking only η_{tot} does not suffice to judge the overall detection performance.

CCD The CCD camera employed (CoolSnap HQ) is run with the parameters described in 5.3.1 which were found by careful optimization[11]. Although the (device specific) parameter η_{CCD} is crucial for the conversion of photons into electrons, its value has to be comprehended by the CCD gain g and the read out noise σ_{ro}. Both parameters dramatically influence the overall performance of the imaging technique.

Therefore, optimization potential for the present setup results in the CCDs developed in recent years which exhibit a very small σ_{ro}.

Spectral filters The spectral filters were empirically selected to provide a maximal $\tilde{T}_{filt}$ for the range of the fluorescence emission while at the same time blocking λ_{exc} by a factor of 10^6.

Objective If the object is separated from the coverslip surface by an aqueous environment of more than a few hundred nm[12], objectives using an immersion medium with $n_{im} > 1.33$ do not necessarily improve η_{obj} since η_{obj} is effectively determined by the limiting angle α under which the entrance pupil of the objective is "seen" by the molecule and *not* by the numerical aperture alone. (Furthermore, the immersion oil showed some undesirable autofluorescence if excited with blue or green light.)

Thus, in case of imaging fluorophores diffusing within lipid membranes, a water immersion objective with the highest available NA of 1.2 and $\tilde{T}_{obj} = 0.90$ was used.

However, for detecting the fluorescence of *Kaede*-GFP molecules immobilized close to the coverslip surface, an oil objective (NA = 1.4, $\tilde{T}_{obj} = 0.90$) was employed.

[11] with the very helpful advice of Dr. N. Gulde, Roper Scientific
[12] for example, as is the case for lipid membranes of GUVs

Fluorescence spectrometer For acquisition of fluorescence spectra a spectrometer (S2000, Ocean Optics) glass fiber-coupled was used.

5.4.3. Miscellaneous

Fluorescent dyes Besides the purely setup related factors, the specific photophysical properties of the fluorescent dyes, especially the quantum efficiency Φ_F and the photobleaching time τ_{PB}, contribute strongly to the obtainable image quality.

Autofluorescence Another issue for intracellular single molecule fluorescence studies is the presence of autofluorescence if the sample is excited by blue to green light. So there is, e.g., an ongoing quest for fluorescent proteins emitting in the (far) red part of the spectrum. Contrary to intra-cellular autofluorescence, these proteins can be excited by orange-red light.

Interdependence Additionally, Many experimental parameters are coupled to each other. For example,

- τ_{PB} depends on the excitation intensity and the chemical environment.
- A big $\tilde{T}_{filt}$ in the range of the fluorescence emission might lead to increased cross talk of λ_{exc}.
- Excitation in the red might lead to low autofluorescence but the dyes absorbing red light might exhibit low Φ_F and / or τ_{PB}.

Therefore, the experimental system as a whole - the optical setup (excitation and detection) and the sample - must be optimized in order to gain optimal results in form of sequences of spot images with a high SNR. These images are then the input for the essential (and quite sophisticated) data analysis.

6. Multi-spot imaging & tracking

For an efficient image analysis and to introduce only a minimum of bias, an automatic multi-spot imaging analysis software had to be developed. Although commercial software and freeware[1] is available, the particular image features, especially the presence of many spots (up to several hundreds in a single image frame) and a generally very low signal to noise ratio ($\sim$ 3-6) required the utilization of a versatile automated image analysis procedure.

Topic of the following chapter is the description of the work flow of this image analysis software, implemented in MATLAB (The Mathworks, MA, U.S.A.), and a thorough quantitative characterization concerning localization precision Δx_{loc} and determination of the diffusion constant D.

6.1. Design of image analysis algorithm

Like the majority of feature tracking software [78], the algorithm presented here can be divided into two core parts: First, the feature extraction (segmentation and fitting) and second, the tracking of the spots through the image stack (linking of trajectories). After having the traces obtained and computing step distance histograms, the data are further processed using commercial data analysis software (ORIGIN7.0, Originlab, MA, U.S.A.) for further evaluation.

More detailed, the workflow of the image analysis algorithm can be described as follows (Tab. 6.1):

Module #0 : First, the image sequence has to be loaded in ("in_file").

Module #1 : Then, the part of the full frame (region of interest, ROI), containing the features of interest (in x-, y-, and z-coordinates) has to be selected ("in_file_ROI").

In case of two spectral channels two ROIs exist on the CCD chip with a specific shift vector $\mathbf{r_s} = (x_s, y_s)$ in between used to cutting out the two ROIs[2].

[1] An example for commercial software is METAMORPH (Molecular Devices Corp.), examples for freeware are SPOT-TRACKER (JAVA-applet for ImageJ software [78]), VIEW5D (JAVA-applet [41]) and a feature point tracking software [83].

[2] $\mathbf{r}_s$ has to be determined independently by, for example, immobilized beads emitting in both channels simultaneously.

module #	content	resulting file
0	loading of image sequence	"in_file"
1	selecting ROI (1-/2-channel case)	"in_file_ROI"
2	subtraction of background offset	"in_file_ROI_bg"
3	filtering by convolution with 2D-Gauss	"in_file_ROI_bg_filter"
4	segmentation of features (spots)	"spot_list_test"
5	feature extraction	"spot_fit_list"
6	feature checking	
7	image reconstruction	"Fit"
8	linking of trajectories	"peaks"
9	trace analysis (step distance histogram)	"step_hist"

Table 6.1.: Workflow of image analysis algorithm

Module #2 : Subsequently, the performance of the feature extraction step ("fitting", module #5) is enhanced by determining and subtracting a constant background offset $I_{off,2}$ for each frame, yielding "in_file_ROI_bg"[3].

The background offset is computed by a weighted fit of the intensity values of all pixels (employing the "robustfit" function in MATLAB and permuting the order of the pixels to avoid trends). Homogeneous within each frame, this background is attributable to the sum of a constant CCD offset $I_{off,2} = 11.2$ count and (potential) residual fluorescence (small, ca. 1-2 count, from out-of-focus emission, etc.) which bleaches on a frame-to-frame basis.

While [83] starts with normalizing the intensity of the images, this is not done here for two reasons: First, the photon shot noise which is included into the spot fitting routine (see below) depends on the absolute pixel intensity value. And second, the spot intensity information is of considerable interest for certain applications [84].

Although the localization precision Δx_{loc} of a spot fitting algorithm is usually of great interest, for the sample system under investigation here (with its relatively large diffusion constant D), simulations showed that even a moderate Δx_{loc} of several ten nanometers only contributes in a minor way to the overall precision of D determination. Therefore, in the case of the experimental system investigated here, optimization of the localization precision beyond a certain limit (ca. 50 nm) was not critical.

Module #3 : In the next image enhancement ("filtering") module, "in_file_ROI_bg_filter" is obtained by convolution of each frame with a 2D Gaus-

[3] see Tab. 5.1

sian kernel [86], with a spot standard deviation (std.dev.) of $\sigma_{spot}^{filt} = 1.0\,\text{pixel}$.

This value was adapted to the std.dev. of real immobilized spots σ_{spot}, reflecting the cross section through the point spread function of the optical setup (see Fig. 5.7). (σ_{spot} is part of the features extracted in the "fitting"-module.)

Since the fluorescent image of a particle on the CCD chip is binned by the discrete pixel array of the CCD chip, the image intensity is in theory non-zero for *all* pixels (due to the non-vanishing PSF). However, considering typical peak intensity and background amplitude values, the spot intensity is negligibly small outside a ROI of $5 \times 5\,\text{pixel}$. Therefore, the standard kernel size[4] used in the algorithm was $5 \times 5\,\text{pixel}$.

Excursus: Filtering Sage et al. [78] proposes the use of a LoG-filter (also known as "Mexican hat") to remove noise which intensity is distributed according to a power law. Convolving our raw images with different kernels (LoG of different std.dev. $\sigma_{LoG}^{filt} = 1.5\,/\,2.0\,/\,2.5\,\text{pixel}$ and a 2D Gaussian, $\sigma_{2DG}^{filt} = 1.0\,\text{pixel}$), however, gives no visible advantage of the LoG approach for our images (Fig. 6.1).

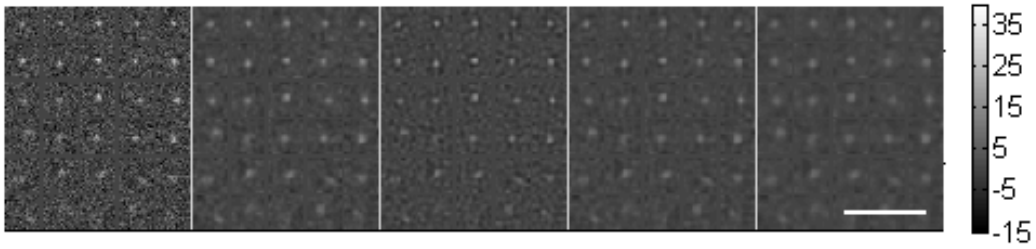

Figure 6.1.: Comparison of convolution filter kernels; *mid-left* to *right*: convolution of original images (*far left*) with different kernels: Gaussian (1.0), LoC (1.5), LoC (2.0), LoC (2.5); (in brackets: σ_{spot} (pixel)). Original images consist of different simulated images of diffusing spots with realistic background noise; *vertical*: diffusion constant $D = 0$; 0.1; 1.0; 2.5; 5.0; $10.0\,\mu\text{m}^2/\text{s}$; *horizontal*: different simulation runs. Diffusion time $\Delta t_{exp} = 10\,\text{ms}$. Intensity is given in count. Scale bar: $5\,\mu\text{m}$.

Module #4 : Upon filtering, within the "segmentation"-module, the x/y-pixel positions of the local maxima are determined for each frame in "in_file_ROI_bg_filter"

[4] Using a bigger convolving or fitting kernel with the size of $7 \times 7\,\text{pixel}$, for example, had only a negligible effect on fitting precision, etc.; for convolution (module #3) and for fitting (module #5), the kernel was $5 \times 5\,\text{pixel}$.

after choosing a user-defined intensity threshold I_{th}. Maxima with intensities above the threshold are chosen as spots (listed in "spot_list_test").

The threshold I_{th} was chosen empirically and confirmed by simulations (see Fig. 8.10). In order to avoid confusion during the feature extraction (spot fitting) step, in addition only spots with a minimal spatial distance $\Delta x_{min} = 3\,\text{pixel}$ were selected.

Module #5 : In this "fitting" module, 2D-Gaussian spots are fitted to the – non-filtered – image stack ("in_file_ROI_bg"). Thereby, the spot positions are refined further in a non-linear noise-weighted way to extract additional features (height, width, local background) using the MATLAB "lsqnonlin"-routine. The spot parameters obtained are stored in "spot_fit_list".

For each pixel a specific weighting factor was computed, taken as the inverse of the total noise, in order to perform the noise-weighted fitting. The square of the total noise is given by the sum of the squared Gaussian read out noise σ_{ro}^2 and the squared Poisson-distributed shot noise σ_I^2. While σ_{ro} is constant for a specific CCD, σ_I depends on the CCD gain g and the effective pixel intensity $I_{0,eff}$ as the difference between the original pixel value I_0 and the CCD offset $I_{off,2}$.

Including the local background into the fit allows the analysis of images with a spatially varying fluorescence background which is usually present in biological samples.

The next two modules deal with automatic and visual control of the algorithm.

Module #6 : First, in the "checking" module #6, feature parameters exceeding certain user-defined values are automatically screened for in "spot_fit_list" . (It is an optional module since the fitting procedure turns out to be highly reliable, a minimum quality of input image data provided.)

Module #7 : Second, the "reconstruction" module (#7) builds a model of the image stack based on the fitted parameters in "spot_fit_list". A fast and comprehensive check whether the algorithm "comprehended" the movie can be done by visual inspection via the VIEW5D renderer [41].

Module #8 : In this "linking"-module, the spots are connected from frame to frame by a least-cost-function routine adapted from [83]. (To that end, one user-defined parameter, the maximum jump length $L_{\max}$, has to be provided to the algorithm.) This routine is based on a particle matching algorithm [16] employing a graph theory technique [44]. (In [83] a closer description of the algorithm can be found.)

The effect of $L_{\max}$ on the value of the diffusion constant D computed was validated and a value chosen accordingly to minimize its influence (see Fig. 8.10 and Appendix 13.4).

Module #9 : In the final element "trace analysis" the step density histogram from the trajectory data is calculated employing a statistically validated bin width[5] Δx_{bin}.

A visual control of the image stack was possible after each processing step (background removal, segmentation, fitting, linking, etc.) via VIEW5D.

6.2. Outline of experimental procedure

Single molecule tracking as performed in this thesis can be considered the result of three independent steps: the preparation of the sample system, the illumination of and the acquisition of fluorescence emission from this sample system and the computer-based analysis of the image sequence obtained.

Thus, parameters which influence the final outcome (here: sample parameter D) can be divided into three (more or less) independent classes:

- "hardware parameters" (acquisition related)
- "sample parameters" (related to the system under investigation) and
- "software" parameters (specific for the analysis algorithm used).

The following paragraph gives an overview of the sequence of the experimental, analysis and simulation steps leading to the results of this work.

Step #1 : Determination of hardware parameters

First, the relevant hardware parameters (gain g, read out noise σ_{ro}, pixel size Δx_{pix}) were determined or confirmed (if already given by the CCD manufacturer).

Step #2 : Sample preparation, image acquisition

After that, the sample system was prepared and real image data were acquired. Variable sample and hardware parameters were optimized in order to gain optimal image sequences (i.e., with a maximal SNR, well separated spots with a step distance in between frames that allows for reasonable tracking, etc.).

[5] Δx_{bin} is determined applying the Freedman-Diaconis approximation, $\Delta x_{bin} = 2R_{iq}/N^{1/3}$ with R_{iq} as the interquantile range of the step distances (i.e. the difference between the third and first quantiles) and N as the number of steps.

Step #3 : Image analysis and determination of software / sample parameters

In this step, the software parameters were empirically optimized in order to gain a set of sample parameters based on the hardware parameters known and by analyzing the experimental image data.

Step #4 : Validation of software parameters

Resting upon the hardware and sample parameters obtained in steps #1 and #3, the influence of the empirically determined hardware and software parameters on the determination of the "final" sample parameters (here: diffusion constant D), was assessed in step #4 (concerning accuracy and precision and potential bias in determination of D).

Therefore, for each parameter investigated, an individual set of image sequences was simulated and analyzed with the same image analysis software as the experimental image sequences.

Step #5 : Refinement of sample parameters

Finally, in a fifth step, based on the assessment of the hardware / software parameters in step #4, the sample parameters (obtained in step #3) were interpreted and, if necessary, corrected.

Focus of this work is the investigation of the influence of certain software parameters on the determination of the diffusion constant D and the determination of D itself (steps #4 and #5).

6.3. Potential imaging artifacts

Although the observation of the fluorescence emission of molecules is from its nature very low invasive to the system under investigation (as compared to, e.g. any mechanical manipulation), it has certain (potential) artifacts which shall be discussed here.

Focussing on single molecule imaging, if the molecules are immobilized (and a frame rate of tens of frames per second is not crucial), an excitation intensity well below 1kW/cm^2 can be used. However,in case of mobile molecules, relatively high excitation intensities I_{exc} of up to several kW/cm^2 are required to excite and collect enough photons for a decent SNR.

6.3.1. Phototoxicity & -bleaching

In cellular systems (*in vivo*), this might induce phototoxic stress leading to an undesired change of the system's properties under investigation.

In *in vitro* systems as investigated in this work, this artifact is not present, however, the illumination dose $I_{exc} \times \Sigma\Delta t_{exp}$ leads to considerable photobleaching of the fluorophore molecules, especially in case of the DiI-C_{18} molecules diffusing within the lipid membrane (see chapter 9).

In section 8.6.4, the effect of photobleaching on the determination of the diffusion constant is treated by simulations as part of the overall characterization of the image analysis algorithm.

6.3.2. Thermal effects

However, illumination with I_{exc} = 1-10 kW/cm^2 (ca. 30 mW illumination power) might lead to an increase in temperature within the sample, significantly biasing its specific properties (e.g. the diffusion constant).

To tackle this question, several facts have to be considered for each sample type discussed separately.

sample: Kaede-GFP

Starting with the sample for the photophysical investigations of the photoswitching protein (*Kaede*-GFP), on the one hand, the absorbance of the sample for the excitation light is almost negligible.

This is due to the fact that the sample consists out of two coverslides (of ca. 160 μm thickness) filled with aqueous PAA-gel. The only light absorbing compound are the *Kaede*-GFP-molecules themselves. Since they are present only in tiny concentrations of ca. 10^{-6}, however, they can not contribute to any potential heating of the sample. Reflections on the surfaces of the coverslips occur, of course, but they do not lead to any absorption which solely can increase the temperature.

sample: GUV-membranes

The sample for the investigation on membrane diffusion similarly consists of two coverslides enclosing purified water containing a small amount of lipids. However, the coverslips were each coated with a thin (few hundred nm) layer of ITO (Indium Tin Oxide) exhibiting an absorption[6] of maximal 8% at λ_{exc} = 514 nm (for the lipid marker DiI-C_{18}).

Due to the necessary excitation power of $P_{exc} < 30$ mW and excitation intensity of $I_{exc} < 10$ kW/cm^2, a potentially critical amount of heat could be absorbed by the ITO-layer. Although the sample was temperature stabilized during the

[6] spectra see Appendix 13.2, Fig. 13.1

measurements via an objective temperature control to $\pm 1\,\mathrm{K}$, potential thermal effects shall be discussed in the following.

To that end, detailed simulations on the evolution of temperature change ΔT during acquisition of an image sequence were performed in order to estimate the rise in the membrane temperature ΔT_{mem} and the effective product of membrane temperature and the normalized number of spots per frame,

$$\Delta T'_{mem,eff} = \Delta T_{mem} \times N(t)/N(0). \tag{6.1}$$

Additionally, for the experimental image sequences acquired, the diffusion coefficient D was analyzed separately for subgroups of frames belonging to different time intervals (100 ms, 430 ms and 830 ms after start of image acquisition) in order to check for potential time trends reflecting the heating of the sample.

Simulation

Absorbed solely by the ITO-layer (of a few hundred nm thickness), the heat ΔQ_{abs} is conducted by the underlying glass coverslip and the water/lipid mixture on top[7] determined by the ratio λ_w/λ_g, the thermal conductivity of water and glass, respectively, at room temperature. $\lambda_w \approx 0.55\,\mathrm{W/mK}$ [30] and $\lambda_g \approx 1.0\text{-}1.2\,\mathrm{W/mK}$ [94].

Therefore, $f_{dist} \approx 1/3$ of ΔQ_{abs} is conducted by the sample medium (which is approximated by pure water in the following calculations[8]).

Typically, for the measurements on GUV-membranes, the membranes chosen by the position of the focal plane, z_m, were situated ca. 100-200 μm *above* the coverslip surface. As the excitation light was not collimated but slightly focussed into the sample, the beam profile was larger at the position of the ITO layer, $z_0 = 0$, than at the focal plane, resulting in an effective absorption area $\Delta A_s \approx 200 \times 200\,\mu\mathrm{m}^2$ (corresponding to a circular disk of $\varnothing = 225\,\mu$m).

Assuming a homogenous illumination (on the scale of several tens of μm) and considering the situation at the center of ΔA_s ($x = y = 0$), the heat conduction occurs predominantly in 1D parallel to the z-axis.

The bigger z, the more resembles the 1D-conduction (in z-direction with a 2D area heat source ΔA_s) a 3D-process (isotropic with point-like heat source ΔV_s).

[7] Convection can be neglected because of the small relevant distances (a few hundred μm) and the – as will be – shown small temperature differences. Radiation is ineffective due to high absorbance of water and glass in the far IR, corresponding to room temperature

[8] a conservative estimation, because the lipid film on top of the ITO should decrease heat conduction;

However, because for 3D heat conduction, the heat flux density[9] decreases with increasing source distance for a stationary process (contrary to 1D conduction), assuming a 1D process is a conservative approach for the present case: The real rise in membrane temperature is lower than for the 1D conduction case, $\Delta T_{mem,eff} < \Delta T_{1D}$.

Since ΔT is directly proportional to ΔQ_{abs} via $\Delta T = \Delta Q_{abs}/\rho$ with ρ as heat capacity, solving the general 1D-heat equation

$$\frac{\partial}{\partial t}\,\Delta T\,(z,t) = D_w\,\frac{\partial^2}{\partial z^2}\,\Delta T\,(z,t)\,, \qquad D_w = \frac{\lambda_w}{\rho_w c_w} \tag{6.2}$$

(with $\rho_w = 4.2\,\mathrm{kJ/(Kkg)}$ and $c_w = 10^3\,\mathrm{kg/m^3}$ as the heat capacity and mass density of water) leads to

$$\Delta T\,(z,t) = \frac{\theta_0}{(4\pi D_w t)^{1/2}}\;\exp\left(-\frac{z^2}{4D_w t}\right) \tag{6.3}$$

with

$$\theta_0 = \frac{\Delta Q_{abs}}{\Delta A_{abs}\rho_w c_w}. \tag{6.4}$$

To that end, the following boundary conditions are assumed:

- The absorbed heat ΔQ_{abs} stays constant over the time $t \in \left[0, \tilde{t}\,\right]$ considered;
- $\Delta T\,(\infty, t) = 0\,; \quad t \in \left[0, \tilde{t}\,\right]$.

In the following, numerical simulations on basis of Eqns. 6.3 and 6.4 for a image sequence of 50 frames with $\Delta t_{exp} = 10\,\mathrm{ms}$ and $\Delta t_{ro} = 23\,\mathrm{ms}$ were performed leading to Fig. 6.2 (details see Appendix 13.2). To account for photobleaching (which reduces the number of molecules and steps present per frame with increasing measurement time t_{meas}, the temperature change ΔT is multiplied by the normalized number of spots per frame which decays exponentially with $\tau_{PB} = 0.66\,\mathrm{ms} = 20$ frames. The number of spots in frame n is directly proportional to the number of steps from frame n to $n+1$, thus, the *effective* change in temperature at a distance z from the coverslip surface has to be given as

[9] $\Delta Q_{abs}/\Delta A$ with ΔQ_{abs} the amount of heat conducted through an area ΔA in a unit time Δt

$$\Delta T_{\mathit{eff}}(z) = \int_0^{t_{meas}} \frac{\Delta T(z,t) \times N(t)}{N(0)}\, dt. \tag{6.5}$$

Due to the conservative assumptions, the simulated values for $\Delta T_{mem,\mathit{eff}}$[10] were above the real ones. This is especially true in case of a membrane distance $z = 50\,\mu$m because in the measurements, z exceeded generally $150\,\mu$m.

For realistic experimental conditions, therefore, $\Delta T_{mem,\mathit{eff}} < 0.5\,$K which is below the measurement accuracy of $\pm 1\,$K.

Experiment

To check for time trends detectable in the experimental data, subgroups of frames of the image sequences[11] were analyzed individually. The diffusion constants determined from frames #1-5, #11-15 and #21-30 (100 ms, 430 ms and 830 ms after begin of image acquisition) are displayed in Fig. 6.3. As can easily be seen, the data points show no trend over time, only statistical scattering.

Thus, the experimental data analysis confirms the finding of the analytical simulations that there is no significant increase in sample temperature due to excitation light absorption. Potential temperature increase is below the measurement accuracy of $\pm 1\,$K.

[10] $\Delta T_{mem,\mathit{eff}}$ is given by $\Delta T_{\mathit{eff}}(z)$ with z as the distance of the membrane from the coverslip.
[11] used to determine D in chapter 9

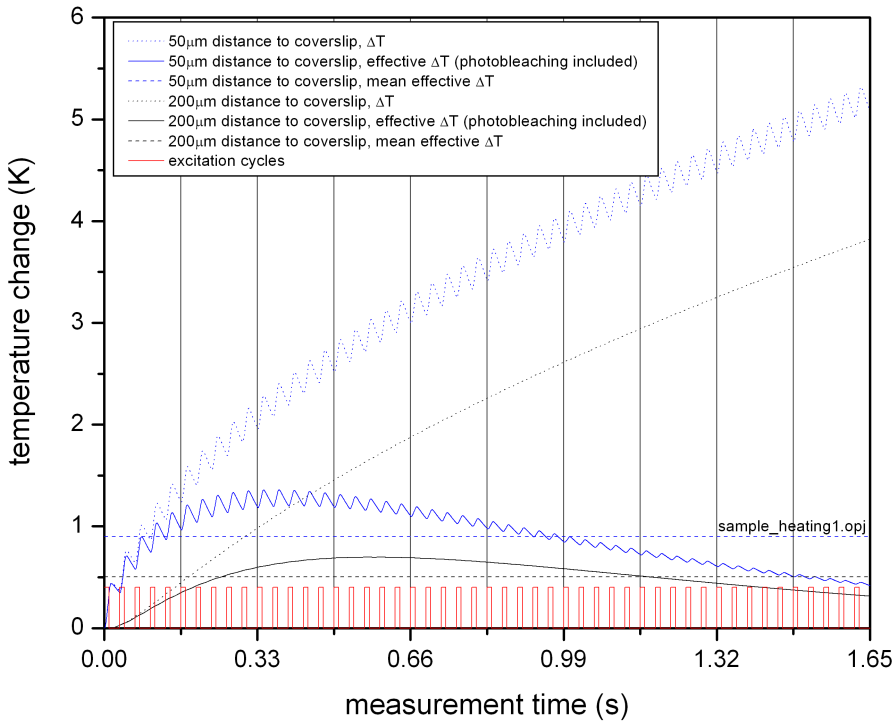

Figure 6.2.: Simulation of change in membrane temperature ΔT_{mem}, effective membrane temperature $\Delta T'_{mem,eff}$ and effective mean membrane temperature $\Delta T_{mem,eff}$. Displayed are the graphs for membrane position $z_m = 50\,\mu$m and $200\,\mu$m. To compensate for photobleaching which reduces the number of spots (and steps) over measurement time, the temperature curves (*dotted lines*) are multiplied by an the normalized number of steps which decays exponentially with $\tau_{PB} = 0.66\,\text{ms} = 20$ frames. The simulation shows a *worst-case-scenario*. However, even for $z_m = 50\,\mu$m, $\Delta T_{mem,eff} < 1\,\text{K}$ which is the measurement accuracy (see text and Appendix 13.2).

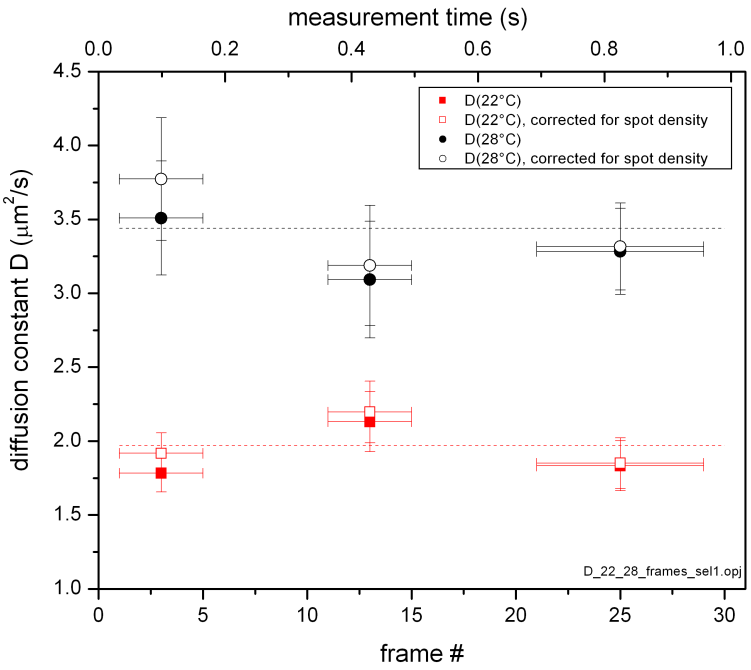

Figure 6.3.: Diffusion constant D determined by fitting of step distance histograms for different subgroups of frames (#1-5, #11-15 and #21-30; 100 ms, 430 ms and 830 ms after begin of image acquisition). Shown are data points for measurements of GUVs at 22 °C and 28 °C (±1 K). No time trend – signalling an artifact due to sample heating – is visible.

7. Sample preparation

7.1. Giant unilamellar vesicles (GUVs)

Giant unilamellar vesicles (GUVs) were grown using the electroformation technique developed by Angelova and Dimitrov [4, 24, 5].

This technique allows for the growth of truly unilamellar vesicles which could be checked obtaining a homogeneous fluorescence intensity among an ensemble of GUVs under the laser scanning microscope.

In order to fabricate the vesicles, first, a solution of cholesterol (5 mM), DLPC[1] (5 mM) and DiI-C_{18}(3) (2.5×10^{-8} mM) was prepared in chloroform and stored under Ar at $-20\,^{\circ}$C. (Cholesterol and DLPC were purchased from Avantilipids (AL, U.S.A.), DiI-C_{18}(3) from Molecular Probes / Invitrogen (CA, U.S.A.) and other chemicals from Merck, Darmstadt, Germany).

Then, two coverslips, coated on one side with indium tin oxide (ITO) (GeSim GmbH, Großerkmannsdorf, Germany) were carefully cleaned and each conductively connected to a copper tape.

To remove residual solvent, one of the coverslips was pre-heated at 65 °C for five minutes. After that, 10 mL of the lipid solution was spread evenly over its conducting side and left on the heater for ca. five minutes, thereby ensuring complete evaporation of the solvent.

In the next step, both coverslips were assembled in a sandwich-like fashion with the conducting sides facing each other. To avoid touching – and creating a volume reproducibly – the coverslips were separated by a plastic spacer ($\varnothing$: 3 mm).

Sealed with vacuum grease (Glisseal, Borer, Switzerland), the volume (ca. 200 μL) was subsequently gently filled with degased water (Lichrosolv, Merck, Germany).

The coverslips were then connected to an external power supply (1.2 VAC, 10 Hz; Conrad, Göttingen) for 1.5 hrs and kept at 60 °C. This procedure exposes the lipids in the mixture (surely above their transition temperature[2]) to an alternating electric field. Although the mechanism of the GUV formation process is not totally understood yet, this handling ensures a proper formation of the giant unilamellar

[1] DLPC is short for 1,2-Dilauroyl-*sn*-Glycero-3-Phosphocholine, a saturated phospholipid

[2] At the transition temperature, an ensemble of lipid molecules changes from the "liquid" to the "gel-phase", e.q..

vesicles, to safeguard for the case that the transition temperature was above room temperature.

As a result, the lipid layers swelled to a 3D "foam" with the smallest vesicles at the bottom and the largest at the top ($\varnothing$: 20-200 mm).

7.2. Green Fluorescent Protein Kaede

Green Kaede protein, kindly provided by Prof. A. Miyawaki, was produced and purified as described before in [3]. It was stored at −80 °C in buffer (10 mM Tris-HCl, 1 mM EDTA, 150 mM NaCl, pH 8.0). The protein was diluted in 10 mM MOPS-buffer, pH 7.0, before the experiments. Following the protocol given in [23], green Kaede protein was immobilized in polyacrylamide (PAA) gel at nanomolar concentrations to perform the imaging measurements. The protein concentration in the PAA gel was 71 nM for bulk measurements and between 0.9 nM and 7.6 nM for single molecule measurements.

Samples were prepared by mixing 1.0 ml Kaede protein solution in 10 mM MOPS buffer (pH 7.0) with 99 ml gel mix (in 1 ml gel mix : 550 ml acryl amide:bis-acryl amide, 38 : 2, 40%; 2.5 ml N,N,N',N'-tetramethylethylendiamine, 445 ml MOPS-Tris-buffer). The cleaning procedure for the coverslips consisted of several steps: First, the were ultrasonicated in a detergent solution, followed by a rinsing cascade (purified water (LiChrosolv, Merck, Darmstadt, Germany), propanol, acetone and purified water). Finally, they were exposed to an oxygen plasma. Sample solution in the amount of 1.0 ml was sandwiched in between two coverslips after adding 0.5 μL of ammonium persulfate solution (4%) to start the polymerization reaction. After a few minutes waiting time, the gel was polymerized.

To acquire bulk fluorescence emission spectra of the green and the red protein, a protein solution in a micromolar concentration was used, diluted in 10 mM MOPS-buffer, pH 7.0.
All measurements were carried out at room temperature (22 °C).

Part III.

Results

8. Characterization of image analysis algorithm

The versatility for different spot environments, combined with its robustness and a small number of relevant user-defined parameters are major advantages of the presented analysis tool: The software can detect, characterize and track an arbitrary number of spot-like features which might vary on a frame to frame base.

Additionally, the quality of the data processing itself can be easily assessed visually by reconstructing each image frame based upon the feature parameters extracted. Therefore, potential processing errors or artifacts can be recognized and corrected.

8.1. Description of images

The dye molecules used to label the lipid bilayer are practically limited to the liquid bilayer membranes itself. Its position relative to the setup is stable over minutes (see Fig. 8.1). Thus, typical fluorescence images as displayed in Fig. 8.2 consist of several spots moving randomly in a 2D plane.

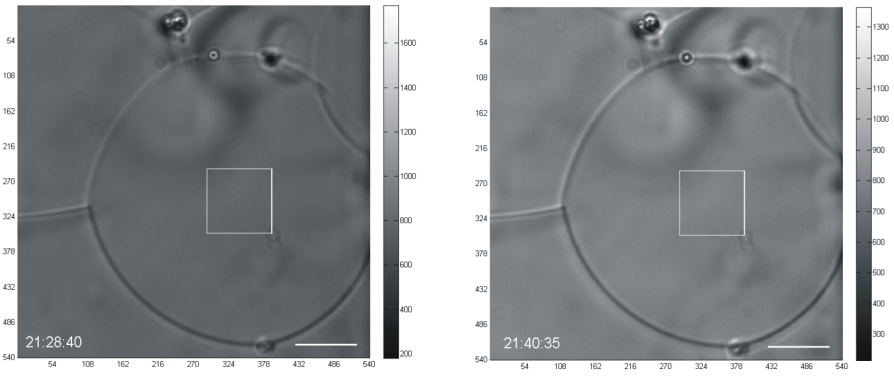

Figure 8.1.: White light transmission image of GUV in its equatorial plane (full frame), before (*left*) and after (*right*) acquisition of sequence of fluorescence images. White square gives position of ROI in 8.2. Time in between (*left*) and (*right*): ca. 12 min. Scale bar: 10 μm. Intensity in count.

With a slightly higher concentration in the center, the spots are distributed randomly over the field of view. Characteristical is a typically low signal to noise ratio (SNR) in the range of 3-6 and a blurring due to diffusion during acquisition time Δt_{exp}.

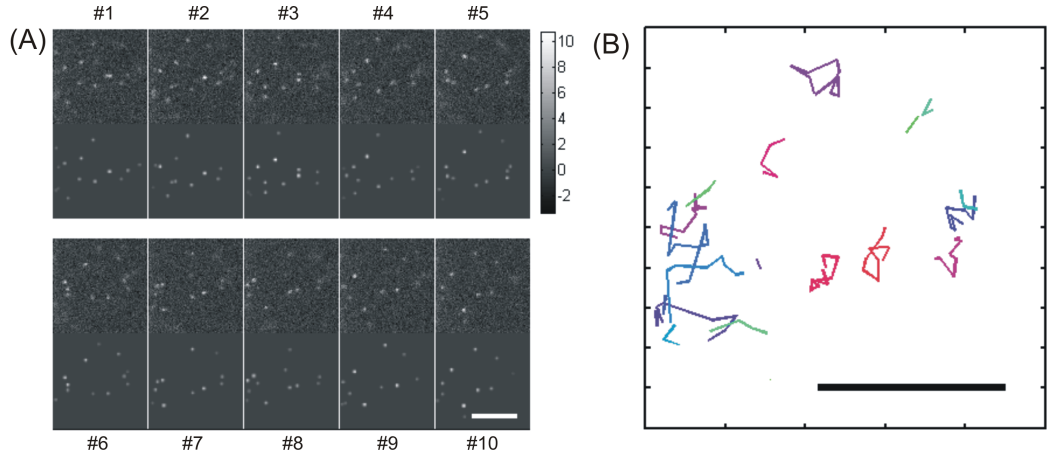

Figure 8.2.: (*A*) Sequence of fluorescence images of single *DiI*-molecules diffusing within lipid bilayer membrane of same GUV (upper pole, 20 μm above equatorial plane) as shown in Fig. 8.1. Displayed are first ten images, raw (*top*) and reconstructed, based on fitted parameters (*bottom*). Lag time in between frames $\Delta t_{lag} = 33$ ms. Scale bar: 5 μm. Intensity in count. (*B*) Traces extracted from the previous ten images (Scale bar: 5 μm).

8.2. Localization precision Δx_{loc}

8.2.1. Excursus: localization accuracy

As already discussed tentatively in paragraph 4.1.4, the localization *precision* Δx_{loc} – the statistical uncertainty in position determination – plays a crucial role in most single particle tracking applications. This is due to the intense importance of the actual position of fluorescent markers within cellular systems for many scientific questions, e.g., the mechanisms of molecular motor activity [43] or the tracking of single protein molecules at the boundary of intracellular compartments [55].

However, first the localization *accuracy* $\Delta x_{loc,acc}$ – the bias of the peak position determination – shall be elucidated.

Thus, in Fig. 8.3, $\Delta x_{loc,acc}$ is plotted for an ideal (noise-free) simulated spot (2D Gauss, std.dev $\sigma_{simu} = 1.0$ pixel), fitted with a 2D Gauss model (std.dev $\sigma_{fit} = 1.2$ pixel) as function of the peak position within a single pixel (see *inset*).

To fit the spots, the value for the model std.dev. σ_{fit} was fixed to 1.2 pixel for several reasons:

First, from the experiment, immobilized as well as spots diffusing with $D \approx 2\,\mu\text{m}^2/\text{s}$ exhibit a (fitted) spot std.dev. σ_{fit} between 1.1 and 1.3 pixel.

Second, fitting spots which were simulated with realistic parameters (spot emission intensity, spot std.dev., noise, etc.) employing either a fixed or free σ_{fit} showed no significant influence on the localization precision.

For example, whether fixing $\sigma_{fit} = 1.2\,\text{pixel}$ or leaving it as free fit parameter, e.g., causes a $\Delta x_{loc} < 8\,\text{nm}$ (average for 500 spots, simulated with $\Delta t_{exp} = 10\,\text{ms}$, $D = 1.0\ \mu\text{m}^2/\text{s}$, $I_0 = 600\,\text{count/s}$).

Third, fixing σ_{fit} to 1.2 pixel allows for a fast and reliable run of the fitting procedure itself.

It is illustrative to consider the relative integrated intensity $I_{int,rel}$ for such a spot within a $5 \times 5\,\text{pixel}$ ($7 \times 7\,\text{pixel}$) ROI around the spot peak[1]. In case the peak is situated at the corner of a pixel (position B), $I_{int,rel} = 90.6\%$ (98.9%), in case it is localized at the center (position A), $I_{int,rel} = 93.7\%$ (99.5%).

Therefore, it can easily be understood that the maximum localization accuracy depends on the size of the fitting kernel, amounting to ca. 1.4 nm (0.3 nm) for a $5 \times 5\,\text{pixel}$ ($7 \times 7\,\text{pixel}$) fitting ROI.

However, the SNR of the spots is typically low due to limitations in

- detection efficiency η_{tot}
- emission intensity I_0 (leading to shot noise σ_I)
- read out noise σ_{ro} and
- diffusion during finite exposure time Δt_{exp},

In this case, as the following Figs. 8.5 ff. will show, the localization *accuracy* – the bias – in the range of a few nm is exceeded by the localization *precision*[2] – the statistical scattering in the range of a few tens of nm.

Therefore, in the following, the role of Δx_{loc} will be discussed more closely.

8.2.2. Spot simulation

In order to include realistic noise into the spot images, the CCD parameters gain $g = 6.4\,\text{e/count}$ and read out noise $\sigma_{ro} = 5.3\,\text{e}$ (RMS) were utilized to generate typical intensity-dependent noise[3] which was added to the (initially) noise-free

[1] computed numerically

[2] In case of high SNR and slow (diffusive) movement, the localization accuracy can be of higher importance compared to the localization precision.

[3] superimposed read out and shot noise

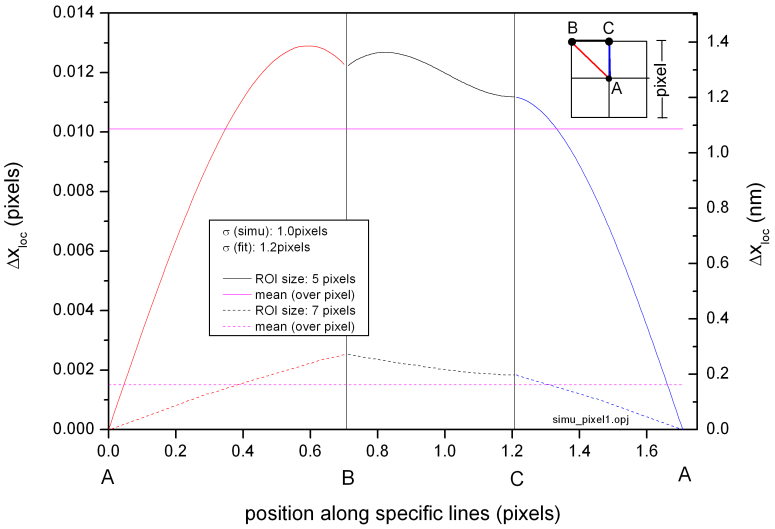

Figure 8.3.: Localization precision Δx_{loc} as function of position of peak center within a single pixel, computed for ROIs around peak of two different sizes (5×5 and 7×7 pixel). The peak is immobilized, no noise is present. Displayed is Δx_{loc} along symmetry lines (see inset). For comparison, the right axis shows Δx_{loc} for 1 pixel = 107.5 nm (Typical for a magnification $M = 60$ and a Sony ICX285AL CCD chip (CoolSnap HQ, Roper Scientific)).

images. This can be seen in Fig. 8.4 where a series of images, (left/right side: with/without noise) is displayed (see figure caption).

The emission intensity was chosen to 600 count/s, close to the average level of real spots (see p. 102). Displayed are five spots for a specific D-value in the range from 0 to 10 μm^2/s. Especially for $D \leq 5\,\mu$m^2/s, with the here used acquisition time of 10 ms the distortion of several spots from a roughly circular shape becomes obvious.

Therefore, for $\Delta t_{exp} = 10$ ms, an approximation (fitting) of the spots by a 2D Gaussian appears appropriate for $D \leq 5\,\mu$m^2/s.

8.2.3. Δx_{loc} as function of emission intensity I_0

As suggested above, the (peak) emission intensity I_0 determines largely the localization precision as can be seen in Fig. 8.5. The size of the fitting kernel, however, contributes only in a minor way. Most of typical experimental spot intensities were in the range from 300 to 600 count/s, so Δx_{loc} was in between 50 and 25 nm.

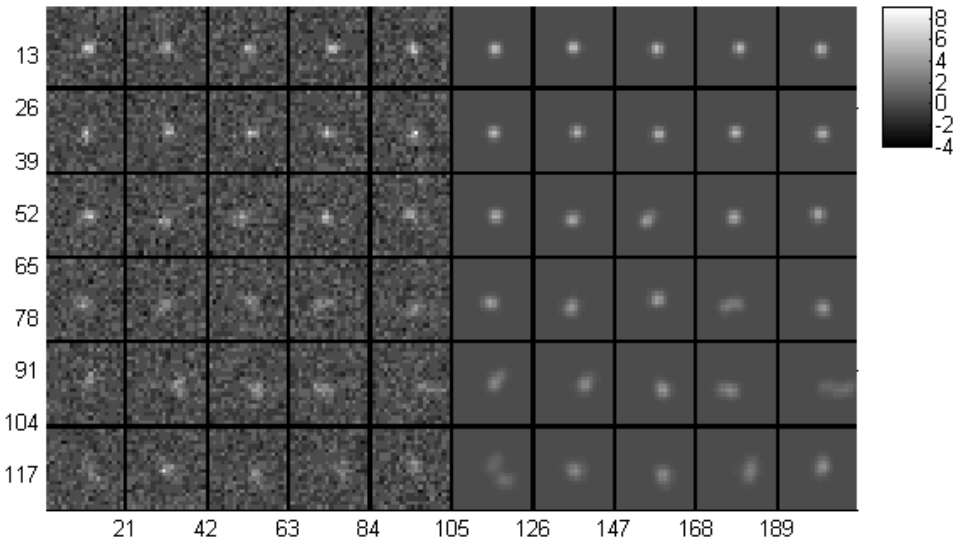

Figure 8.4.: Simulated spots for different diffusion constants (5 examples each). Peak detection intensity $I_{det} = 600\,\text{count/s}$, exposure time $\Delta t_{exp} = 10\,\text{ms}$, spot standard deviation $\sigma = 1.0\,\text{pixel}$ ($1\,\text{pixel} = 107.5\,\text{nm}$). *Left (right) side*: spot with (without) CCD read out and photon shot noise. CCD parameters (CoolSnap HQ, Roper Scientific): read out noise $\sigma_{ro} = 5.3\,\text{e}$, gain $g = 6.4\,\text{e/count}$; From top to bottom: $D = 0.0/0.1/1.0/2.5/5.0/10.0\,\mu\text{m}^2/\text{s}$

The effect of the specific Δx_{loc} on the precision of the diffusion constant D can be roughly estimated by

$$\Delta D \approx \frac{\Delta x_{loc}^2}{4\Delta t_{lag,eff}}. \tag{8.1}$$

With $\Delta t_{lag,eff} = 29.7\,\text{ms}$ (see p. 100), $\Delta D \approx 2.1 \times 10^{-2}\,\mu\text{m}^2/\text{s}$ (for $\Delta x_{loc} = 50\,\text{nm}$) and $\Delta D \approx 5.3 \times 10^{-3}\,\mu\text{m}^2/\text{s}$ (for $\Delta x_{loc} = 25\,\text{nm}$).

Considering the diffusion constant values in the range of $1\,\mu\text{m}^2/\text{s}$ or above, $\Delta D/D \leq 2\%$ even for relatively faint spots ($I_0 = 300\,\text{count/s}$). Since Δx_{loc} for the experimental spot intensity is ca. 30 nm and the experimental diffusion constant is $\approx 2.5\,\mu\text{m}^2/\text{s}$, $\Delta D/D \ll 1\%$.

Thus, the contribution of the localization precision and localization accuracy to the determination of the diffusion constant can be neglected for the specific experimental system investigated in this thesis.

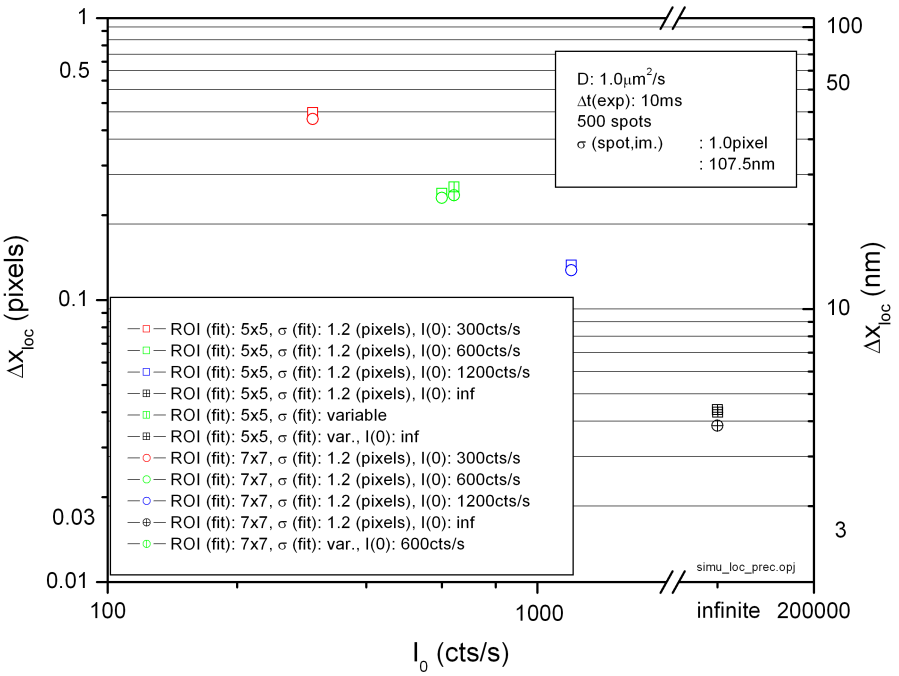

Figure 8.5.: Localization precision Δx_{loc} as function of emission intensity $I_0 = 300; 600; 1200; \infty$ count/s for different fitting ROIs (5×5 and 7×7 pixel) and different fitting spot standard deviation ($\sigma_{fit} = 1.2$ pixel and σ_{fit} as fitted; $D_{simu} = 1.0\,\mu\text{m}^2/\text{s}$, $\Delta t_{exp} = 10$ ms, $\sigma_{simu} = 1.0$ pixel).

8.2.4. Δx_{loc} as function of diffusion constant D

If Δx_{loc} is plotted versus the diffusion constant for several emission intensities I_0 as parameters, an almost exponential dependence can be recovered (Fig. 8.6). In the noise-free case and with practically non moving spots, with a finite fitting ROI of 5×5 pixel a minimum $\Delta x_{loc} \approx 1$ nm can be reached, corroborating the results of Fig. 8.3.

8.2.5. Δx_{loc} as function of SNR

In Fig. 8.7 finally, the localization precision is given as function of the signal to noise ratio. Considering data points for a specific diffusion constant, an almost exponential dependence $\Delta x_{loc} \sim k \times \text{SNR}$ with $k < 0$ seems possible, mirroring the results in Fig. 8.6.

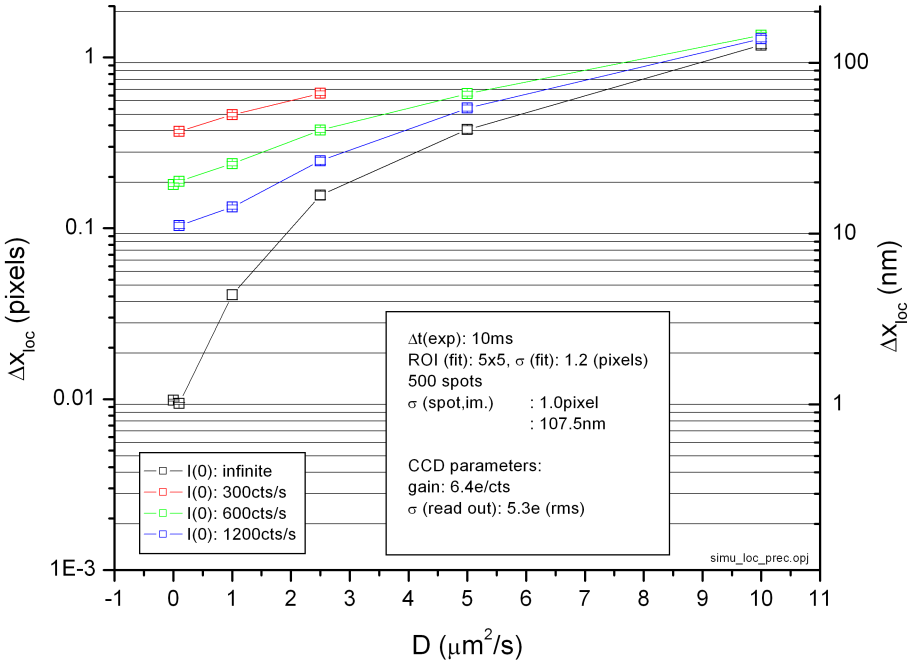

Figure 8.6.: Localization precision Δx_{loc} as function of the diffusion constant $D = 0; 0.1; 1.0; 2.5; 5.0; 10.0\,\mu\text{m}^2/\text{s}$ for various peak intensities $I_0 = 300; 600; 1200; \infty$ count/s for the fitting ROI 5×5 and $\sigma_{fit} = 1.2$ pixel.

8.3. Sources of bias on determination of D

On the one hand, a low SNR limits the localization precision (resulting in a lower precision in the determination of the diffusion constant D but no bias [14]), on the other hand, the diffusion during Δt_{exp} *can* introduce a bias of D [79].

8.3.1. Finite acquisition time Δt_{exp}

The latter effect – the bias[4] on D – is especially pronounced if Δt_{exp} is comparable to the lag time (the time between two consecutive frames) Δt_{lag}.

In order to obtain enough fluorescence photons (and to increase the SNR), a exposure time of 10 ms had to be chosen. To track the spots in a highly unambiguous way, $\Delta t_{lag} = \Delta t_{exp} + \Delta t_{ro}$ was selected to 33 ms, as short as the minimum CCD read out time $\Delta t_{ro} = 23$ ms allowed. (The longer Δt_{lag}, the less likely is a specific link between two spots in frames n and $n + 1$.)

[4] or artifact, if not properly accounted for

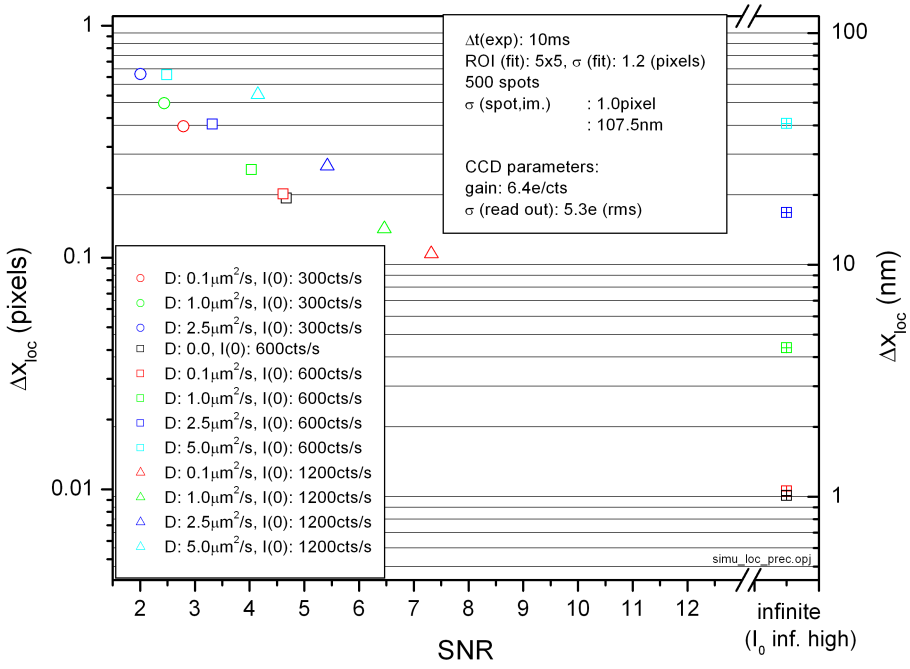

Figure 8.7.: Localization precision Δx_{loc} as function of the signal-to-noise ratio (SNR) which depends implicitly on the diffusion constant D and peak emission intensity I_0. The fitting ROI was 5×5 pixel and the fitting spot standard deviation $\sigma_{fit} = 1.2$ pixel was used.

This potential bias on the diffusion coefficient is discussed in paragraph 8 theoretically [79] and on basis of simulated trajectories.

8.3.2. Finite spot density ρ_{spot}

In addition to diffusion during exposure which effect can be corrected for by [79], Eqn. 14, a finite spot density ρ_{spot} leading to intersection of trajectories and ambiguous linking alternatives among neighboring spots can introduce a systematic underestimation of D. This is the case if the inter-spot-distance Δx_{is} is comparable to the average step distance Δx_{step}.

Furthermore, in single molecule image sequences, the number of spots typically decreases over time due to photobleaching. In case of unexposed sample regions adjacent to the illuminated ROI, spots may enter or leave the ROI via diffusion

within the lipid membrane. (Waiting a few minutes between two measurements allows dye molecules to diffuse into the previously bleached ROI to practically "replenish" the bleached ones.)

The effect of a finite ρ_{spot}, whether constant or decreasing via photobleaching, is investigated in paragraph 8 (see Fig. 8.14).

We consider our image data typical for single molecule applications compared to other works, especially concerning the diffusion constant D (ca. 1-5 μm^2/s [85]) and the SNR (2-10 [55] ; 5-70 [86]; 15 [36]).

8.4. Successful acquisition of single dye molecules diffusing within a liquid lipid membrane

As described above, single lipid marker molecules (DiI-C_{18}(3)) were imaged in an artificial lipid bilayer membrane of a giant unilamellar vesicle. To that end, a small ROI (100×100 pixel) close to the x/y-center (pole) of the GUV was selected to acquire the fluorescence image sequence.

This was done by moving the objective in z-direction and thereby raise the focal plane by 20 μm in order to focus the membrane of the GUV in its "polar" region. As the images with non-blurred spot showed, at this site the membrane was roughly parallel to the focal plane. After each acquisition of fluorescence images, it was checked by illumination with white light that the GUVs were spatially stable ($|\Delta x, y| < 0.3\,\mu$m) so that trajectories of single molecules diffusing in the x-y-plane could be extracted.

In general, due to the curvature of the vesicle, the spots in the frame center are more in focus than the spots closer to the rim.

If the membrane bends away from the focal plane, the lipid marker molecules follow its shape. Therefore, a bent membrane might affect the lateral distances as well as the axial properties of the spot image, i.e. the spot intensity[5].

However, geometric calculations yield that for a GUV with a diameter $\varnothing = 20\,\mu$m, at 5 μm lateral distance from the ROI center (equals the scale bar in Fig. 8.2), the axial distance between the focal plane and the membrane is given by $\Delta z_{bend} < 0.64\,\mu$m; the lateral distance differs by $\Delta x_{bend} < 0.054\,\mu$m if measured on the focal plane and the membrane, respectively. (To safeguard the precision, all GUVs included in the analysis had $\varnothing \geq 20\,\mu$m, so this is a worst case estimation.)

Furthermore, if trajectories of a simulated spot diffusing on a 50×50 pixel area (with the pole of the GUV in the center) over 3000 frames in case of bending

[5] due to the off-center cross section of the point spread function imaged to the CCD chip;

corrected and not corrected were compared, D_{fit}/D_{simu} could be determined to 1.00 ± 0.03 and 0.99 ± 0.03, respectively.

Thus, although finding the proper z-position within ca. $\pm 0.5\,\mu$m is crucial concerning the SNR, however, the effect of blurring and membrane bending on the determination of D is very small as long as the spot intensity is above the detection limit.

8.5. Strong agreement between experimental and simulated data

Trivially, in order to gain relevant information about experimental from simulated data, there has to be a high degree of similarity between the sets of relevant parameters of the experimental and the simulated data. Therefore, hardware parameters (gain g, read out noise σ_{ro}, pixel size[6] Δx_{pix}, exposure time Δt_{exp}, read out time Δt_{ro}, spot width Δx_{spot}, spot emission intensity[7] I_0) and sample parameters (diffusion constant D, spot density ρ_{spot} photobleaching time τ_{PB}) were included as relevant parameters into the image sequence simulations.

Fig. 8.8 displays a set of experimental (column #1) and simulated (column #4) raw images. The corresponding automatically reconstructed images (after processing) are shown in columns #2 and #5, the residuals are given in columns #3 and #6. In rows #1, #2 and #3 frames #1, #15 and #30 are displayed.

Since the simulations were performed with the (sample) parameter set obtained from several sequences of experimental images, consequently, both image sets show a high degree of similarity.

The number of spots decreases strongly between frames #1 and #30 due to photobleaching of the molecules. (However, stopping the illumination of the ROI for a few minutes allows the lipid markers to diffuse back laterally from other parts of the membrane. It is known that the distribution coefficient of the dye used between the lipid membrane and the surrounding aqueous medium is very high so that basically all fluorophore molecules are dissolved in the lipid phase.)

The negative values on the intensity scale bar (right) result from the Gaussian background and the subtraction of the background offset.

Comparing columns #1 with #2 and #4 with #5 visualizes the performance of the

[6] In this paper, "pixel" either describes a light sensitive CCD element in image space or the edge length of such an element (also given as Δx_{pix}).

[7] The effective spot height $I_{spot,eff}$ is the maximum spot amplitude above background and depends implicitly on D and the spot emission intensity I_0. The spot emission intensity I_0 itself depends on the excitation intensity I_{exc} and is, therefore, considered rather a "hardware" than a "sample" parameter in this context.

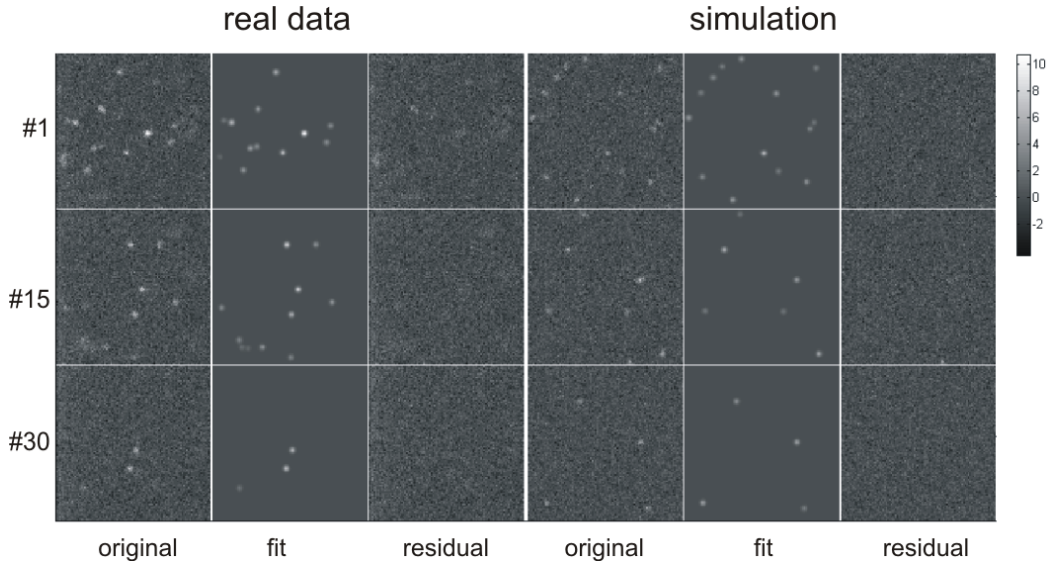

Figure 8.8.: Image sets of one selected experimental (*left three columns*) and one simulated (*right three columns*)sequence of images. The simulation was performed with the parameter values matching to the experiment. *Col.* #1 and #4 (from left): raw images. *Col.* #2 and #5: corresponding automatically reconstructed images (after processing). *Col.* #3 and #6: residuals. In *rows* #1, #2 and #3 frames #1, #15 and #30 are displayed. Lag time in between frames $\Delta t_{lag} = 33\,\text{ms}$. length of each image: $10.7\,\mu\text{m}$. Intensity in count.

analysis tool on the one hand. As the (almost) empty residual images (columns #4 and #6) show, the images are virtually recognized and "comprehended" by the algorithm.

On the other hand, the similarities between columns #1 and #4 (#2 and #5) demonstrate the performance of the *simulation* tool to generate image sequences which are basically identical to the experimental ones.

Both features of the algorithm, the analytic and the synthetic part are necessary for the validation of the algorithm's analytical competence.

8.6. Successful evaluation of the influence of hardware and software parameters

8.6.1. Effect of finite acquisition time

In case each frame is captured by illuminating the sample for an exposure time Δt_{exp} and subsequent read out during Δt_{ro}, a lag time $\Delta t_{lag} = \Delta t_{\text{exp}} + \Delta t_{ro}$ can be

defined. Since diffusion takes place also during Δt_{exp} and only the superposition (= mean position) $\bar{r}(t) = \langle r(t') \rangle$; $t' \in [t; t + \Delta t_{exp}]$ is recorded, this can lead to a systematic deviation in the determination of D_{fit}. Therefore, in case of Fickian diffusion, the *efficient* lag time $\Delta t_{lag,eff}$ is given by

$$\Delta t_{lag,eff} = \Delta t_{lag} - \Delta t_{exp}/3 = \Delta t_{ro} + 2/3 \times \Delta t_{exp} \tag{8.2}$$

as calculated in [79] (Eqn. 14).

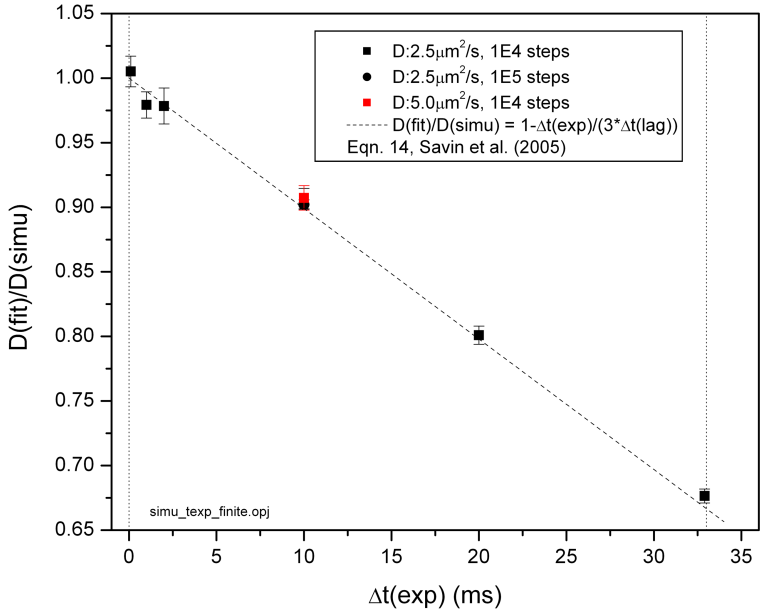

Figure 8.9.: Dependence of the relative diffusion constant D_{fit}/D_{simu} on the exposure time $\Delta t_{exp} = 0.1\,\text{ms} \ldots 29.8\,\text{ms}$., relative to $D_{simu} = 2.5 \mu m^2/s$. D_{fit} was determined by fitting step distance histograms to Eqn. 9.1. Shown are data from simulated trajectories consisting of 10^4 and 10^5 steps. $D_{simu} = 2.5\,\mu\text{m}^2/\text{s}$, $\Delta t_{lag} = 33\,\text{ms} = const.$

This could be verified by simulation (Fig. 8.9). Assuming a constant $\Delta t_{lag} = 33\,\text{ms}$, "primary" spot trajectories of $33s$ and $330s$ (10^4 and 10^5 substeps of duration $\Delta t_{substep} = 0.1\,\text{ms}$) length were generated, for $D = 2.5\,\mu\text{m}^2/\text{s}$ and $D = 5.0\,\mu\text{m}^2/\text{s}$, under variation of Δt_{exp} from 0.1 ms to 32.9 ms. After computing the mean positions for each exposure period, "secondary" trajectories were subsequently generated by connecting these mean positions. (For example, for $\Delta t_{exp} = 10\,\text{ms}$ – and, consequently, $\Delta t_{ro} = 23\,\text{ms}$, the positions of substeps 1-100, 331-430, 661-730, ... were each summed up to gain the mean positions.)

In case of $\Delta t_{lag} = 33\,\text{ms}$ and $\Delta t_{exp} = 10\,\text{ms}$, $\Delta t_{lag,eff} = 29.7\,\text{ms}$ can be obtained from Eqn. 8.6.1.

For the following simulations of diffusing spots, always $D = 2.5\,\mu\text{m}^2/\text{s}$ was assumed based on the D-values of the experimental system which were around 2-3 $\mu\text{m}^2/\text{s}$, according to step #3, paragraph 6.2.

These trajectories were analyzed by histogramming the step distances[8] and fitting a Rayleigh distribution [2]

$$p\,(r, \bar{r_t})\ dr = \frac{2r}{\bar{r_t}^2} \times \exp\left(-\frac{r^2}{\bar{r_t}^2}\right)\ dr \quad \text{with} \quad \bar{r_t}^2 = 4\,D_{fit}\,\Delta t_{lag,eff} \tag{8.3}$$

to the histogram. (This method was also used to analyze the experimental data.)

The ratio between the fitted and the intrinsic diffusion coefficients, D_{fit} and D_{simu}, behaved as $\frac{D_{fit}}{D_{simu}} = 1 - \frac{\Delta t_{exp}}{3\,\Delta t_{lag}}$ and is the same for $D_{simu} = 2.5\,\mu\text{m}^2/\text{s}$ and $D_{simu} = 5.0\,\mu\text{m}^2/\text{s}$, as predicted by [79] (Eqn. 14).

8.6.2. Effect of segmentation intensity threshold I_{th}

For segmentation of the spots and separation from background, a user-defined intensity threshold I_{th} has to be provided to the algorithm. After convolution of the raw image with a 2D Gauss kernel, a set of neighboring pixels of the convolved image is considered ("detected") as a "spot" if for these pixels $I^{conv}_{spot,eff} > I_{th}$. The bigger I_{th}, the higher the percentage of spots detected, whether they are "real" (originating from fluorescent molecules) or "false" (from unspecific, out-of-focus fluorescent background, CCD read out noise, etc.).

To determine the percentage of detected real and false spots, synthetic images with varying spot emission intensity I_0 were generated, with I_0 as the peak intensity of a noise-free, immobile spot ($[I_0] = \text{count/s}$).

In order to simulate the synthetic sample images, the relevant hardware, sample and software parameters as given in Tab. 8.1 were kept constant[9]. Therefore, a changing effective spot height $I_{spot,eff}$ reflected a variation in I_0. ($I_{spot,eff}$ is defined here as the peak spot height above background as fitted by the algorithm.)

As the convolution of an image (in module #3) is a linear process, neglecting the noise, the spot height in the filtered image $I^{conv}_{spot,eff}$ is proportional to $I_{spot,eff}$.

[8] The bin width is determined by the Freedman-Diaconis approximation (see footnote 5, p. 77).

[9] The value for Δx_{filt} was determined empirically by filtering real images and chosen as compromise between noise suppression and feature (spot) enhancement. Likewise, the value for $\Delta x_{spot,fit}$ was determined by fitting real spots with the spot width as free parameter.

Hardware parameters:		
gain	g	6.4 e/count
read out noise	σ_{ro}	5.3 e
pixel size	Δx_{pix}	107.5 nm
exposure time	Δt_{exp}	10 ms
read out time	Δt_{ro}	23 ms
spot width	Δx_{spot}	2.0 pixel
Sample parameters:		
diffusion constant	D	2.5 μm^2/s
spot density	ρ_{spot}	1 spot/frame
photobleaching time	τ_{PB}	∞
Software parameters:		
filter kernel width	Δx_{filt}	2.0 pixel
fitting spot width	$\Delta x_{spot,fit}$	2.4 pixel

Table 8.1.: Relevant *hardware*, *software* and *sample* parameters

Therefore, with decreasing I_{th} a higher number of pixels fulfill $I^{conv}_{spot,eff} > I_{th}$ leading to a rising number of detected spots.

In Fig. 8.10 the percentage of spots detected is given as function of I_0 for different I_{th} values. As can be seen, even with a relatively small value of $I_{fit} = 1.0$ count, almost no false spots are detected. Therefore, for spot segmentation within real images, $I_{th} = 1.5$ count was chosen.

8.6.3. Calibration of spot emission intensity from fitting spot height

In order to determine the integral intensity of a spot[10], we plotted the spot height $I_{spot,eff}$ (as determined in module #5) as function of the spot emission intensity I_0 (input parameter to the simulation) shown in Fig. 8.11.

To that end, a sequence of 500 frames was simulated with the same set of relevant hardware (g, σ_{ro}, Δx_{pix}, Δt_{exp}, Δt_{ro}, Δx_{spot}), sample (D, ρ_{spot}, τ_{PB}) and software (Δx_{filt}, $\Delta x_{spot,fit}$) parameters as above (Tab. 8.1). With the intensity threshold[11] I_{th} set to 1.5 count, the spot emission intensity was varied from $I_0 = 300$ count/s to 700 count/s (amounting to 3.0-7.0 count for the excitation time $\Delta t_{exp} = 10$ ms).

As can be seen from Fig. 8.11, the fitted effective spot height $I_{spot,eff}$ for simulated

[10] which is directly proportional to the fluorescence emission intensity of a molecule
[11] as software parameter

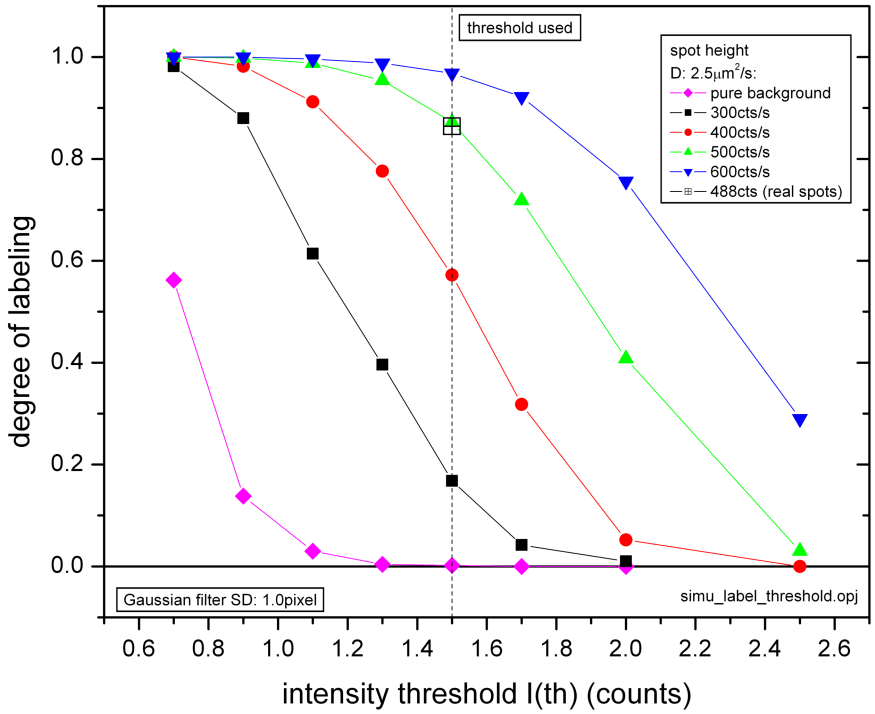

Figure 8.10.: Degree of detection (zero: no spots, one: all spots detected) as function of intensity threshold I_{th} (count). Prior to spot identification, image was convolved by $2D$ Gaussian filter kernel ($\sigma_{Gauss} = 1.0$ pixel).

spots (black squares) rises linearly with the spot emission intensity I_0 according to

$$I_{spot,eff} = m * I_0 + b = 0.36 * I_0 + 1.9\,\text{count} \tag{8.4}$$

($\Delta t_{exp} = 10$ ms is assumed for the value of I_0).

The relatively flat slope of the fit, $m = 0.36$, can be explained by the diffusion taking place during image acquisition (leading to spot blurring). The offset $b = 1.9$ count can be attributed to the read out noise σ_{ro} which is predominantly Gaussian at low I_0 levels (and independent of I_0) so that the fitting routine in module #5 extracts an artificial spot height.

With Eqn. 8.4, I_0 of our real data could be computed yielding $I_0 = 4.9 \pm 0.76$ count/10 ms.

Under the assumption of hardware parameters (g, Δx_{pix}, Δt_{exp}, Δx_{spot}) as chosen above and, further, a total collection efficiency $\eta_{tot} = 0.09 \pm 0.02$ e/ph of the

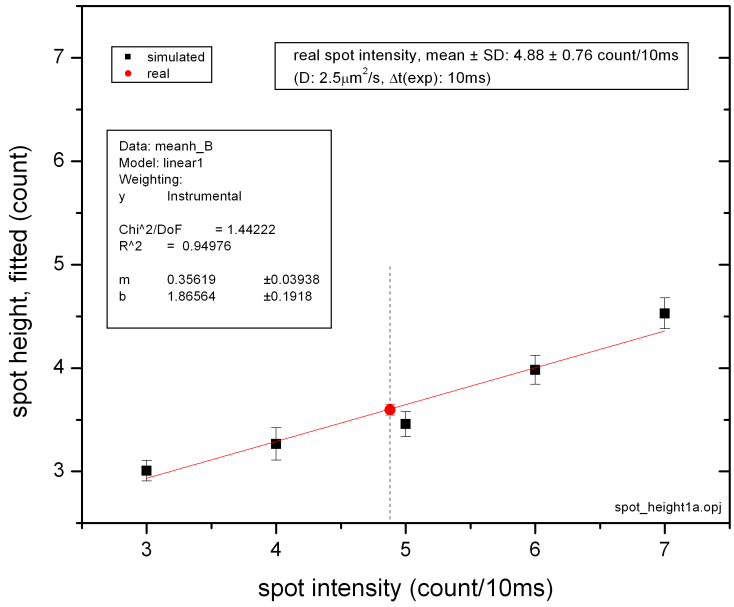

Figure 8.11.: Spot height $I_{spot,eff}$ (determined in module #5) displayed as function of the simulated spot emission intensity I_0 (for $\Delta t_{exp} = 10\,\text{ms}$; on average, 440 simulated spots were included per data point.) Subsequently, a weighted linear fit was computed to gain the quantitative relation between $I_{spot,eff}$ and I_0 (see text). Based on this, the average emission intensity of real spots (2550 spots included) could be determined to 4.88 count/10ms.

setup[12], we find $I_{spot}^{ph} = (3.2 \pm 0.85) \times 10^3$ ph/10ms as mean emission intensity and $N_{tot} = (6.4 \pm 1.7) \times 10^4$ ph as the total number of photons per molecule[13]. (see Appendix 13.1).

The error (1σ) of I_{spot}^{ph} is computed including the uncertainties in I_0 and η_{tot} (calculated using error propagation). However, the relatively small number of N_{tot} might be attributable either to an still optimistic assumption of certain individual transmittances $\tilde{T}_i$ or to the existence of chemical agents leading to fluorescence quenching and/or premature photobleaching.

8.6.4. Effect of maximal step distance, finite spot density and photobleaching

After having spots identified and their features extracted (modules #4 and #5), the individual spots have to be linked to obtain trajectories (module #8). If two

[12] see p. 68
[13] assumed $\tau_{PB} = 0.2\,\text{s}$

or more spots with identical features are present in two consecutive frames, no unique solution to link them exists. Besides, linking the spots "by hand" is a tedious work prone to subjective bias. Therefore, the automatic linking routine suggested in [16, 83] – in the following called *Link_trajectories* – was employed, requiring a user-defined parameter[14] L_{max} which gives the maximum step distance that can occur within one trajectory.

The influence of this parameter on the determination of D shall be discussed in the following under consideration of a finite spot density ρ_{spot}. This evaluation appears necessary, since a bias in the determination of D arises if the spot density ρ_{spot} is high enough that the average inter-spot distance Δx_{is} between two neighboring spots within *one* frame becomes comparable to the average step distance $\bar{r}_t$ of a spot between two successive frames. The reason for this bias is the erroneous linking of spots belonging to different molecules which trajectories intersect; Since *Link_trajectories* selects trajectories by the minimal spot distance, increasing ρ_{spot} should lead to an apparently smaller D corroborated by the results displayed in Fig. 8.14.

In order to gain the results, sequences of frames (100×100 pixel i.e. $10.8 \times 10.8\,\mu\mathrm{m}^2$) were generated by MONTE-CARLO-simulations containing the respective number of spots.

Two series of simulations were performed. In one series the number of spots remained constant over time, in a second series spots vanished at random, their number decreasing exponentially over time (simulating "photobleaching" of molecules). The bleaching time was set to $\tau_{PB} = 20$ frames according to experimental evaluations (see Fig. 8.12).

As in other simulations within this work, certain relevant hardware parameters (gain $g = 6.4\,\mathrm{e/count}$, read out noise $\sigma_{ro} = 5.3\,\mathrm{e}$, pixel size $\Delta x_{pix} = 107.5\,\mathrm{nm}$, exposure time $\Delta t_{exp} = 10\,\mathrm{ms}$, read out time $\Delta t_{ro} = 23\,\mathrm{ms}$, spot width $\Delta x_{spot} = 2.0\,\mathrm{pixel}$) and sample parameters (emission spot intensity $I_0 = 600\,\mathrm{count/s}$, diffusion constant $D_{simu} = 2.5\,\mu\mathrm{m}^2/\mathrm{s}$) were kept constant.

Different spot densities were chosen, $\rho_{spot} = 4 \times 10^{-4}\,\mathrm{spot/pixel}$ (1 spot/frame), $\rho_{spot} = 1\,[4] \times 10^{-3}\,\mathrm{spot/pixel}$ (10 [40] spots on a frame of 100×100 pixel).

Analysis of experimental data finds a mean initial spot density of $\rho_{spot} = 1 \times 10^{-3}$/pixel (see Fig. 8.12).

After simulating the image stacks, they were analyzed by the fitting algorithm described above: After the spots had been identified and fitted, the trajectories were extracted considering $L_{\max}$ and the step distance histograms were computed. Since for $D_{simu} = 2.5\,\mu\mathrm{m}^2/\mathrm{s}$ and $\Delta t_{lag,eff} = 29.7\,\mathrm{ms}$ the average step distance is

[14] The *Link_trajectories* routine itself and the role of L_{max} is discussed in Appendix 13.4

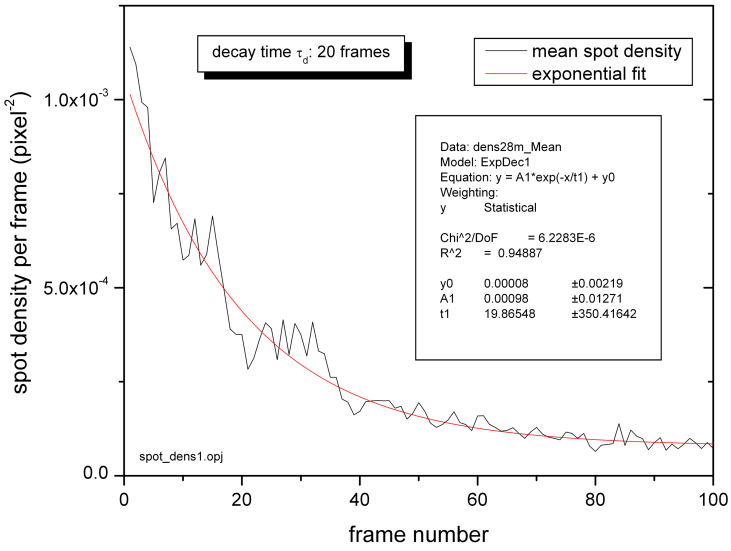

Figure 8.12.: Spot density as function of total illumination time $\Delta t_{exp,tot}$ (1686 spots included). The decay is due to photobleaching of the fluorophores. Fitting a single exponential yield an initial spot density $\rho_{spot,ini} = 1{\times}10^{-3}$/pixel and decay time $\tau_{PB} = 20$ frames, corresponding to $\tau_{PB} = 0.20\,\mathrm{s}$ (with $\Delta t_{exp} = 10\,\mathrm{ms}$).

$\bar{r_t} = 0.54\,\mu$m, D_{fit}/D_{simu} is determined for $L_{max} = 0.81\,\mu$m up to $5.4\,\mu$m. (The number of steps included into the histograms ranged from 1100 to more than 3000, depending on the specific ρ_{spot} and L_{max} and whether photobleaching was simulated or not.)

In Fig. 8.13, a typical step distance histogram is displayed which is based on, in this case, 100 frames of 100×100 pixel with $\rho_{spot} = 4 \times 10^{-3}$ spot/pixel, $L_{max} = 1.6\,\mu$m and 3057 steps. The fit according to Eqn. 9.1 yields $D_{fit} = 2.26 \pm 0.04\,\mu\mathrm{m}^2/\mathrm{s}$, $90 \pm 1\%$ of D_{simu}.

Fig. 8.14 (A) displays the results of the first series (no photobleaching present). For the experimentally relevant spot density of 1×10^{-3} spot/pixel (open inverted triangles) D_{fit}/D_{simu} shifts slightly from 0.92 to 0.95 by varying L_{max} from $0.81\,\mu$m to $5.4\,\mu$m. For $\rho_{spot} = 4 \times 10^{-3}$ spot/pixel (open circles), the change of D_{fit}/D_{simu} is more pronounced, from 0.81 to 1.06.

In case of photobleaching ($\tau_{PB} = 0.20\,\mathrm{s}$ Fig. 8.14 (B)), for $\rho_{spot} = 1{\times}10^{-3}$ spot/pixel (closed inverted triangles) D_{fit}/D_{simu} shifts from 0.95 to 0.97 in the same L_{max} range. However, for $\rho_{spot} = 4 \times 10^{-3}$ spot/pixel (closed circles) D_{fit}/D_{simu} rises from 0.90 to 1.11.

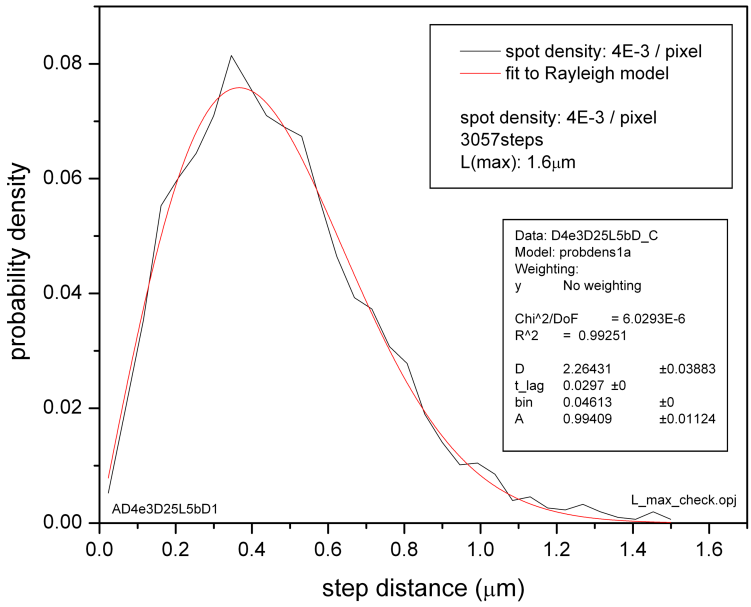

Figure 8.13.: Step density histograms from a simulated image sequence with $D_{simu} = 2.5\,\mu\mathrm{m}^2/\mathrm{s}$, $\rho_{spot} = 4 \times 10^{-3}\,\mathrm{spot/pixel}$ (40 spots per $100 \times 100\,\mathrm{pixel}$ frame, 50 frames in total). The step density distribution was fitted with Eqn. using the effective lag time $\Delta t_{lag,eff} = 29.7\,\mathrm{ms}$ to yield $D = 2.26 \pm 0.04 \mu m^2/s$ and a correction factor $D_{fit}/D_{simu} = 0.90 \pm 0.01$.

In Fig. 8.14 (A) and (B), in case of only one spot per frame (closed squares), no erroneous linking should occur ("negative control") and D_{fit}/D_{simu} should equal one, as can readily be observed.

For all D_{fit}/D_{simu} data points, the error bars (given as std.dev. of the mean values) were in the range from 0.02 to 0.04.

In summary, for all spot densities simulated Fig. 8.14 clearly shows a monotonic increase of D with increasing L_{max}. Under the conditions applied during the experiments (photobleaching time $\tau_{PB} = 0.20s$ initial spot density $\rho_{spot} = 1 \times 10^{-3}\,\mathrm{spot/pixel}$), we expect a correction factor $D_{\mathrm{app}}/D_{real} = 0.95$ between the apparent and the real diffusion constants, D_{real} and D_{app}, for a maximum step distance $L_{max} = 15\,\mathrm{pixel} = 1.6\,\mu\mathrm{m}$.

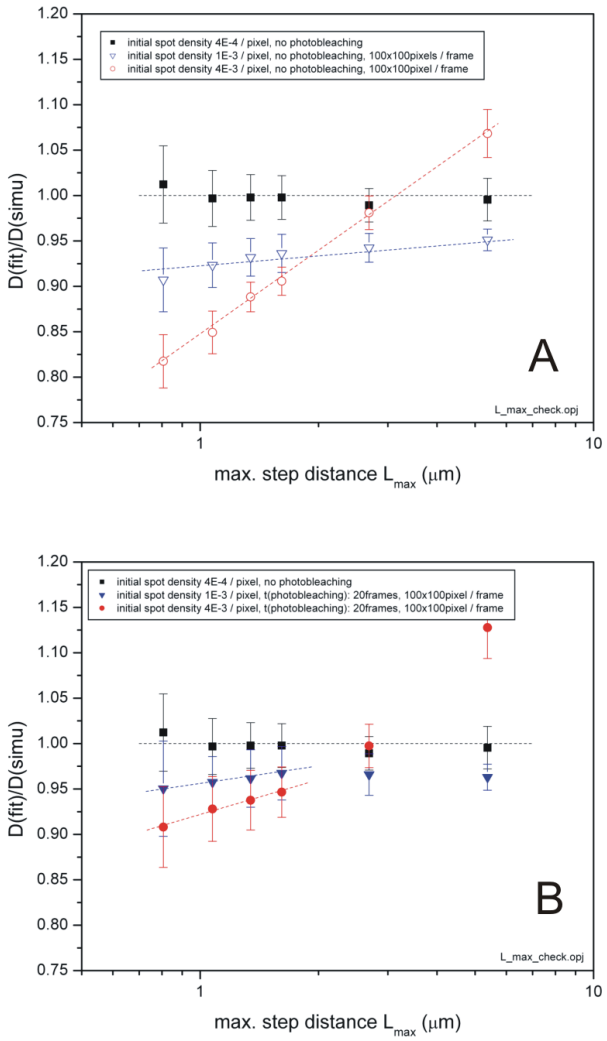

Figure 8.14.: Ratio of fitted and simulated diffusion constants, D_{fit} and D_{simu}, as function of the maximum step distance L_{max} (mandatory input parameter for *Link_trajectories*). Displayed are data for different spot density values ρ_{spot}. (A) No photobleaching is assumed ($\rho_{spot} = const$). (B) Photobleaching ($\tau_{PB} = 20\,\text{frames} = 0.20\,\text{s}$) is simulated.

9. Temperature-controlled determination of diffusion constant of lipid bilayer membrane

The artificial lipid membranes of giant unilamellar vesicles (GUVs) were prepared as described in section 7.1. The image sequences were acquired according to section 8.4.

In accordance to the analysis of the simulated image sequences in the preceding paragraph, the real movies were acquired with the same set of relevant hardware parameters (g, σ_{ro}, Δx_{pix}, Δt_{exp}, Δt_{ro}, Δx_{spot}) and processed with the same set of software parameters (Δx_{filt}, $\Delta x_{spot,fit}$, I_{th}) as above, given in Tab. 8.1. The temperature of the membrane system was equilibrated to either 22°C or 28°C.

The results are given in Fig. 9.1 (A) (22°C) and (B) (28°C) for $L_{max} = 15\,\text{pixel} = 1.6\,\mu\text{m}$. In ($A$) and ($B$) the step distance histograms are nicely approximated by the model, Eqn. 9.1. For the lower (higher) temperature, the fit yields $D_{22\text{C}} = 1.9 \pm 0.1\,\mu\text{m}^2/\text{s}$ ($D_{28\text{C}} = 3.2 \pm 0.1\,\mu\text{m}^2/\text{s}$). Applying the correction factor[1] $D_{app}/D_{real} = 0.95$ to the results, we get $D'_{22\text{C}} = 2.0 \pm 0.1\,\mu\text{m}^2/\text{s}$ and $D'_{28\text{C}} = 3.4 \pm 0.1\,\mu\text{m}^2/\text{s}$ as the diffusion coefficients of a GUV-membrane consisting of cholesterol : DLPC, 50 : 50 at 22°C and 28°C. (That means, a rise in membrane temperature from 22°C to 28°C causes an increase in D by ca. 70%.)

[1] for finite ρ_{spot}

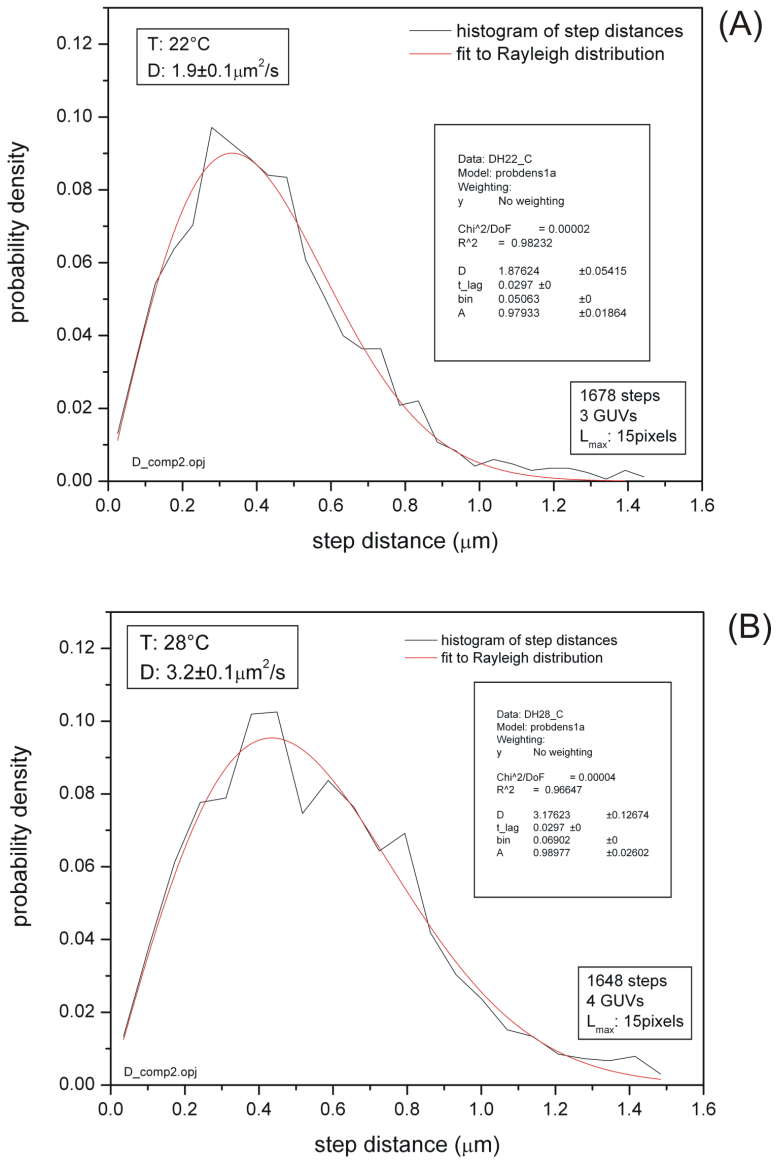

Figure 9.1.: Step density histograms from experimental measurements of fluorescent molecules diffusing within lipid bilayer membrane of GUVs (Cholesterol : DLPC, 50 : 50) at 22°C (A) and 28°C (B). The step density distribution was fitted with Eqn. using the effective lag time $\Delta t_{lag,eff} = 29.7\,\mathrm{ms}$ to yield $D_{22\mathrm{C}} = 1.9 \pm 0.1\,\mu\mathrm{m}^2/\mathrm{s}$ (A) and $D_{28\mathrm{C}} = 3.2 \pm 0.1\,\mu\mathrm{m}^2/\mathrm{s}$ (B). Applying the correction for finite spot density leads to $D'_{22\mathrm{C}} = 2.0 \pm 0.1\,\mu\mathrm{m}^2/\mathrm{s}$ and $D'_{28\mathrm{C}} = 3.4 \pm 0.1\,\mu\mathrm{m}^2/\mathrm{s}$ (see text).

10. Photoinduced conversion and bleaching behavior of the fluorescent protein Kaede-GFP

In this chapter, the results of the single molecule investigations on the photobleaching, long term blinking and photoswitching behavior of the fluorescent protein *Kaede*-GFP are presented. Contrary to bulk (ensemble) experiments which usually can not reveal the behavior of subpopulations or subspecies of biomolecules, the statistical analysis of single molecule intensity trajectories allowed us to characterize the diverse emission dynamics of both *Kaede*-GFP forms.

The trajectories were obtained by automated detection ("segmentation") and fitting ("feature extraction") of the spots within each frame of an image sequence.

The photobleaching of single *grKaede* molecules was analyzed by determining the number of fluorescent spots and the sum of their intensities as function of time upon illumination at 488 nm.

Additionally, the photoswitching behavior was accessed by applying a single violet light pulse ($\lambda = 405\,\mathrm{nm}$) to the sample by simultaneous monitoring of the fluorescence emission in the green and red channels before and after the violet light pulse.

10.1. Image processing

The fluorescence images of immobilized single *Kaede*-GFP molecules were in principle processed similarly to the image sequences of DiI-C_{18} molecules diffusing in lipid membranes (see chapter 6).

Certain differences in the image processing shall be described briefly:

- Contrary to the 1-color emission experiment (GUVs), the *Kaede*-GFP experiment required the separation of two spectral channels.

- Due to the higher sensitivity of *Kaede*-GFP to photobleaching, excitation intensities were decreased ($< 1\,\mathrm{kW/cm^2}$) and exposure times Δt_{exp} (for the photoconversion experiments) extended (see sections 10.2 and 10.3).

- Due to the presence of fluorescence background and the broader distribution of emission intensities, the intensity threshold I_{th} for detecting spots was increased to 3 count (DiI-C_{18} in GUVs: 1.5 count).

- Additionally, since the spots were immobilized, no spatial tracking was needed. To the contrary, if a spot was detected at a given position (x, y) in any frame, the spot was "fitted" (i.e., its refined position and intensity determined) at this position for all other frames, too. This includes frames in which the spot was "dark", bleached or had converted to another spectral form (green to red or vice versa).

  However, if for a specific spot only the frames in which the spot was detected are considered, the position of the spot does not vary more than $\Delta x_{spot} \pm 1\,\text{pixel}$ over the whole image stack[1].

  This procedure allowed for a direct comparison between the two spectral channels on a frame-to-frame base.

The procedure outlined provides a reliable recognition and description of the spots, as is evident from the reconstructed image and the residuals between the original and the reconstructed images (Fig. 10.1). All significant spots could be found and fitted automatically by supplying the algorithm with a user-defined detection threshold I_{th}.

During the analysis, a constant spot std.dev. $\sigma_{spot} = 1.2\,\text{pixel}$ was used as determined by the PSF measured on sub-resolution size fluorescent beads (see also section 5.3, Fig. 5.7). (As was found empirically, on the one hand, a fixed σ_{spot} does speed up fitting and, on the other hand, for example, prohibits "freak" fits of unrealistic fitted intensity values. The specific value of σ_{spot} is neither crucial for the (relative) spot intensity nor for the (absolute) position determination which is not relevant in this experiment.)

Spots having the same positions over the whole set of the images in both spectral channels were linked through the image stack resulting in a set of intensity trajectories in both spectral channels.

In the following, two different experiments shall be presented and discussed, investigating the photobleaching (by 488 nm light) and photophysical reactions upon illumination with 405 nm.

10.2. Photobleaching induced by 488 nm light

In order to acquire information about the fluorescent properties of a molecule, generally (optical) excitation with subsequent detection of the emitted radiation

[1] The reason why spots move at all can be found in a finite size of the gel pores: They have to be large enough to allow for the complete functionality of the protein while confine it at the same time to a specific location.

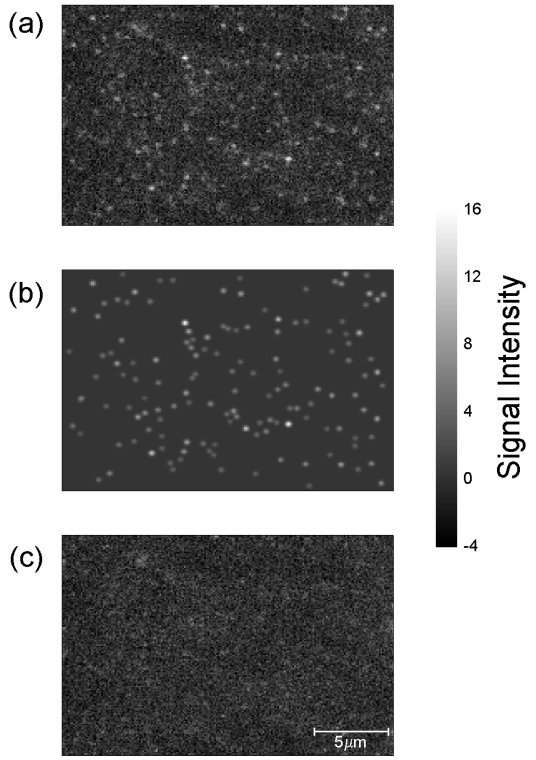

Figure 10.1.: Fluorescence microscopy image (150×200 pixel) frame of single *Kaede*-GFP molecules immobilized in PAA gel. Shown is fluorescence emission in the "green" spectral channel under laser excitation at $\lambda_{exc} = 488\,\mathrm{nm}$. ($I_{exc} = 3 \pm 0.3\,\mathrm{kW/cm^2}$, $\Delta t_{exp} = 10\,\mathrm{ms}$). ($a$) raw image (original image with constant background removed); (b) fit and (c) residuals. (signal intensity is given in count.)

is involved. Besides the direct radiative decay into the (singlet) ground state (typically within less than 100 ns), there are also non-radiative ways of leaving the excited state including a possible conversion to a long lived "dark" state from which non-radiative decay to the ground state can occur.

After a finite number of absorption-emission cycles, the fluorophore finally degrades ("bleaches") by an irreversible chemical reaction and loses its ability to fluoresce. In the case of *grKaede*, the intensity of the green fluorescence decreases slowly due to bleaching (by illumination with 488 nm light) as well as photoconversion (induced by violet light). Since the illumination intensity at 488 nm could not be decreased below a certain value due to limitations in the signal-to-noise ratio in the detected fluorescence signal, an accurate analysis of the photoconversion process requires a careful characterization of the bleaching behavior.

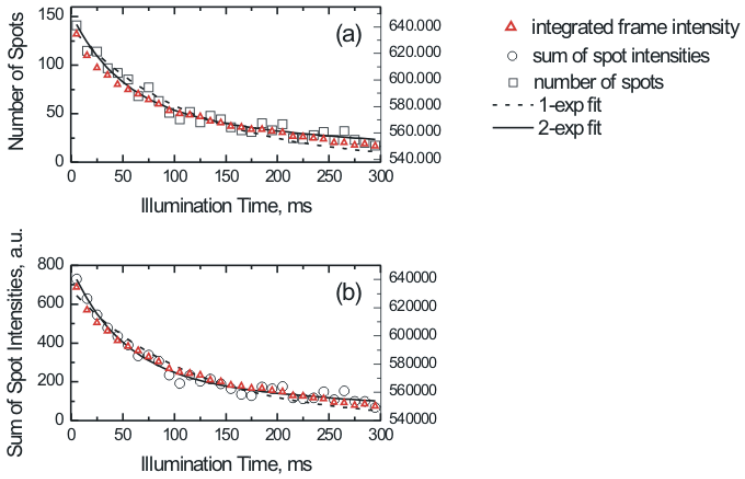

Figure 10.2.: Photobleaching kinetics of PAA gel-immobilized *Kaede*-GFP protein molecules: (*a*) number of spots detected in the image of (open squares) and (*b*) sum of spot intensities (open circles) as a function of the illumination time. Also shown are the integrated frame intensities (red triangles) and the single-exponential (dashed curves) and biexponential fits (solid curves). $\lambda_{exc} = 488\,\text{nm}$; $I_{exc} = 3 \pm 0.3\,\text{kW/cm}^2$ [84].

To characterize the photobleaching behavior, the fluorescence emission of *grKaede* molecules was recorded as function of illumination time under conditions where no photoconversion was expected (diode laser blocked). 30 frames of 200×200 pixel images were acquired during illumination of the samples by 10 ms pulses at 488 nm. Excitation intensity was set to $3 \pm 0.3\,\text{kW/cm}^2$. After acquiring an image during a single 10 ms excitation pulse, each frame was transferred (read out) from the CCD to the computer within 50 ms. During this time (read-out time) no exposure of the sample to light took place. Each image obtained was analyzed as described above.

The number of *grKaede* spots found in the corresponding frames and the sum of the spot intensities are displayed as a function of illumination time with 488 nm light in Fig. 10.2 (*a*) and (*b*), respectively. As can be seen, the detected number of spots, the sum of their intensities and the integrated pixel intensity per frame decreases with increasing duration of illumination. These decays within the error limits follow the same dependence. Indeed, a least-squares-fit with a single-exponential decay model yielded the decay times of 132 ms and 116 ms for the number of molecules and their intensity, respectively. However, a much better fit can be obtained with a biexponential model:

$$X(t) = X(0) \cdot (\alpha \exp(-t/\tau_1) + (1-\alpha)\exp(-t/\tau_2)) \tag{10.1}$$

where $X(t)$ is either the number of spots in the ROI or their integral intensity. The biexponential model gives $\alpha \approx 0.32$, $\tau_1 \approx 0.06\,\mathrm{s}$ and $\tau_2 \approx 0.38\,\mathrm{s}$ for the number of spots and $\alpha \approx 0.31$, $\tau_1 \approx 0.05\,\mathrm{s}$ and $\tau_2 \approx 0.35\,\mathrm{s}$ for the sum of spot intensities.

Two conclusions can be drawn from these observations:

- First, while in general the decay of the number of spots as well as the sum of intensities over illumination time is not surprising, the similarity of the decay rates shows that the photobleaching probability is virtually independent of the spot intensity.
- Second, the non-monoexponential decay of the number of spots and their integral intensity might suggest the existence of at least two *grKaede* subspecies affected by photobleaching in a different way. (Since the fluorescent background was carefully removed during the image processing, its contribution can be excluded as reason for the non-single-exponential intensity decay.)

Apart from heterogeneities in the microenvironment of the molecules within the PAA gel (as observed for PVA gels [35]), photophysical reasons specific for the *Kaede*-GFP protein and other GFP-mutants [22, 49, 73, 3] could explain the presence of at least two fractions of protein molecules corresponding to 2 decay times of ca. 50 ms and ca. 350 ms. The fast decaying fraction could be attributed to a type of molecules that are converted by the 488 nm excitation light into a dark state similar to Dronpa [35]. The slower decaying species eventually bleach irreversibly into a non fluorescent dark state without previous conversion.

Negative controls with samples prepared as described above in which the protein solution was substituted by buffer solution showed a low fluorescent background constant over time. In particular, background fluorescence was the same before and after 405 nm illumination.

10.3. Reaction pathways induced by 405 nm light

After analyzing the photobleaching of the *grKaede* molecules by the 488 nm irradiation a series of photoconversion experiments was carried out. By imaging the corresponding fluorescence signal of single protein molecules in the red and green channels as a function of time, the temporal conversion behavior of *grKaede* to *rKaede* was determined.

In Fig. 10.3 the setup is displayed during four specific states of the experiment, with a focus on changes occurring over the measurement time in the sample (enlarged circle):

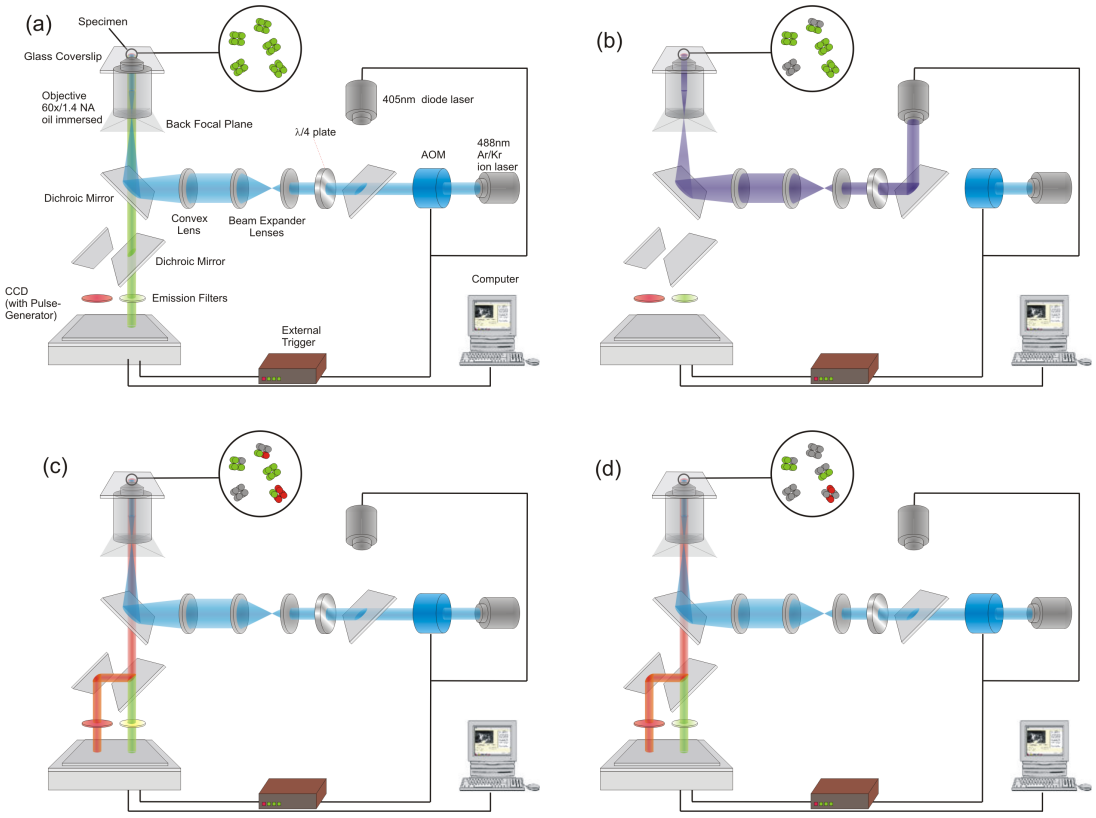

Figure 10.3.: Experimental setup as used for photophysical investigations of the *Kaede*-GFP. Two colors were used for excitation of the sample, the emission signal was split spectrally into two differently colored channels and focussed on the CCD camera.

(a) In a first step, the sample was usually exposed to four 488 nm-pulses, to identify the positions of the molecules and check for a change in emission behavior ($I_{exc} = 0.6 \pm 0.06\,\mathrm{kW/cm^2}$ for $\Delta t_{exp} = 50\,\mathrm{ms}$; read-out time for each image (illumination blocked): $\Delta t_{ro} = 100\,\mathrm{ms}$) . (The *Kaede*-GFP molecules are in their native (*green*) state, the excitation with 488 nm (blue) light leads to the emission of green fluorescence.)

(b) In a second step, the sample was illuminated with a flash of 405 nm (violet) light for 100 ms ($I_{exc} = 0.3 \pm 0.3\,\mathrm{kW/cm^2}$) while the CCD was not detecting. (Some molecules (*gray*) had turned – temporarily or permanently – photophysically inactive.)

(c) Directly following the violet pulse, the sample was excited by 488 nm light again. Some *Kaede*-GFP molecules exhibit green, some red fluorescence,

some are bleached.

(d) During the exposure to blue light, bleaching of the green and red molecules occurs.

Except when exposed to violet light, the protein emission was recorded for every frame in both channels.

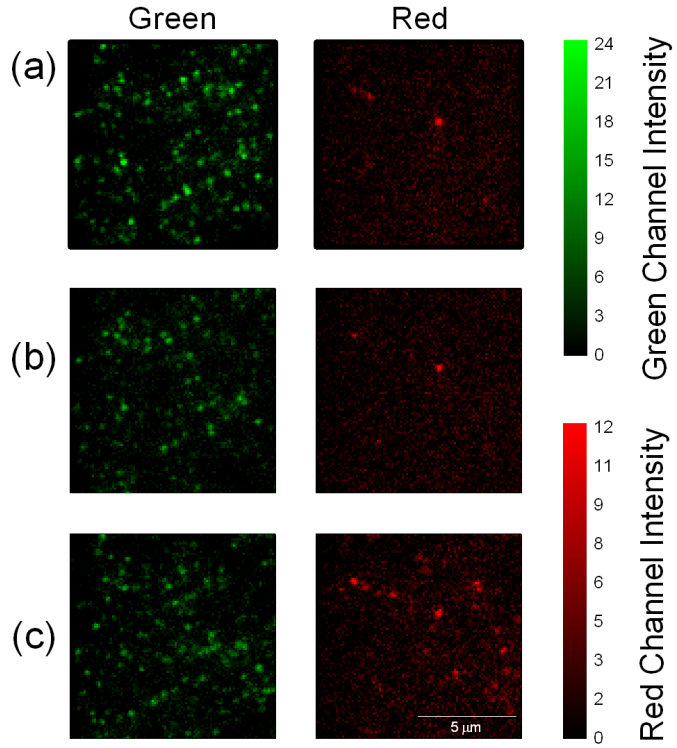

Figure 10.4.: Observation of the photoconversion and photobleaching of single *Kaede*-GFP protein molecules immobilized in PAA gel. Unfiltered background-corrected images (a), (b) and (c) correspond to frames #1, #4 and #5. Images are acquired with excitation at 488 nm ($0.6 \pm 0.06\,\mathrm{kW/cm^2}$, exposure time $\Delta t_{exp} = 50\,\mathrm{ms}$). The violet light pulse (405 nm, $0.3 \pm 0.03\,\mathrm{kW/cm^2}$, $\Delta t_{exp} = 100\,\mathrm{ms}$) was applied between frames #4 (b) and #5 (c) [84].

Unfiltered fluorescence images for a typical experiment of this type (background level subtracted) are displayed in Fig. 10.4. Frames #1, #4 and #5 are shown in Fig. 10.4 (a) to (c), respectively.

Inspection of the images shows that first, much fewer spots are visible in the red than in the green channel for all frames. This behavior is indeed expected for Fig. 10.4 (*a*) and (*b*) due to the absence of violet light during and before image acquisition for the frames #1 to #4. (The spots present in the red channel in Fig. 10.4 (*a*) and (*b*) had obviously converted before the triggering light pulse was applied.)

Second, in both channels a moderate decrease in the number of spots is visible between the upper two pairs of images, reflecting photobleaching from frame #1 to #4. However, after illumination with 405 nm light between frame #4 and #5, a strong increase in the spot number can be seen in both channels. In addition to the expected green-to-red conversion leading to an increase in the number of "red" (and lowering the number of "green") emitting molecules, a large number of previously non-fluorescing molecules appears in the green channel (Fig. 10.4 (*c*)). Since the absorbance of *rKaede* at 488 nm is roughly half as high as for *grKaede*, the ratio of the emission intensities should be expected to be similar. Thus, in Figs. 10.4 and 10.5, the color bars in the red and green channels scale 1:2.

This activation of non-fluorescent molecules to green emission by radiation around 400 nm had been previously observed in the case of GFP and its mutants [49, 35]. Surprising to us was the high amount of activated green compared to green-to-red photoconverted *Kaede*-GFP which was quantified in a further step below.

It should be mentioned that the green-to-red conversion process, as well as the non-fluorescent-to-green activation is completed within frame #5. An image analysis has shown that no new spots appear in the frames #6 to #8 which were not present already in frame #5 (data not shown). The images shown in Fig. 10.4 represent a quarter of the area that was subjected to a statistical analysis of spot behavior, as discussed in what follows.

To quantify the conversion and activation processes, the full frames #1 to #8 (200×190 pixel) were analyzed as described above. For each spot detected in any frame, the x- and y-positions and the intensity were determined in all eight frames in both channels. The resulting intensity trajectories were sorted into 16 different groups, depending on whether spots were active in the first and/or last four frames in the red and/or green channels (see Appendix 13.3). For each trace in both channels, the mean intensities in frames #1 to #8 were compared to an empirical threshold value to determine whether the particular spot is on average "active" or "inactive" in the specific channels. The threshold value was chosen to be the same for both channels because it was largely determined by the variance of the read-out noise of the CCD camera which is independent of the spectral range.

A spot had to show activity at least in one of the spectral channels in order to be included in the analysis at all. If the spot is "active", the ratio between the

mean intensities for the frames #1 to #4 and #5 to #8 was compared against the second threshold estimated based on the bleaching experiments described above determining if photoinduced switching occurs.

Depending on the ratio of the mean intensities in frames #1...#4 and #5...#8, the intensity trajectories in each of the channels can be classified into the classes "on/on", "on/off", "off/on" and "off/off". With this notation, for example, the expression "green on/off" refers to a spot in the green channel being on average "on" during the frames #1...#4, and on average "off" during the frames #5...#8.

Combination of the classes for the green and the red channels yields 16 groups in which the trajectories were sorted. Although 16 possible combinations of green/red emission characteristics existed, 90% of all the traces belonged to only one of four categories.

Upon sorting, the spots were reconstructed as noise-free images and concatenated. Altogether 534 different single molecule traces were detected and analyzed. To show the typical dynamics of spots, 15 representative traces are displayed in Fig. 10.5 (a) – (d) for each group. As in Fig. 10.4, in each plot the spots' intensities are presented in two blocks, for the green and red channels.

Fig. 10.5 (a) shows 15 trajectories grouped by the property "green on/off", "red off/on". In total, 22 of 534 trajectories (4%) were classified for this group. All traces display a strong increase in red fluorescence after being illuminated with violet light (after frame #4); Simultaneously, in all traces the green signal is substantially reduced from frame #5 on. At the same time, notice that several of the molecules show some red emission even before the activation by the violet pulse (e.g., spot #9). On the other hand, one can observe some molecules still showing some green emission after the exposure to the violet light (spots #1, #7, and #13). For spot #1, quantitative comparison of the intensities shows that the decrease in green matches well with the increase in red fluorescence suggesting that spot #1 consists of a cluster of at least 2 active fluorophores. Spot #7 shows a brief re-activation of green fluorescence in frame #5 while exhibiting red fluorescence in frames #5 to #8. This could be explained by transient reactivation from a "dark" state to the intensity comparable with that of frame #1 and a subsequent switching to the red *Kaede* form. Spot #9 shows conversion already in frame #2 which might have potentially been activated by 488 nm light. Although this seems rather unlikely, it is still possible taking into account the absorption spectrum of other protonated GFP mutants: the protonated molecule is supposed to have the maximum absorption at ~ 400 nm. Therefore, 405 nm can efficiently trigger the green-to-red conversion [13, 3, 62]. However, the protonated molecule also exhibits (weak) absorption at higher wavelengths, e.g., 488 nm. A slight decrease in the *rKaede* emission intensity in the red channel in frames #5 to #8 can be seen in

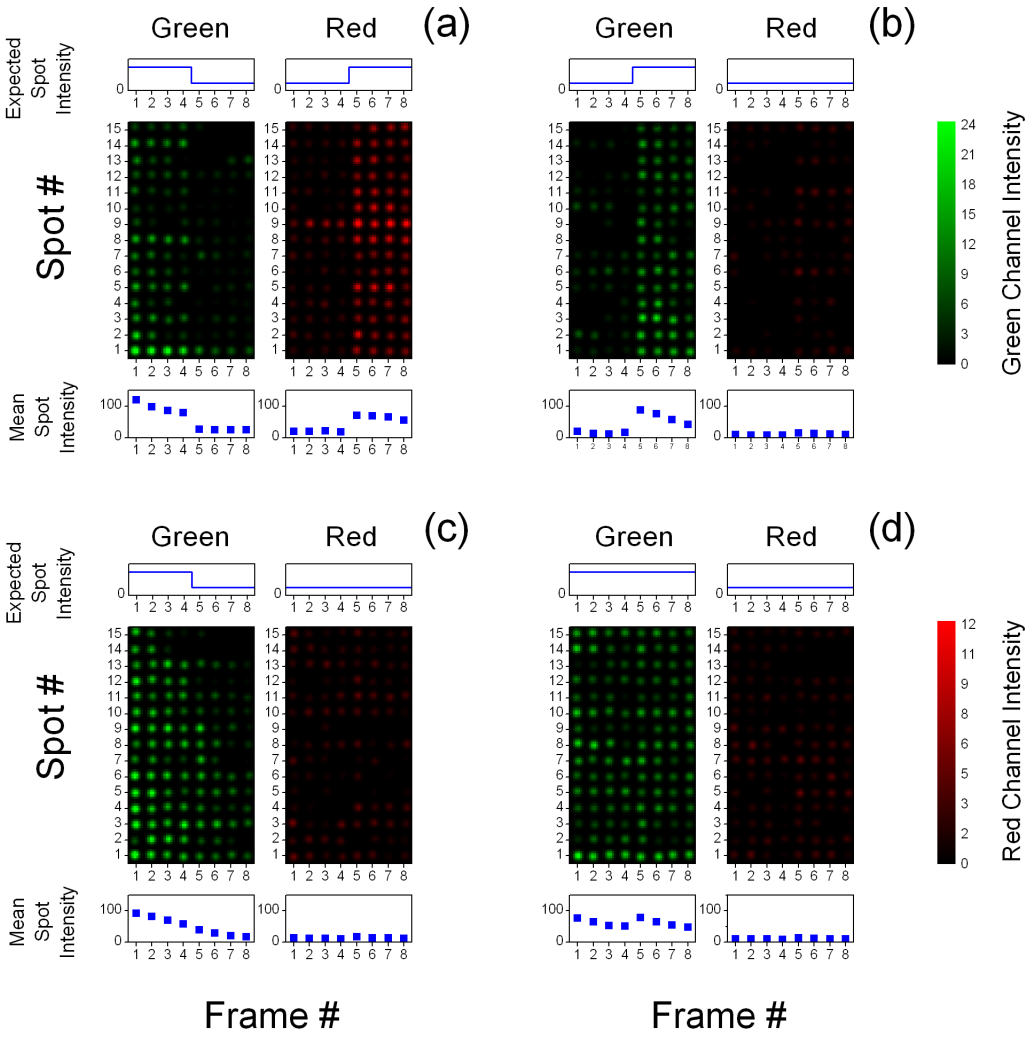

Figure 10.5.: Reconstructed time sequences of single *Kaede*-GFP molecule images in green and red spectral channels for four most significant groups classified according to their fluorescence dynamics pattern. Fifteen representative traces are displayed for each group. Schematic representations of the group-specific type of fluorescence dynamics are shown on top of each panel (solid lines). The actual dynamics of the mean spot intensity for each of the groups is shown at the bottom of each panel (squares). In total, 534 intensity traces were analyzed. (*a*) Group demonstrating green-to-red photoswitching (22 intensity traces (4%) were detected); (*b*) Group exhibiting photoactivation of the green emission with no red emission observed (70 intensity traces (13%) were detected); (*c*) Group demonstrating photoinduced deactivation of green emission with no red emission observed (230 intensity traces (43%) were detected); (*d*) Group showing partial photoinduced revival of green emission with no red emission observed (160 intensity traces (30%) were detected).

Fig. 10.5 (*a*), lower panel, which is indicative of photobleaching of *rKaede* by 488 nm light.

Besides the green-to-red photoswitching behaviour of the *Kaede*-GFP molecules a substantial amount of the detected *Kaede*-GFP molecules showed activation in the green channel upon illumination by 405 nm light (Fig. 10.5 (*b*)). 70 of 534 traces (13%) were sorted as "green off/on", "red off/off".Intensity in the red channel was dim through the entire eight frames (slight intensity increase in the red channel in frames #5 to #8 can be attributed to spectral crosstalk from the green channel.) Activation of green fluorescence from a non-fluorescent state seems to be a common feature among GFP mutants as observed before [49]. In case of the fluorescent protein Dronpa [35], a high degree of reversibility exists. As traces #2, #6, and #10 show, re-activation in the green channel occurs upon previous dimming of the spots in frames #4 and #5. Whether a reversibility (as in case of Dronpa) exists also for *Kaede*-GFP, further investigations will show.

The trajectories displayed in Fig. 10.5 (*c*) belong to the large group "green on/off", "red off/off". 230 of the 534 trajectories (43%) were sorted into this subset. The spots collected here display a decrease in the green emission after the 405 nm illumination, stronger than on average expected from photobleaching with 488 nm and might be considered as a partial photodeactivation of the green emission. The signal in the red channel remains dim with weak fluctuations around the mean intensity. The partial photodeactivation of green fluorescence observed in this case can be tentatively attributed to irreversible photobleaching of a fraction of *Kaede*-GFP molecules by the violet light pulse. (A specific investigation of the photobleaching of *grKaede* by 405 nm light was outside the scope of the present study.)

Fig. 10.5 (*d*) shows the group of spots which the sorting algorithm regarded as "green on/on", "red off/off". The group consisted of 160 traces (30 % of the total number of traces). As can be seen, the spots exhibit a continuous emission pattern in the green channel interrupted occasionally by transient blinking in one or two frames. Green fluorescence is not bleached by probe light within the observation time used here. However, the 405 nm light pulse leads to a slight revival of the intensity in the green and/or the red channels. Red channel fluorescence is always dim in this group. Partial revival of green emission observed in Fig. 10.5 (*d*) pose interesting questions about the nature of these phenomena (red-to-green conversion upon transient increase in green fluorescence?), however, a more detailed investigation is necessary to clarify this behavior.

It should be noted that only very few events which showed emission in the green and red channels simultaneously were observed. They were not included into the analysis due to the lack of statistical significance.

Under the experimental conditions a green-to-red conversion ratio was repro-

ducibly obtained which is significantly below the ratio which can be expected according to bulk measurements in aqueous solution performed before by Ando et al. [3]. Additionally, an increase in green fluorescence upon illumination with violet light was found consistent to observations on GFP and related fluorescent proteins [22, 49, 73, 87, 35] but contrary to what was previously published [3].

In detail, in the experiments 405 nm light was applied in a dose of 15 J/cm^2 which is comparable to the dose (ten pulses à 1.3 J/cm^2) used by Ando et al. [3]. Of 534 spots analyzed, 22 (4%) showed a significant increase in the red spectral channel upon illumination with violet light while becoming dim in the green channel. Likewise, 70 (13%) spots significantly increased their emission intensity in the green spectral region without showing red emission.

In comparison, Ando et al. obtained a decrease in bulk fluorescence in the green channel by ca. 75% and a $\sim$ 30-fold increase in the red channel ([3], Fig. 5 C) employing similar spectral emission filters. However, while a 488 nm laser light was used to excite both the green and the red forms of *Kaede*-GFP, Ando et al. used blue (475 ± 10 nm) and yellow-green (550 ± 15 nm) Xe-lamp light for excitation of *grKaede* and *rKaede*, respectively. These differences in the spectral excitation range probably cause an increase in the absolute value of fluorescence in the red channel compared to the experiment performed in this thesis. However, it cannot account for the relative changes in red fluorescence intensity (factor 1.5 (here) vs. 63 [3]). Additionally, the differences in the spectral regions of the excitation and/or emission channels between the two works also cannot explain why an increase in green emission was observed contrary to the decrease obtained by Ando et al..

One potential reason for the discrepancies in the results observed could be differences in the chemical environment of the single molecules in the present experiment as compared to an aqueous solution. As suggested in ([35]; supplemental material), this could give rise to a changed photophysical behaviour. Another explanation could be based on structural and/or conformational changes of the protein itself potentially induced by the gel mixture and/or the polymerization reaction. However, since the protein was not expressed in-house, it cannot be excluded that the respective changes had already occurred prior to the polymerization reaction.

11. Summary

In this work, a fluorescence imaging technique based on a wide field microscope was developed which is capable of identifying, characterizing and tracking the fluorescence emission originating from single molecules in biological systems.

To that end, the technical setup had to be designed, implemented and finally adapted to the sample systems in order to yield an optimal image quality and to maximize the signal-to-noise ratio (SNR).

For quantitative analysis, the physical properties of the optical setup had to be characterized and calibrated.

In a second step, representative biological model systems – giant unilamellar vesicles (GUVs) and fluorescent proteins (*Kaede*-GFP) immobilized in a gel – had to be developed and standardized.

Image sequences had to be acquired, showing the fluorescence emission of either single fluorophores diffusing within the lipid membrane of a GUV or single immobilized fluorescent protein molecules. The image sequences exhibited a generally low SNR combined with a medium to high density of spots. On the one hand, this prevented the application of conventional (commercial) image analysis software.

On the other hand, manual selection of the fluorescent spots was excluded on grounds of efficiency and significant subjective bias.

Therefore, in a third step, an automated image analysis algorithm was designed, implemented, tested and debugged. It was characterized physically and the image sequences of the model systems were analyzed in a reliable and repeatable way.

Thus, for the *Kaede*-GFP molecules photobleaching and photoswitching behavior could be statistically characterized.

In case of the lipid bilayer system investigated, the diffusion constant could be determined with a high precision and accuracy for two different measurement temperatures.

12. Conclusions and outlook

In conclusion, establishing a reliable automated analysis procedure for single molecule fluorescence images proved, somewhat unexpected, to be the most demanding part of the thesis. This was due to some simple fact, the excellence of the human eye:

Even the "naked eyes" of a non-expert usually "understand" what is going on in typical, relatively noisy image sequences showing the fluorescence of single molecules: Blurred spots are moving around, appearing and disappearing here and there. However, even nowadays computers do not contain a built-in neuronal network adapted to segment, characterize and trace moving objects out of a numerical 3D-array. In other words, it generally requires a lot of (human) intelligent input to teach a computer the art of visual interpretation of data, i.e., to "see".

Therefore, in all image analysis procedures, it is crucial to validate the algorithm, whether it is performed by a human being or a computer.

In the first case, *subjective preferences* can bias the results, in the latter case, however, due to the highly non-linear compression of the 3D-pixel intensity data of an image sequence into, e.g., the diffusion constant as a single scalar, *hidden bugs and artifacts* easily can lead to wrong results and conclusions.

Thus, this study is understood as a contribution to a systematic and automated analysis approach for single molecule fluorescence imaging.

13. Appendix

13.1. Conversion processes

The number of fluorescence photons $N^{ph}(t) = I^{ph}(t)\Delta t$ follows the Poissonian distribution [96]. The probability to detect n photons within Δt under the condition of a mean photon number N^{ph} is given by:

$$P\left(N^{ph}(t) = n\right) = \frac{\left(N^{ph}\right)^n}{n!} \exp\left(-N^{ph}\right) \tag{13.1}$$

Since for this distribution the variance equals the mean,

$$\frac{N^{ph}}{\mathrm{ph}} = \left(\frac{\sigma_N^{ph}}{\mathrm{ph}}\right)^2 . \tag{13.2}$$

Therefore, with Eqn. 3.14 follows:

Photon-to-electron conversion:

$$\begin{aligned} \frac{N^e}{\mathrm{e}} &\overset{(3.14)}{=} \frac{\eta N^{ph}}{\mathrm{e}} \overset{(13.2)}{=} \frac{\eta\,\mathrm{ph}}{\mathrm{e}} \left(\frac{\sigma_N^{ph}}{\mathrm{ph}}\right)^2 \\ &= \frac{1}{\mathrm{e}^2} \left(\sqrt{\frac{\eta\,\mathrm{e}}{\mathrm{ph}}}\,\sigma_N^{ph}\right)^2 \\ &= \left(\frac{\sigma_N^e}{\mathrm{e}}\right)^2 \end{aligned} \tag{13.3}$$

with

$$\sigma_N^e := \sqrt{\frac{\eta\,\mathrm{e}}{\mathrm{ph}}}\,\sigma_N^{ph} . \tag{13.4}$$

Electron-to-counts conversion:

$$\begin{aligned} \frac{N^c}{\mathrm{count}} &\overset{(3.14)}{=} \frac{N^e}{g\cdot\mathrm{count}} = \frac{\mathrm{e}}{g\cdot\mathrm{count}}\frac{N^e}{\mathrm{e}} \\ &\overset{(13.3)}{=} \frac{\mathrm{e}}{g\cdot\mathrm{count}} \left(\frac{\sigma_N^e}{\mathrm{e}}\right)^2 \overset{(13.6)}{=} \frac{\mathrm{e}}{g\cdot\mathrm{count}} \left(\frac{g\cdot\sigma_N^c}{\mathrm{e}}\right)^2 \\ &= \frac{g\cdot\mathrm{count}}{\mathrm{e}} \left(\frac{\sigma_N^c}{\mathrm{count}}\right)^2 \end{aligned} \tag{13.5}$$

with

$$\sigma_N^c := g^{-1}\,\sigma_N^e. \tag{13.6}$$

Photon-to-counts conversion:
Therefore:

$$\sigma_N^c := g^{-1}\sqrt{\frac{\eta\,\mathrm{e}}{\mathrm{ph}}}\,\sigma_N^{ph}. \tag{13.7}$$

13.2. Thermal effects

13.2.1. Absorption of ITO coverslips

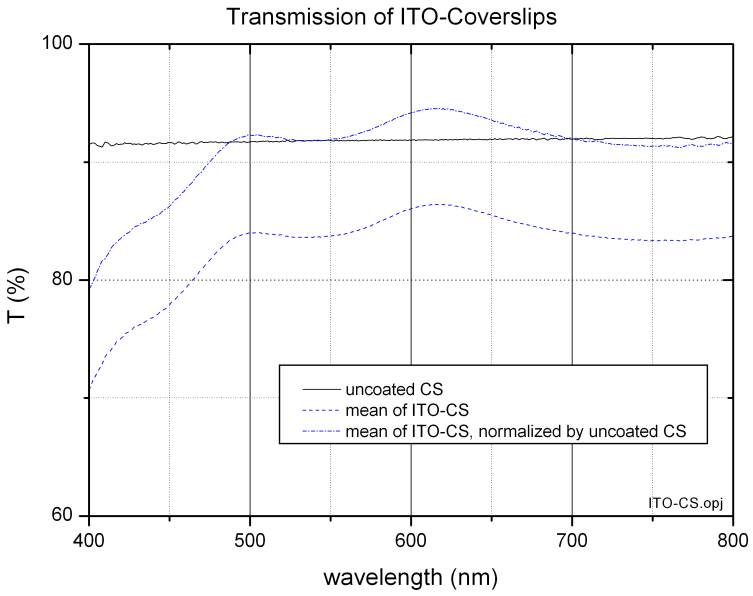

Figure 13.1.: Transmission spectra for standard uncoated (*solid black*) and Indium-Tin-Oxide (ITO)-coated coverslips (before (*dash blue*) and after (*dash-dotted blue*) correction for reflection). Mean of a set of eight ITO-coverslips is displayed. The absorption at $500 \pm 20\,\mathrm{nm}$ is $A < 8\%$ which is the upper limit for A because the refraction index of ITO $n_{ITO} \approx 2.0$ and, therefore, the reflectivity is higher than that of glass.

13.2.2. Numerical simulations

The numerical simulations of the 1D heat dissipation process from the heat absorbed in the ITO layer diffusing into the water above the coverslip were conducted

as follows: First, the whole measurement process was separated into a sequence of 50 steps, each having a duration of $\Delta t_{lag} = 33\,\text{ms}$ (Total time of simulation: $1.65\,\text{s} = 50 \times 33$). Each step consisted of

- an *exposure* period lasting $\Delta t_{exp} = 10\,\text{ms}$ during which heat was added to the system linearly with time t, at the position of the ITO-layer ($z = 0$).
- a subsequent *read out* period ($\Delta t_{ro} = 23\,\text{ms}$), during which no heat is added.

In the simulation, both parts of the 50 steps are further subdivided into substeps of $\Delta t_{sub} = 0.5\,\text{ms}$ to approximate the heat *absorption* and *diffusion* process.

This is done in the following way:

During an exposure period, at the beginning of each substep the heat absorbed during Δt_{sub} ("*heat quantum*") is added to the system and the diffusion of this heat quantum is computed for $t \in [0, \Delta t_{sub}]$. In addition, applying the superposition principle, the diffusion is computed for all heat quanta which were *previously* added to the system and which diffuse *independently*.

On the other hand, during the read out period, no heat is added at the beginning of each substep. Only the diffusion processes for the already absorbed heat quanta are computed.

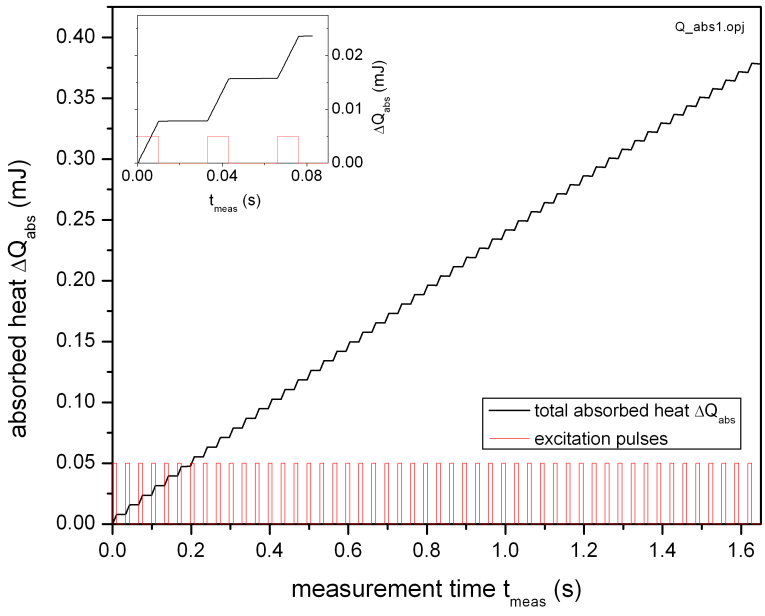

Figure 13.2.: Simulation of total heat absorbed ΔQ_{abs} over the acquisition time t_{meas} needed to collect 50 frames ($\Delta t_{exp} = 10\,\text{ms}$, $\Delta t_{ro} = 23\,\text{ms}$). Numerical simulations performed with time step width $\Delta t_{step} = 0.5\,\text{ms}$.

The spatial step with for the computation of $\Delta T(z,t)$ was $\Delta z_{step} = 1.0\,\mu$m, $z \in [0, 10^3\,\mu\text{m}]$.

As can be seen in the simulation of the temperature change in Fig. 6.2 (p. 80), for $z = 50\,\mu$m, the individual exposure periods can clearly be distinguished from the read out periods because the heat quanta added during the exposure cause an increase in temperature which is levelled of during the image read out (when no light is absorbed).

However, for $z = 200\,\mu$m the "ripples" on $\Delta T(z = 200\,\mu\text{m}, t)$ are not recognizable any more, due to the averaging effect of the increasing distance from the coverslip.

In Fig. 13.2 the total heat absorbed

$$\Delta Q_{abs,tot} = \int_0^{z_{max}} \rho_w\, c_w\, \Delta T(z,t)\; dz, \qquad z_{max} = 10^3\,\mu\text{m} \tag{13.8}$$

is given to check for consistency of the simulations. As expected, $\Delta Q_{abs,tot}$ increases linearly with time during periods of light exposure while it stays constant during frame read out. In addition, the heat absorbed during one exposure period amounts to $\approx 0.008\,$mJ which is consistent with the expected value of

$$\begin{aligned} \Delta Q_{abs,exp} &= P_{exc}\,\Delta t_{exp}\,\rho_{abs}\,f_{dist} && (13.9)\\ &= 30\,\text{mW} \times 10\,\text{ms} \times 0.08/3 \\ &= 0.008\,\text{mJ}. && (13.10) \end{aligned}$$

13.3. Threshold determination for the investigations on the photoswitching behavior of Kaede-GFP

The threshold value to select one part of a trace as "on" or "off" was determined considering *grKaede* photobleaching behavior upon illumination. In the first series of experiments the sample was illuminated 30 times by 488 nm at $3 \pm 0.3 kW/cm^2$ for 10 ms. To investigate photoconversion a new sample was exposed eight times for 50 ms to 488 nm light. Illumination intensity was set to $0.6 \pm 0.06 kW/cm^2$. Since the dose (illumination intensity $\times$ time) of the blue light was comparable in the experiments analyzing bleaching as well as photoconversion the effect of *grKaede* switching to *rKaede* could be blurred by bleaching. From a monoexponential fit to the data shown in Fig. 10.2 one can roughly estimating a bleaching time of $\tau = 0.12\,$s for the illumination intensity applied. Since the dose acquired scales linearly with intensity, the decay time raises by the same factor as the illumination intensity is decreased. Therefore, a fife-fold increase of the bleaching time compared to the photobleaching experiments can be assumed due to the fife

times lower excitation intensity of 488 nm light when the photoconversion was investigated. With $r = I_{1-4}/I_{5-8} = \exp(T/2\tau)$, where $T = 8 \times 50\,\text{ms} = 0.4\,\text{s}$ is the total illumination time at 488 nm and $\tau = 0.60\,\text{s}$, the ratio r between the mean intensity of the first versus the last four frames can be estimated as $r = 1.4$. Therefore, the threshold value $r = 2$ was set for both channels indicating "switching on" behavior for $I_{1-4}/I_{5-8} < 0.5$ ("switching off" for $I_{1-4}/I_{5-8} > 2$). (Bulk bleaching experiments (data not shown) suggested a similar bleaching rate for *rKaede* as for *grKaede* under the conditions applied.)

Based on the threshold criteria the intensity trajectories were sorted in 16 different groups representing the possible combinations of emission dynamics pattern in each channel.

13.4. Linking algorithm Link_trajectories

The linking algorithm was kindly provided by I.F. Sbalzarini as MATLAB-code and adapted to our needs. Specifically, the cost function is solely determined by the distance between potentially linked spots. The intensities (zeroth order moments) and "widths" (second order moment) of the spots do not contribute. Additionally, because the molecules exhibited no blinking (on the ms-timescale or longer), the spots at time t were linked for $t + r$ with fixed $r = 1$, implying that only correlations between immediately adjacent frames were considered.

In the following, the *Link_trajectories* routine and the role of the L_{max} -parameter shall be discussed.

Given are two consecutive frames p and p+1 containing m and n spots, respectively $(m, n \in N)$. Further, consider two particular spots $i \in M = \{1, ..., m\}$ in frame p and spot $j \in N = \{1, ..., n\}$ in frame $p + 1$.

For each of the frame pairs $(p; p + 1)$, *Link_trajectories* finds the optimal linking of the spots determining the minimum of a cost function $f_p = f_p(M, N; L_{max})$.

Within the routine, L_{max} gives the maximum distance which is allowed between two consecutive spots belonging to the same trajectory.

The spatial distance between spot i and spot j is given by $r^{ij}_{p,p+1}$. Then, for all spots with $r^{ij}_{p,p+1} > L_{max}$, the cost function $f^{ij}_p = f^{ij}_p\left(r^{ij}_{p,p+1}; L_{max}\right)$ is set to ∞ and, hence, the trajectory can not be continued between spots i and j. If $r^{ij}_{p,p+1} \leq L_{max}$, f^{ij}_n is set to a finite value, monotonically increasing with $r^{ij}_{p,p+1}$.

In case spot i in frame p can not be linked to another spot in frame $p+1$ (because the number of spots in two consecutive frames differ $(m \neq n)$ or $r^{ij}_{p,p+1} > L_{\max}$), it is linked to a "dummy" spot $n + 1$. (Vice versa, spot j in frame $p + 1$ would be linked to "dummy" $m + 1$.)

For spots linked to dummies, $r_{p,p+1}^{i,n+1} = r_{p,p+1}^{m+1,j} = L_{max}$ yielding a finite $f_p^{i,n+1} = f_p^{m+1,j}$.

Besides the $(m+1) \times (n+1)$ cost function matrix $\left(f_p^{ij}\right)$, the routine computes a $(m+1) \times (n+1)$ linking matrix $\left(a_p^{ij}\right)$ with $a_p^{ij} = \begin{cases} 1, & i \text{ linked to } j \\ 0, & \text{else} \end{cases}$.

The total cost function is given by $f_p = \sum_i^{m+1} \sum_j^{n+1} a_p^{ij} f_p^{ij}$. To optimize the linking of the spots, thus, the routine minimizes f_p by varying $\left(a_p^{ij}\right)$ under the conditions $\sum_{i=1}^{m+1} a_p^{ij} = 1, \ \forall j = 1, ...n$ and $\sum_{j=1}^{n+1} a_p^{ij} = 1, \ \forall i = 1, ...m$. (This is featured by iteratively permuting the spot combinations and computing f_p : the spot pairs (i_1, j_1), (i_2, j_2) become (i_2, j_1), (i_1, j_2) etc.)

Bibliography

[1] E. Abbé. Beiträge zur Theorie des Mikroskops und der mikroskopischen Wahrnehmung. *M. Schultze's Arch. Microsc. Anat.*, 9:413–468, 1873.

[2] C. M. Anderson, G. N. Georgiou, I. E. Morrison, G. V. Stevenson, and R. J. Cherry. Tracking of cell surface receptors by fluorescence digital imaging microscopy using a charge-coupled device camera. low-density lipoprotein and influenza virus receptor mobility at 4degrees c. *J. Cell Sci.*, 101(Pt2):415–425, 1992.

[3] R. Ando, H. Hama, M. Yamamoto-Hino, H. Mizuno, and A. Miyawaki. An optical marker based on the uv-induced green-to-red photoconversion of a fluorescent protein. *Proc. Natl. Acad. Sci. USA*, 99:12651–12656, 2002.

[4] M. I. Angelova and D. S. Dimitrov. Liposome electroformation. *Faraday Discuss.*, 81:303–311, 1986.

[5] M. I. Angelova, S. Soleau, Ph. Meleard, J. F. Faucon, and P. Bothorel. Preparation of giant vesicles by external ac electric fields. kinetics and applications. *Prog. Coll. Pol. Sci.*, S89:127–131, 1992.

[6] L. S. Barak and W. W. Webb. Diffusion of low density lipoprotein-receptor complex on human fibroplasts. *J. Cell Biol.*, 95:846–852, 1982.

[7] H. C. Berg. *Random Walks in Biology.* Princeton University Press, 1983.

[8] N. Bobroff. Position measurement with a resolution and noise-limited instrument. *Rev. Sci. Instrum.*, 57(6):1152–1157, 1986.

[9] M. Born and E. Wolf. *Principles of Optics, p.472ff.* Cambridge University Press, Seventh (expanded) edition edition, 1999.

[10] I. N. Bronstein, K. A. Semedjajew, G. Musiol, and H. Mühlig. *Taschenbuch der Mathematik.* Verlag Harry Deutsch, Thun and Frankfurt a. M., Germany, 2 edition, 1995.

[11] R. Brown. A brief account of microscopical observations, made in the months of june, july, and august, 1827 on the particles contained in the pollen of plants; and ton the general existence of active molecules in organic and inorganic bodies. *Privately printed. Reprinted in Edin. New Phil. J.*, 5:358–371, 1828.

[12] R. E. Campbell, O. Tour, A. E. Palmer, P. A. Steinbach, G.S. Baird, D. A. Zacharias, and R. Y. Tsien. A monomeric red fluorescent protein. *Proc. Natl. Acad. Sci. USA*, 99:7877–7882, 2002.

[13] M. Chattoraj, B. A. King, G. U. Bublitz, and S. G. Boxer. Ultra-fast excitated state dynamincs in green fluorescent protein: Multiple states and proton transfer. *Proc. Natl. Acad. Sci. USA*, 93:8362–8367, 1996.

[14] M. K. Cheezum, W. F. Walker, and W. H. Guilford. Quantitative comparison of algorithms for tracking single fluorescent particles. *Biophys. J.*, 81:2378–2388, 2001.

[15] D. M. Chudakov, V. V. Verkhusha, D. B. Staroverov, E. A. Souslova, S. Lukyanov, and K. A. Lukyanov. Photoswitchable cyan fluorescent protein for protein tracking. *Nat. Biotechnol.*, 22(11):1435–1439, 2003.

[16] S. B. Dalziel. Decay of rotating turbulence: some particle tracking experiments. *Appl. Sci. Res.*, 49:217–244, 1992.

[17] B. L. de Groot and H. Grubmüller. Water permeation across biological membranes: Mechanism and dynamics of aquaporin-1 and glpf. *Science*, 294:2353–2357, 2001.

[18] Nuydens R Moeremans M DeMey J. Debrabander M, Geuens G. Probing microtubule-dependent intracellular motility with nanometre particle video ultramicroscopy (nanovid ultramicroscopy). *Cytobios*, 43(174S):273–83, 1985.

[19] W. Demtröder. *Laser Spectroscopy: Springer Series in Chemical Physics*, volume 5. Springer, Berlin, 1988.

[20] D. J. Denvir and E. Conroy. Electron multiplying ccds. Technical report, Andor Technology Ltd. UK, http://www.emccd.com/Electron

[21] A. Diaspro. *Confocal and Two-Photon Microscopy.* Wiley-Liss, New York, 2002.

[22] R. M. Dickson, A. B. Cubitt, R. Y. Tsien, and W. E. Moerner. On/off blinking and switching behaviour of single molecules of green fluorescent protein. *Nature*, 388:355–358, 1997.

[23] R. M. Dickson, D. J. Norris, Y. Tzeng, and W. E. Moerner. Three-dimensional imaging of single molecules solvated in pores of poly(acrylamide) gels. *Science*, 274:966–968, 1996.

[24] D. S. Dimitrov and M. I. Angelova. Lipid swelling and liposome formation mediated by electric-fields. *Bioelectroch. Bioener.*, 19:323–336, 1988.

[25] P. S. Dittrich, S. P. Schaefer, and P. Schwille. Characterization of the photoconversion reaction of the fluorescent protein kaede on single molecule level. *Biophys. J.*, 89:3446–3455, 2005.

[26] C. Eggeling, A. Volkmer, and C. A. M. Seidel. Molecular photobleaching kinetics of phodamine 6g by one- and tow-photon induced confocal fluorescence microscopy. *ChemPhysChem*, 6:791–804, 2005.

[27] J. Eichler and H.J. Eichler. *Laser. Bauformen, Strahlführung, Anwendungen.* Springer. Berlin, Heidelberg, New York, 5 edition, 2003.

[28] A. Einstein. Die von der molekularkinetischen theorie von wärme geforderte bewegung von in ruhenden flüssigkeiten suspendierten teilchen. *Ann. Phys.*, 17:549, 1905.

[29] T. J. Feder, I. Brust-Mascher, J. P Slattery, B. Baird, and W. W. Webb. Constrained diffusion or immobile fraction on cell surfaces: a new interpretation. *Biophys. J.*, 70:2767–2763, 1996.

[30] C. Gerthsen and H. Vogel. *Physik.* Springer-Lehrbuch, 17 edition, p. 215, 1993.

[31] R. N. Ghosh and W. W. Webb. Automated detection and tracking of individual and clustered cell surface low density lipoprotein receptor molecules. *Biophys. J.*, 66:1301–1318, 1994.

[32] M. Goulian and S. M. Simon. Tracking single proteins within cells. *Biophys. J.*, 79:2188–2198, 2000.

[33] L. A. Gross, G. S. Baird, R. C. Hoffman, K. K. Baldridge, and R. Y. Tsien. The structure of the chromophore within dsred, a red fluorescent protein from coral. *Proc. Natl. Acad. Sci. USA*, 97:11990–11995, 2000.

[34] N. G. Gurskaya, V. V. Verkhusha, A. S. Shcheglov, D. B. Staroverov, T. V. Chpurnykh, A. F. Fradkov, S. Lukyanov, and K. A. Lukyanov. Engineering of a monomeric green-to-red photoactivatavle fluorescent protein induced by blue light. *Nat. Biotechnol.*, 24(4):461–465, 2006.

[35] S. Habuchi, R. Ando, P. Dedecker, W. Verheijen, H. Mizuno, A. Miyawaki, and J. Hofkens. Reversible single-molecule photoswitching in the gfp-like fluorescent protein dronpa. *Proc. Natl. Acad. Sci. USA*, 102:9511–9516, 2005.

[36] G. S. Harms, L. Cognet, P. H. M. Lommerse, G. A. Blab, H. Kahr, R. Gamsjager, H. P. Spaink, N. M. Soldatov, C. Romanin, and T. Schmidt. Single-molecule imaging of l-type ca2+ channels in live cells. *Biophys. J.*, 81:2639–2646, 2001.

[37] J. W. Harris and H. Stocker. *Maximum Likelihood Method, §21.10.4 in Handbook of Mathematics and Computational Science.* Springer-Verlag, p. 824, New York, 1998.

[38] U. Haupts, S. Maiti, P. Schwille, and W. W. Webb. Dynamics of fluorescence fluctuations in green fluorescent protein observed by fluorescence correlation spectroscopy. *Proc. Natl. Acad. Sci. USA*, 95:13573–13578, 1998.

[39] E. Hecht. *Optics, p.264.* Addison Wesley, 4th edition, 2002.

[40] E. Hecht. *Optics, p.485.* Addison Wesley, 4th edition, 2002.

[41] R. Heintzmann. *http://wwwuser.gwdg.de/˜rheintz/View5D/.*

[42] R. Heintzmann. *Resolution Enhancement of Biological Light Microscopic Data (Ph.D. thesis), p. 29, App. C2.* PhD thesis, University Heidelberg, Germany, 1999.

[43] J. Helenius, G. Brouhard, Y. Kalaizidis, S. Diez, and J. Howard. The depolymerizing kinesin mcak uses lattice diffusion to rapidly target microtubule ends. *Nature*, 441(7089):115–119, 2006.

[44] F. L. Hichcock. The distribution of a product from several sources to numerous localities. *J. Math. Phys.*, 20:224, 1941.

[45] J. Howard. *Mechanics of motor proteins and the cytoskeleton.* Sunderland, MA: Sinauer Associates, 2001.

[46] S. B Howell. *Handbook of CCD Astronomy.* Cambridge University Press, 2000.

[47] J. Janesick. *Scientific Charge-Coupled Devices.* SPE, Bellingham, WA, 2001.

[48] J. Janesick and T Elliott. *Astronomical*, volume 23. ASP Conference Series, 1992.

[49] G. Jung, S. Mais, A. Zumbusch, and C. Brauchle. Two-color fluorescence correlation spectroscopy of one chromophore: Application to the e222q mutant of the green fluorescent protein. *J. Chem. Phys.*, 114:3149–3156, 2001.

[50] S.M. Kay. *Fundamentals of Statistical Signal Processing.* Prentice Hall PTR, Upper Saddle River, NJ, U.S.A., 1993.

[51] U. Kubitscheck, O. Kückmann, T. Kues, and R. Peters. Imaging and tracking of single GFP molecules in solution. *Biophys. J.*, 78:2170–2179, 2000.

[52] T. Kues. *Visualisierung einzelner Proteinmoleküle und Analys ihrer Trajektorien in intakten Zellkernen mittels Weitfeld-Fluoreszenzmikroskopie.* PhD thesis, University Bremen, 2001.

[53] T. Kues. *Visualisierung einzelner Proteinmoleküle und Analys ihrer Trajektorien in intakten Zellkernen mittels Weitfeld-Fluoreszenzmikroskopie, Fig. 2.17.* PhD thesis, University Bremen, 2001.

[54] T. Kues. *Visualisierung einzelner Proteinmoleküle und Analys ihrer Trajektorien in intakten Zellkernen mittels Weitfeld-Fluoreszenzmikroskopie, p. 43.* PhD thesis, University Bremen, 2001.

[55] T. Kues, A. Dickmanns, R. Lührmann, R. Peters, and U. Kubitscheck. High intranuclear mobility and dynamic clustering of the splicing factor u1 snrnp observed by single particle tracking. *Proc. Natl. Acad. Sci. USA*, 98:12021–12026, 2001.

[56] T. Kues, R. Peters, and U. Kubitscheck. Visualization and tracking of single protein molecules in the cell nucleus. *Biophys. J.*, 80:2954–2967, 2001.

[57] J. Lakowicz. *Principles of Fluorescence Spectroscopy.* Kluwer Academic and Plenum Publishers, New York, 1999.

[58] H. Lossau, A. Kummer, R. Heinecke, F. Pollingerdammer, C. Kompa, G. Bieser, T. Jonsson, C. M. Silva, M. M. Yang, D. C. Youvan, and M. E. Michelbeyerle. Time-resolved spectroscopy of wild-type and mutant green fluorescent proteins reveals excited state deprotonation consistent with fluorophore-protein interactions. *Chem. Phys.*, 213:1–16, 1996.

[59] F. Malvezzi-Campeggi, M. Jahnz, K. G. Heinze, P. Dittrich, and P.Schwille. Light-induced flickering of dsred provides evidence for distinct and interconvertible fluorescent states. *Biophys. J.*, 81:1776–1785, 2001.

[60] M. V. Matz, A. F. Fradkov, Y. A. Labas, A. P. Savitsky, A. G. Zaraisky, M. L. Markelov, and S. A. Lukyanov. Fluorescent proteins from nonbioluminescent anthozoa species. *Nature Biotechnol.*, 17:969–973, 1999.

[61] R. M. Mazo. *Brownian Motion - Fluctuations, Dynamics and Applications.* Oxford Science Publications, Oxford, New York, 2002.

[62] H. Mizuno, T. K. Mal, K. I. Tong, R. Ando, T. Furuta, M. Ikuro, and A. Miyawaki. Photo-induced peptide cleavage in the green-to-red conversion of a fluorescent protein. *Mol. Cell*, 12:1051–1058, 2003.

[63] W. E. Moerner and L. Kador. Optical-detection and spectroscopy of single molecules in a solid. *Phys. Rev. Lett.*, 62:2535–2538, 1989.

[64] J. F. Nagle. Long tail kinetics in biophysics? *Biophys. J.*, 63:366–370, 1992.

[65] P. C. Nelson. *Biological Physics*. W. H. Feeman and Company, 2003.

[66] S. Nie, D. T. Chiu, and R. N. Zare. Probing individual molecules with confocal fluorescence microscopy. *Science*, 266:1018–1021, 1994.

[67] K. Nienhaus, G. U. Nienhaus, J. Wiedenmann, and H. Nar. Structural basis for photo-induced protein cleavage and green-to-red conversion of fluorescent protein eosfp. *Proc. Natl. Acad. Sci. USA*, 102:9156–9159, 2005.

[68] R. J. Ober, S. Ram, and E. S. Ward. Localization Acurracy in Single-Molecule Microscopy. *Biophys. J.*, 86:1185–1200, 2004.

[69] Y. Okada and N. Hirokawa. A progressive single-headed motor: Kinesin superfamily protein kif1a. *Science*, 238:1152–1157, 1999.

[70] M. Ormö, A. B. Cubitt, K. Kallio, L. A. Gross, R. Y. Tsien, and S. J. Remington. Crystal structure of the aequorea victoria green fluorescent protein. *Science*, 273:1392–1395, 1996.

[71] M. Orrit and J. Bernhard. Single pentacene molecules detected by fluorescence excitation in a p-terphenyl crystal. *Phys. Rev. Lett.*, 65:2716–2719, 1990.

[72] A. A. Pakhomov, N. Y. Martynova, N. G. Gurskaya, T. A. Balashova, and V. I. Martynov. Photoconversion of the chromophore of a fluorescent protein from dendronephthya sp. *Biochemistry-Moscow*, 69:901–908, 2004.

[73] G. H. Patterson and J. Lippincott-Schwartz. A photoactivatable gfp for selective photolabeling of proteins and cells. *Science*, 297:1873–1877, 2002.

[74] H. Qian, M. P. Sheetz, and E. L. Elson. Single particle tracking - analysis of diffusion and flow in two-dimensional systems. *Biophys. J.*, 60:910–921, 1991.

[75] C. R. Rao. *Linear Statistical Inference and its Applications*. John Wiley & Sons, New York, 1965.

[76] Lord Rayleigh. On the theory of optical images, with special reference to the microscope. *Phil. Mag.*, 54(5):167–195, 1896.

[77] M. S. Robbins and B. J. Hadwen. The noise performance of electron multiplying charge-coupled devices. *IEEE Transactions on Electron Devices*, 50(5):1227–1232, 2003.

[78] D. Sage, F. R. Neumann, F. Hediger, S. M. Gasser, and M. Unser. Automatic tracking of individual fluorescence particles: Application to the study of chromosome dynamics. *IEEE Trans. Image Process.*, 14:1372–1383, 2005.

[79] T. Salvin and P. S. Doyle. Static and dynamic errors in particle tracking microrheology. *Biophys. J.*, 88:623–638, 2005.

[80] M. Saxton. Lateral diffusion in an archipelago. *Biophys. J.*, 64:1766–1780, 1993.

[81] M. J. Saxton. Single-particle tracking: The distribution of diffusion coefficients. *Biophys. J.*, 72:1744–1753, 1997.

[82] M. J. Saxton and K. Jacobson. Single particle tracking: Applications to membrane dynamics. *Annu. Rev. Biomol. Struct.*, 26:373–399, 1997.

[83] I. F. Sbalzarini and P. Koumoutsakos. Feature point tracking and trajectory analysis for video imaging in cell biology. *J. struct. biol.*, 151:182–195, 2005.

[84] S. P. Schäfer, P. S. Dittrich, E. P. Petrov, and P. Schwille. Single molecule fluorescence imaging of the photoinduced conversion and bleaching behavior of the fluorescent protein kaede. *Microsc. Res. Techn.*, 69:210–219, 2006.

[85] Th. Schmidt, Schütz G. J., Baumgartner W., Gruber H. J., and Schindler H. Characterization of photophysics and mobility of single molecules in a fluid lipid membrane. *J. Phys. Chem.*, 99:17662–17668, 1995.

[86] Th. Schmidt, G. J. Schütz, W. Baumgartner, H. J. Gruber, and H. Schindler. Imaging of single molecule diffusion. *Proc. Natl. Acad. Sci. USA*, 93:2926–2929, 1996.

[87] M. Schneider, S. Barozzi, I. Testa, M. Faretta, and A. Diaspro. Two-photon activation and excitation properties of PA-GFP in the 720-920-nm region. *Biophys J.*, 89:1346–1352, 2005.

[88] G. J. Schütz, G. Kada, V. P. Pastushenko, and H. Schindler. Properties of lipid microdomains in a muscle cell mebrane visualized by single molecule microscopy. *EMBO J.*, 19:892–901, 2000.

[89] G. J. Schütz, H. Schindler, and Th. Schmidt. Single Molecule Microscopy on Model Memebranes Reveals Anomalous Diffusion. *Biophys. J.*, 73:1073–1080, 1997.

[90] J. Schuster. *Untersuchung der Diffusion in dünnen Flüssigkeitsfilmen mit Methoden der Einzelmoleküldetektion*. PhD thesis, University of Technology Chemnitz, 2002.

[91] P. Schwille, U. Haupts, S. Maiti, and W. W. Webb. Molecular dynamics in living cells observed by fluorescence correlation spectroscopy with one. and two-photon excitation. *Biophys. J.*, 77:2251–2265, 1999.

[92] D. A. Shagin, E. V. Barsova, Y. G. Yanushevich, A. F. Fradkov, K. A. Lukyanov, Y. A. Labas, T. N. Semenova, J. A. Ugalde, A. Meyers, J. M. Nunez, E. A. Widder, S. A. Lukyanov, and M.V. Matz. Gfp-like proteins as ubiquitous metazoan superfamily: Evolution of functional features and structural complexity. *Mol. Biol. Evol.*, 21:841–850, 2004.

[93] N. C. Shaner, R. E. Campbell, P. A. Steinbach, B. N. G. Giepmans, A. E. Palmer, and R. Y. Tsien. Improved monomeric red, orange and yellow fluorescent proteins derived from discosoma sp red fluorescent protein. *Nature Biotechnol.*, 22:1567–1572, 2004.

[94] H. Stroppe. *Physik*. VEB Fachbuchverlag Leipzig, 8. edition, p. 164, 1990.

[95] R. E. Thompson, D. R. Larson, and W. W. Webb. Precise Nanometer Localization Analysis for Individual Fluorescent Probes. *Biophys. J.*, 82:2775–2783, 2002.

[96] L. J. van Vliet, D. Sudar, and I. T. Young. *Cell Biology*, volume III, chapter Digital Fluorescence Imaging Using Cooled CCD Array Cameras, pages 109–120. Academic Press, New York, 2 edition, 1998.

[97] S. Weiss. Fluorescent spectroscopy of single biomolecules. *Science*, 283:1676–1683, 1999.

[98] E. W. Weisstein. Maximum likelihood. *From MathWorld–A Wolfram Web Resource*, http://mathworld.wolfram.com/MaximumLikelihood.html.

[99] J. Wiedenmann, S. Ivanchenko, F. Oswald, F. Schmitt, C. Rocker, A. Salih, K. D. Spindler, and G.U. Nienhaus. Eosfp, a fluorescent marker protein with uv-inducible green-to-red fluorescence conversion. *Proc. Natl. Acad. Sci. USA*, 101:15905–15910, 2004.

[100] J. Wiedenmann, A. Schenk, C. Rocker, A. Girod, K. D. Spindler, and G. U. Nienhaus. A far-red fluorescent protein with fast maturation and reduced oligomerization tendency from entacmaea quadricolor (anthozoa, actinaria). *Proc. Natl. Acad. Sci. USA*, 99:11646–11651, 2002.

[101] X. S. Xie and J. K. Trautman. Optical studies of single molecules at room temperature. *Annu. Rev. Phys. Chem.*, 49:441–480, 1998.

[102] X.-H. Xu and E. S. Yeung. Direct measurement of single-molecule diffusion and photodecomposition in free solution. *Science*, 275:1106, 1997.

[103] S. Zacks. *The Theory of Statistical Inference*. John Wiley & Sons, New York, 1971.

[104] F. Zhang, B.Crise, B. Su, Y. Hou, J. K. Rose, A. Bothwell, and K. Jacobson. Lateral diffusion of membrane-spanning and glycosylphosphatidylinositol-linked proteins: toward establishing rules governing the lateral mobility of membrane proteins. *J. Cell Biol.*, 115(1):75–84, 1991.

[105] J. Zhang, R. E. Campbell, A. Y. Ting, and R. Y. Tsien. Creating new fluorescent probes for cell biology. *Nature Rev. Mol. Cell Biol.*, 3:906–918, 2002.

List of abbreviations

ADC:	Analog-to-digital converter
AFM:	Atomic force microscopy
AOM:	Acousto-optical modulator
APD:	Avalanche photo diode
BFP:	Back focal plane
BM:	Brownian motion
CCD:	Charge coupled device
COI:	Center of intensity
cts, count:	counts, digital units of CCD camera
DIC:	Differential interference contrast
DH:	Displacement histogram, step distance histogram
e:	photoelectrons
FWHM:	Full width at half maximum
FRET:	Förster resonance energy transfer
GFP:	Green Fluorescent Protein
GUV:	Giant Unilamellar Vesicle
ICCD:	Intensified CCD
LSM:	Laser scanning microscope
MCP:	Multichannel plate
MSD:	Mean square displacement
PAA:	Poly-acrylamide
PMT:	Photomultiplier tube
ph:	photons
ROI:	Region of interest
SMT:	Single molecule tracking
SNR:	Signal-to-noise ratio

Acknowledgements

My thank first goes to Prof. Dr. Petra Schwille for supervising the thesis, giving me the opportunity and financial means to work in her lab. Especially I acknowledge the freedom and open work atmosphere in her group.

Additionally, I want to thank the members of my Ph.D. comitee, especially the referees Prof. Dr. Ulrich Kubitscheck, Bonn, and Prof. Dr. Lukas Eng, Dresden, for a critical review of the thesis.

For my time in Göttingen I am indebted to Prof. Dr. Dr. Detlef Schild as the chairman of the Graduiertenkolleg 723 for accepting me to the Graduiertenkolleg. Besides providing financial support, he organized very stimulating visits to conferences and summer schools.

I want to thank Eugene Petrov for being an extremely knowledgable, critical and motivating colleague and mentor in all respects, scientific and more. His continuous availability and constructive suggestions helped me invaluably to complete this thesis.

I owe special thanks to Rainer Heintzmann who was a very helpful and motivating colleague during my time at the MPI in Göttingen. I am very grateful for his expertise on image analysis and programming, Thanks for providing the View5D rendering software!

I am very thankful to the members of the Graduiertenkolleg 723, especially Arne Gennerich for his organizing efforts and for having many interesting and motivating discussions about "science and life".

For her constant and motivating work and for her open mind I want to thank Karin Birkenfeld and her colleague Sylvia Löbermann who helped me tremendously in all issues related the biochemistry lab.

I am very grateful to Norbert Gulde, Roper Scientific, for his very valuable expertise on CCD cameras.

Thanks to the researchers of the field, who helped me on the stony path to single molecule imaging, especially Ulrich Kubitscheck and Thorsten Kues (at that time in Münster) and Gerhard Schütz, Linz.

I want to thank the members of the fine mechanics and fine optics workshops of the MPI for experimental Biophysics in Göttingen for providing me with indispensable know-how and excellent work. Their professional motivation and work ethics were

a lasting impression to me.

Also my thank goes to Petra Dittrich for being a great person and colleague and motivating me for the great fun of long distance running.

I want to thank Dag Scherfeld for sharing the office with me and for always interesting conversations.

I owe deep respect and thank to Svitlana Berezhna who was a very close and motivating colleague during the Göttingen days. Especially I could learn a lot concerning the sometimes roughed but also exciting paths in the real life of a scientist.

My room mates Hella Hartmann and Fedor Malic I want to thank deeply for always being patient colleagues and tolerating unavoidable emotional outbreaks during my early stages as a programmer.

For her never-ending patience in administrative matters and fabulously correct work I want to say a big thank you to our secretary Claudia Lorenz.

Special thanks goes to all other Göttinger members of the Schwille-group, especially Tobias Kohl, Michael Jahnz, Elke Haustein, Guido Böse, Kirsten Bacia, Nicoletta Kahya, Barbara Müller and Katrin Heinze who enabled me a good start into the Ph.D. and always provided a pleasant and motivation work atmosphere. The present group in Dresden, especially my lab mate Wolfgang Staroske, and all the other present and previous members (Markus, Jakob, Madhavi, Jonas, Salvo, Inge, Ana, Jörg, Anke, Zdenek, Volkmar, Peter, Stefan, Heiko, Thomas, Alex, Katja, Stefan, Ruth, Christoph, Martin, Dan...) I want to thank for being a great group, as persons and scientifically.

Further, I thank Ivo Sbalzarini to provide me with the particle linking algorithm.

I acknowledge Prof. A. Miyawaki and H. Mizuno for kindly providing us the *Kaede*-GFP protein samples.

Financial support by the BMBF (Biofuture Grant to Prof. Schwille) and the EFRE (grant No. 4-0123.55-20-0370-03/3) is gratefully acknowledged.

I am very grateful to Antje Schmidt for her continuous support in all matters of life and her never ending patience whenever I called from office apologizing 'that it would be later today'. Thanks a lot!!

Finally, I want to thank my parents, Dieter and Maria, for believing in me and supporting me during all my life, materially and mentally. I am very grateful to live with them and Bianka, Christian and Michael in such a benign family.

I am eternally indebted to my grandmother Klara Berneiser who laid the foundation of my interests and doubts, scientific and spiritual.

Erklärung

Hiermit bestätige ich, dass ich diese Doktorarbeit ohne unzulässige Hilfe Dritter und ohne die Benutzung anderer als der angegebenen Hilfsmittel angefertigt habe. Die aus fremden Quellen direkt oder indirekt übernommenen Gedanken sind als solche kenntlich gemacht. Die Arbeit wurde bisher weder im Inland noch im Ausland in gleicher oder ähnlicher Form einer anderen Prüfungsbehörde vorgelegt.

Diese Arbeit wurde in der Zeit von Februar 2002 bis September 2006 unter der Betreuung von Prof. Dr. Petra Schwille zu etwa gleichen Teilen am Max-Planck-Institut für Biophysikalische Chemie, Göttingen, und am Institut für Biophysik, TU Dresden, angefertigt.

Dresden, den 11. September 2006